Influence of Hydrodynamic Derivatives on Ship Manoeuvring Prediction and Application of SQCM to Ship Hull Forces

ファーリ, アクバ, アユブ

Influence of Hydrodynamic Derivatives on Ship Manoeuvring Prediction and Application of SQCM to Ship Hull Forces

July 2021

Fakhri Akbar Ayub

Table of Contents

Chapter 1 Introduction

1.1. General Overview

Good manoeuvring capability of ships is important for marine safety and protection of the marine environment. It is crucial that a ship has a good manoeuvrability and can be controlled safely whether the ship is operated at open water or restricted water. For these reasons, the International Maritime Organization (IMO) has approved the regulations for manoeuvring performance of ships.

From the viewpoint of marine safety, the Interim Standards for Ship Manoeuvrability has been accepted by the IMO as Resolution A.751(18) in 1993 to eliminate ships which have poor manoeuvrability. In 2002, the IMO updated the Interim Standards for Ship Manoeuvrability and the Standards for Ship Manoeuvrability was adopted as Resolution MSC.137(76) (IMO, 2002). In particular, the IMO defined ship manoeuvrability as essential characteristics of ships to change or maintain their course and speed. The bigger ships often have more problems in manoeuvring motion because of the poor manoeuvrability. Every ship that is longer than 100 m in ship length must fulfil the criteria defined in the IMO manoeuvring standards.

To confirm that a ship satisfies the IMO manoeuvring standards, sea trials must be performed. Sea trials are carried out for newly-built ships. The trials should be conducted for ships in fully loaded condition at sea area with enough depth and at calm weather conditions as much as possible. It is mandatory for shipyards to conduct the sea trials even if time and costs are consumed. However, it is difficult for shipyards to execute the sea trials at fully loaded condition for newly-built ships because of empty cargo hold. That is why sea trials are usually conducted at ballast condition and only manoeuvring data for ballast condition can be measured. Additionally, it is almost impossible to conduct the sea trials under the ideal weather conditions specified by the IMO manoeuvring standards. Therefore, prediction of manoeuvring performance based on numerical simulations is often used.

Furthermore**,** it is important to be able to predict the performance indices of ship manoeuvrability such as advance, transfer, tactical diameter, the first and the second overshoot angles for zigzag manoeuvres, and so on at the design stage of ships in order

to secure that ships can be operated safely. Hydrodynamic derivatives play an important role in the prediction of manoeuvring motions of ships at the design stage. Hydrodynamic derivatives have to be known for any type of ships whose manoeuvring performance is under considerations.

Consequently, reliable prediction methods for manoeuvring performance are required. By this reason, verification and validation (V&V) are important related to the accuracy of prediction of manoeuvring performance. Predicted results are expected to be compared with the results of full scale ship trials or benchmark data.

However, there are very few public data of full scale trials carried out at a scientific level with which validation can successfully be made except for the Esso Osaka (Crane, 1979). Full scale trials in shallow and deep waters for the Esso Osaka tanker were carefully performed in 1977. This trial is one of the valuable and successful full scale trial data, and a lot of researcher have used this vessel as benchmark data.

In addition, to compare simulation results with the results of full scale trials, it is strongly advised to carefully consider scale effects and the influence of external disturbances. Wake fraction is different between model ship and full scale ship and sea trials cannot be executed without the influence of wind, wave, and current. These effects must be excluded from the measured data before the comparison.

Hence, the quality of simulations is generally evaluated by using model test results. In this case, free running model tests which are performed in the same way as full scale trials are necessary to evaluate predicted ship manoeuvring motion. On the other hand, captive model tests to measure hydrodynamic forces and moments acting on a ship in manoeuvring motions are necessary to evaluate predicted hydrodynamic forces.

Validation of the predicted results depends on methods used to predict the manoeuvring performance (Berlekom, 1992). This means, it is essential to make a dedicated verification and validation effort related to the prediction or simulation methods and hereby asses the accuracy of the methods.

Moreover, mathematical models of hydrodynamic forces used in prediction of manoeuvring motions have many kinds of errors and uncertainties (Wang et al., 2014,

Dash et al., 2015). Some of the problems are generally affected by hydrodynamic derivatives which are used to express hydrodynamic forces acting on a ship hull (Shenoi et al., 2015), model tests (Woodward, 2013), facilities equipment (Woodward, 2014), etc. Analyzing and assessing the errors are time consuming and very complex. A knowledge of the errors is crucial if any sort of validation is to be done. The relation between prediction results and measured hydrodynamic forces used to obtain hydrodynamic derivatives can only be correctly assessed if the accuracies of both the prediction results and the measured data are known with some uncertainties.

To achieve accurate prediction results, hydrodynamic derivatives which are good in quality must be used. Generally, there are three kinds of methods to obtain the hydrodynamic derivatives such as approximate formulae with the parameters of the principal dimensions of ships based on existing data, captive model tests, and numerical calculation methods based on hydrodynamics.

Approximate formulae are simple calculation methods which can be used easily, but the estimation accuracy of the methods becomes poor if the shape of the hull of a target ship is different from ships in mother data which are used to develop the approximate formulae.

Captive model tests can provide accurate hydrodynamic derivatives by analyzing hydrodynamic forces measured in model basins using model ships. However, it is time consuming to carry out the measurement of hydrodynamic forces even for one condition. Therefore, measurements of the hydrodynamic forces in the same condition are not repeated in general.

As the numerical calculation methods, CFD (Computational Fluid Dynamics) is available to predict the hydrodynamic forces acting on ships by directly solving the Navier-Stokes equation numerically. However, it requires a lot of computational cost and time. As the other kinds of numerical calculation methods, panel methods can also accurately describe the shape of a ship hull and predict the hydrodynamic forces. The SQCM (Source and Quasi Continuous vortex lattice Method) is one of the panel methods and it has been confirmed that the SQCM had good accuracy to calculate hydrodynamic forces produced by a propeller (Nakatake et al., 1994).

1.2. Literature Review

The mathematical models of hydrodynamic forces acting on a ship hull are essential components in the equations of ship motion. They have been defined in terms of inherent values which are different for every type of ship. These terms related to ship hull are known as hydrodynamic derivatives which are derived by analyzing measured hydrodynamic forces acting on a ship hull. They are equal to the rate of change of the force and moment to drift angle, non-dimensional sway velocity, and non-dimensional yaw rate.

The fundamental basis of equations of motion that are used in ship manoeuvring subject has been formed by Davidson and Schiff (1946) by using Newton's second law of motion. They made the first attempt at theoretical approach by regarding a ship as a rigid body with three degrees of freedom (surge, sway, and yaw motions) and described the hydrodynamic forces and moments acting on the ship by the first order derivatives.

However, it was found that whereas the forces and moments became non-linear due to the large values of velocities and cross products of velocities. When a ship is turning with a large rudder angle, the non-linear hydrodynamic forces reach the same order of magnitude as that of the linear component. Furthermore, the non-linear component of yawing moment reaches five to ten times its linear component. These non-linear terms are frequently represented by means of cubic or quadratic polynomial expressions. The coefficient of which are usually determined through conducting captive model tests.

Taylor series expansion to represent the nonlinearities, resulting in a polynomial in two variables was proposed by Abkowitz (1964). Functions describing hydrodynamic forces and moments acting on a ship may involve many motions and orientation parameters. The functions can be reduced to useful mathematical form by using the Taylor series expansion of a function of several variables. In this case, only odd terms in the Taylor series would be required to represent the sway force and yawing moment due to port and starboard symmetry.

On the other hand, the nonlinearities could be calculated for in a different manner, by using quadratic polynomial expressions (Fedyaevsky and Sobolev, 1963). Even though quadratic polynomial expressions are really unsuited since they are even functions, by

introducing a modulus term and different way of writing the nonlinearities, this problem can be avoided. Quadratic functions modulus approach can be shown to represent the hydrodynamic concept of cross-flow drag at large angles of incidence, since it does have some immediate virtue.

Non-linear forces and moments had been calculated by Fedyaevsky and Sobolev (1963) and Norrbin (1971). Quadratic form was used to represent the non-linear nature of forces acting on a ship hull. By assuming lateral force due to drag created by the cross flow velocity component, a good representation was obtained. However, the distribution of non-linear forces was tending to be concentrated toward the stern (Clarke, 1972).

A combination of cubic and quadratic terms to represent non-linear terms had been proposed by Inoue (1978). Even though the difference was not significant, a cubic model could fit the experimental data slightly better than a quadratic model (Ogawa et al., 1980). It is clear there is a different result between the cubic model and the quadratic model. For the sake of getting more precise mathematical models of hydrodynamic forces, the differences between them need to be investigated further.

Furthermore, mathematical models of hydrodynamic forces acting on a ship can be divided into two categories, such as “whole ship models” and “modular models” (ITTC Manoeuvring Committee, 1999). In the whole ship models, equations of motion are composed by the combinations of hydrodynamic force components related to a hull, a propeller, and a rudder. Hydrodynamic coefficients required in the components are determined by conducting captive model tests using a model ship equipped with a propeller and a rudder. Whole ship models perform very well when a ship is taken as a whole but do not allow individual elements to be changed as the design is changed (Dand, 1987).

Chudley et al. (1991) found that a linear whole ship model provided acceptable predictions when the rudder movements were relatively small, but their results were inaccurate when performing a complete turning circle. Compared to full scale trials, their non-linear whole ship model seemed to give an accurate representation of the three degrees of freedom motion in all manoevring situations.

However, the remaining applications in the whole ship models require more flexibility and a distinct knowledge of individual forces acting on a hull, a rudder, and a propeller. This is because all the remaining applications are often based on trying various alternative ship dimensions and/or propeller and rudder geometry to evaluate their influence on manoeuvring performance. The physical meaning of each term of the equations for hydrodynamic forces in the whole ship models is not completely segregated and most of the influence of different elements are hidden or mixed in hydrodynamic derivatives.

Then, modular models were presented in the late 1970's (Ogawa and Kasa, 1978, Kose and Saeki, 1979) to cope with the whole ship models deficiency. In modular models, forces acting on a hull, a propeller and a rudder and forces due to interaction among them or modules of the ship are each represented by different terms in equations, and force coefficients are measured or predicted separately for the hull, propeller and rudder. Interactions among a hull, a propeller and a rudder are sometimes measured in captive model tests, but are more typically determined from empirical relationships incorporating parameters that depend on the geometry and position of the propeller and the rudder relative to the hull. Modular models have to be able to operate in all manoeuvring regime, particularly at zero or slow speed, and give a realistic response to a rudder, a thruster, and a propeller (McCallum, 1992).

There are many and various mathematical models of hydrodynamic forces used in manoeuvring studies and all are subject to many kinds of errors and uncertainties. The scientific process of analyzing and assessing the errors is complex, as well as time consuming and costly. As a consequence, most studies compared numerical and experimental results but hardly ever analyzed and quantified the errors. The quality assessment of the simulated results employed for prediction is then generally given in terms of the level of agreement between the prediction itself and measurement results.

Dand (1992) suggested that error range should always be provided with any prediction or measurement and that such range should be standardized at a total width of twice the standard error. The term "good agreement", which it usually assumed that the prediction is validated, may be taken as overlap between the error range of the prediction itself. The good agreement can be achieved by conducting sensitivity analysis and/or uncertainty

analysis to the prediction of manoeuvring performance. By this fact, a lot of researchers focusing their research to the sensitivity of manoeuvring performance indices such as turning motions and zigzag manoeuvres.

Son and Nomoto (1981) conducted sensitivity analysis based on the 4DOF mathematical model of a container ship S175. They investigated the influence of hydrodynamic coefficients on turning motions and zigzag manoeuvres. The results show that linear derivatives for yawing moment N'_v and N'_r are the most impactful parameter on turning circle, tactical diameter, and second overshoot angle for 10°/10° zigzag manoeuvre. It was found that coefficients with high influence tended to have higher standard deviations and coefficients with low influence tended to have lower standard deviations.

The Manoeuvring Committee in the 28th ITTC carried out sensitivity analysis based on whole ship model presented by Shin et al. (2012) and Sung et al. (2014) to investigate the dominant coefficients for each characteristic of manoeuvring motion by using Monte Carlo simulations (ITTC Manoeuvring Committee, 2017). The results show that turning circle are mostly normally distributed while zigzag manoeuvres do not have a symmetric distribution.

Later, Wang et al. (2014) indicated that non-relevant hydrodynamic coefficients could be removed by doing sensitivity analysis. According to their comparison between simulation results of original and simplified mathematical models for turning motion and zigzag manoeuvres, a mathematical model can be simplified significantly based on the sensitivity analysis. This means, it is possible to decrease the uncertainty in the mathematical model because it was confirmed by Dash et al. (2015) that uncertainties in a mathematical model is larger than the experimental uncertainty. However, it does not mean that the uncertainty in the experimental or other source can be ignored.

Woodward (2014) investigated the source of uncertainty on inter-facility tests. In his research, Monte Carlo simulations is presented to evaluate the propagation of uncertainty. The results of his study on KVLCC1 show that hydrodynamic coefficients in normal probability distribution generate overshoot angles of zigzag manoeuvres in a Weibull distribution. These results show the same agreement with ITTC Manoeuvring Committee (2017). Ayub et al. (2019) also confirmed Weibull distribution on zigzag manoeuvres.

The uncertainties in full scale measurements have been investigated by Gavrilin and Steen (2015). It was found the uncertainty were caused by changing environmental data. By using Monte Carlo simulations, they were able to determine turning trajectories with higher accuracy, hence decreasing the uncertainty on the parameters such as tactical diameter. Gavrilin and Steen (2016) also determined that one of the most important issues to address in future research is the uncertainty of experimental measurements and how it affects validation quality.

Ayub et al. (2021) also investigated the sensitivity of simulated manoeuvring motion to hydrodynamic derivatives derived from measured lateral force and yawing moment including measurement error. Hydrodynamic derivatives are randomly changed one by one, independently. It is considered that the value of each derivative should not be varied independently to grasp the sensitivity of manoeuvring performance to hydrodynamic derivatives precisely.

Furthermore, to achieve good agreement in the prediction of manoeuvring performance, accurate hydrodynamic derivatives must be obtained. Conducting captive model tests is a common way to obtain hydrodynamic derivatives which is derived from measured hydrodynamic forces acting on a ship hull. The problem with captive model tests appears when measurements of the hydrodynamic forces in the same condition are not repeated, because it consumes long time to carry out the measurement even for one condition. Extrapolating data also tends to happen when using the results of the mathematical model outside the tested range of drift angles and rotation rates (ITTC Manoeuvring Committee, 2008).

Based on these reasons, practical application of numerical calculation methods such as Computational Fluid Dynamics (CFD) which is available to predict the hydrodynamic forces by directly solving the Navier-Stokes equation numerically is expected. RANS (Reynolds-Averaged Navier-Stokes equation) calculations are the most used method and they are expected as replenishment for captive model tests (ITTC Manoeuvring Committee, 2008). A matrix of conditions is simulated and results are analyzed to obtain hydrodynamic derivatives in a mathematical model (Cura Hochbaum et al., 2008, Toxopeus et al., 2008). However, a large amount of expertise and code development are

needed to achieve good results. This method also requires a lot of computer resources and time consuming which are inconvenience.

To cope with these problems, researchers have tried to develop fast and cheap method to obtain hydrodynamic forces acting on a hull such as hybrid method which is a combination of captive model tests with potential CFD (ITTC Manoeuvring Committee, 2008). Other than that, panel methods are ideal for calculating the flow field over an airfoil executing unsteady time-dependent motion in an inviscid incompressible medium (Cebeci et al., 2005). This method can also accurately describe the shape of a ship hull.

A method to calculate incompressible potential flow about arbitrary, non-lifting, and three-dimensional bodies had been introduced by Hess and Smith (1964). In this method, the body surface is divided into quadrilateral panels and sources are distributed on the panels. To make the normal component of velocity of the fluid becomes zero on the surface panels, the distribution of sources is obtained. Quadrilateral surface panels are used to replace the integral equation for the source distribution by a set of linear algebraic equations. This method has two advantages over the other methods, which is the equations that must be solved are two-dimensional over the surface of the body rather than the three-dimensional over the entire flow field. By working straightly on the body surface, it can avoid the difficulty that other methods may encounter when the body surface converge the coordinate net in an arbitrary form.

Lan (1970) developed QCM (Quasi Continuous vortex lattice Method) to solve a thin wing problem with considering the wing edge and Cauchy singularities, but it is still keeping the flexibility and simplicity of the conventional vortex lattice method. To fulfilling the conditions of wing boundary, chord wise vortex integral is lowered to finite sum through an altered trapezoidal rule and the theory of Chebychev while the distribution of span wise is assumed to be step wise. The result of his research stated that the current estimation for two-dimensional and three-dimensional wings are more accurate than the conventional vortex lattice method for an airfoil with a flap deflection. The results of planar lifting surface are proportionate to those by some continuous loading methods, however this method requires much less computing time in some comparison.

By combining the Hess and Smith (1964) method and the QCM (Lan, 1970), a calculation method for three-dimensional unsteady wing problem has been developed by Nakatake et al. (1994). This simple surface panel method named as the SQCM (Source and Quasi Continuous vortex lattice Method) is one of the panel method that can easily satisfy the Kutta condition in steady and unsteady condition problems. Hess and Smith method is used to represent the wing surface and the vortex strength and the source strength are determined simultaneously. Furthermore, the Kutta condition is satisfied automatically as same as the QCM. It has been confirmed that this calculation method can accurately predict hydrodynamic force produced by a propeller.

Applications of the SQCM to the estimation of hydrodynamic forces have been done by a lot of researchers (Ando et al., 1995, Maita et al., 1997a, 1997b, Kanemaru et al., 2013). A good agreement with experimental data is presented in these researches. However, almost all of them focusing on the hydrodynamic forces acting on a propeller. In fact, the SQCM can be applied to calculate hydrodynamic forces acting on a hull by treating ship hull as thick wing.

Ando et al. (1997) investigated the SQCM for estimation of hydrodynamic forces acting on a ship in oblique towing. Numerical results for three VLCC models (SR221 A, B, and C) which have different aft shapes with each other are shown. The agreements of estimated hydrodynamic forces and experimental data are fairly well.

Hydrodynamic forces acting on a Wigley hull in manoeuvring motion based on the SQCM had been calculated by Ayub et al. (2020). It was confirmed that the free vortices shed from the bottom of a hull contributed to the improvement of prediction accuracy on lateral force and yawing moment. To investigate further the capability of the SQCM on the prediction of hydrodynamic forces acting on a hull, Ayub et al. (2021) applied new vortex models considering the deformation of free vortices to the calculation of hydrodynamic forces. It was confirmed that the hydrodynamic forces can be predicted accurately in the range of small drift angle, at first. Then, two kinds of vortex models are examined to improve the estimation accuracy of lateral force and yawing moment in the range of large drift angle.

1.3. Research Objectives

As described above, the accuracy of predicted manoeuvring motions mainly depends on the quality of hydrodynamic coefficients included in mathematical models of hydrodynamic forces acting on a ship. Especially, lateral force and yawing moment acting on a ship hull have great influence on manoeuvring motions.

Two kinds of mathematical models of lateral force and yawing moment acting on a ship hull are investigated. One is a cubic model which expresses non-linear terms of hydrodynamic forces by cubic polynomials on drift angle (or non-dimensional sway velocity) and non-dimensional yaw rate. The other is a quadratic model based on quadratic polynomials.

In order to have better understanding about difference between the characteristics of cubic model and quadratic model, course stability index which is calculated by using linear hydrodynamic derivatives are investigated. Then, to clarify the advantages and disadvantages of both models, sensitivity of simulated ship manoeuvring motion to hydrodynamic derivatives derived from measured lateral force and yawing moment including measurement error coming from the resolution of measurement equipment, fluctuation of towing speed and angular velocity of a carriage, setting error in drift angle, and so on is investigated.

Monte Carlo simulation method is used to analyze the sensitivity. Varying the assumed values of measurement error randomly, evaluation indices such as advance, transfer and tactical diameter for turning motion and the first and the second overshoot angles for 10°/10° and 20°/20° zigzag manoeuvres are evaluated to quantify the influence of the measurement error on manoeuvring performance. By assuming the measurement error, close relation between linear and non-linear derivatives can be included in the sensitivity analyses.

The SQCM is applied to predict hydrodynamic forces acting on a ship hull in drift motion. A ship hull is treated as a thick wing. To represent the flow field around the hull appropriately, vortex models considering the deformation of free vortices are introduced and applied for three ship hulls which are Wigley, KCS, and KVLCC2. Predicted results

are compared with experimental data measured by captive model tests to verify the effectiveness of the vortex models to improve the accuracy of prediction.

The aim of this study is to clarify the difference between the characteristics of the cubic and quadratic models of hydrodynamic forces acting on a ship hull and to investigate the sensitivity of simulated ship manoeuvring motion to hydrodynamic derivatives including the influence of measurement error. Furthermore, applicability of the SQCM for the prediction of hull forces is investigated introducing two kinds of vortex models with the consideration of the deformation of free vortices.

1.4. Thesis Layout

This thesis consists of six chapters where **Chapter 1** introduces a general overview of this study, such as hydrodynamic derivatives, manoeuvring prediction methods and so on. A literature review is presented associated with mathematical models of hydrodynamic forces acting on a hull, sensitivity analysis related to ship manoeuvring motion. The objectives and expected outcome of this research as well as a brief layout of this thesis are also presented.

Chapter 2 starts by presenting the equations of motion for ship manoeuvring motions. Mathematical models of hydrodynamic forces which are necessary to simulate ship manoeuvring motion are described in this chapter. The differences between the characteristics of a cubic model and a quadratic model of hydrodynamic forces acting on a ship hull are evaluated and investigation on course stability index is also presented.

The sensitivity of simulated ship manoeuvring motion using hydrodynamic derivatives to measurement error included in measured lateral force and yawing moment is investigated in **Chapter 3**. Furthermore, difference of the sensitivity between hydrodynamic derivatives based on a cubic model and a quadratic model is discussed.

To calculate lateral force and yawing moment acting on a ship hull representing the shape of the hull accurately, the SQCM is introduced in **Chapter 4**. To represent flow field around the hull appropriately, vortex models considering the deformation of free vortices are also introduced.

To investigate the applicability of SQCM, **Chapter 5** presents the results of the SQCM application to the Wigley hull and real hull such as KCS and KVLCC2. The results of hydrodynamic forces obtained from the SQCM are compared with experimental data. Pressure distributions for each ship is also presented in this chapter.

Finally, the conclusions of this research and recommendation for future work are presented in **Chapter 6**.

Chapter 2 Mathematical Models for Simulating Ship Manoeuvring Motion

2.1. Introduction

Mathematical models of hydrodynamic forces acting on a ship hull are essential components in the equations of ship motions. They have been defined in terms of inherent values which are different for every type of ship. These terms are known as hydrodynamic derivatives or hydrodynamic coefficients that have been shown to be equal to the rate of change of force and moment to suitable parameters. To derive mathematical models of hydrodynamic forces acting on a rigid body moving over the water, various approaches can be used.

In this chapter, the equations of motion for ship manoeuvring are described. Mathematical models for hydrodynamic forces acting on a ship are presented based on Manoeuvring Modelling Group (MMG) model. This MMG model consists of the individual properties of a hull, a propeller, a rudder and other external components. Two kinds of mathematical models for lateral force and yawing moment often used in MMG model are presented. One of the model is represented in the form of cubic polynomials by Yasukawa (2015) and the other model is represented in the form of quadratic polynomials by Kijima et al. (1990). Here after, the former is noted as a "cubic model" and the latter is noted as a "quadratic model".

Furthermore, comparing the cubic model and the quadratic model, it is generally said that the cubic model is better for approximating the accuracy of hydrodynamic force including the range of large motion (Ogawa et al., 1980). However, since it does not include a term proportional to the square of the drift angle β, it is pointed out that it is inconsistent with the theoretical study. Since the cubic model is more advantageous in explaining physical phenomena, different kinds of models are used for each research institute or company, including the choice of sway velocity v.

In order to investigate the differences between the characteristics of hydrodynamic forces expressed by the cubic and the quadratic models, hydrodynamic data accumulated through captive model tests conducted at Kyushu University were reanalyzed. As the

IMO manoeuvring standards cover the course keeping and yaw checking abilities as well, course stability has become important. Course stability index is presented to show the differences between two kinds of mathematical models.

2.2. Equations of Manoeuvring Motion

2.2.1. Equations of Motion in Six Degrees of Freedom

To inspect the motion of an object, equations of motion can be used. In this section, body fixed coordinate system $G - xyz$ shown in Fig. 2.1 is used to derive equations of manoeuvring motion around the centre of gravity of a ship.

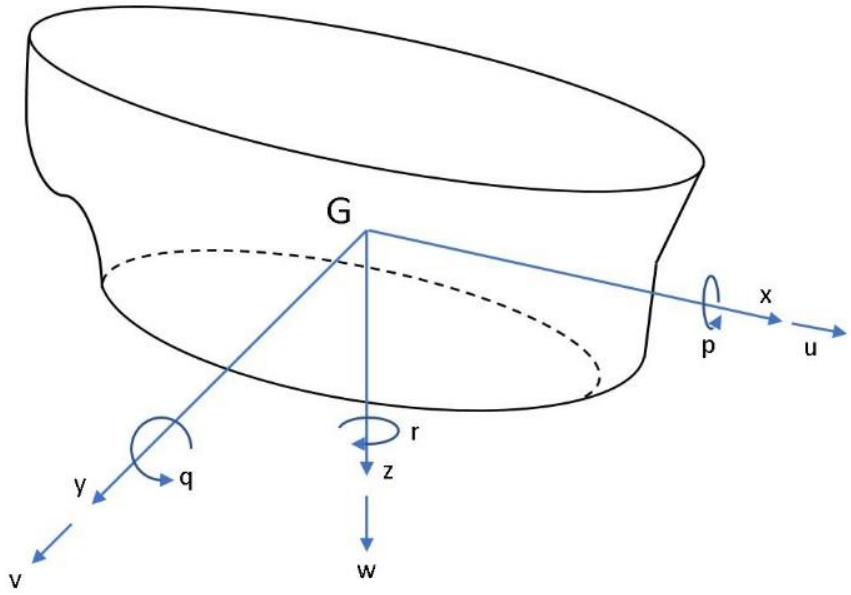

Figure 2.1 Body fixed coordinate system

The positive directions of x, y and z axes are defined as shown in Fig. 2.1. u, v, and w are ship velocities in x, y, and z axes and p, q, and r are angular velocities around x, y and z axes, respectively. Ship motion can be expressed by three transitional motions and three rotational motions.

Equations of motion for the transitional motions of a ship are expressed as follows:

$$\left.\begin{aligned} \text{Surge} &= m(\dot{u} + wq - vr) = X_{G0}, \\ \text{Sway} &= m(\dot{v} + ur - wp) = Y_{G0}, \\ \text{Heave} &= m(\dot{w} + vp - uq) = Z_{G0}, \end{aligned}\right\} \tag{2.1}$$

where, m is the ships mass and X_{G0}, Y_{G0}, and Z_{G0} are x, y, and z components of external forces acting on the ship. Assuming x, y, and z axes are principal axes of inertia, equations of motion for the rotational motions of the ship are expressed as follows:

$$\left.\begin{array}{rl} \text{Roll:} & I_{xx}\dot{p} + \left(I_{zz} - I_{yy}\right)qr = L_{G0}, \\ \text{Pitch:} & I_{yy}\dot{q} + (I_{xx} - I_{zz})rp = M_{G0}, \\ \text{Yaw:} & I_{zz}\dot{r} + \left(I_{yy} - I_{xx}\right)pq = N_{G0}, \end{array}\right\} \tag{2.2}$$

where, I_{xx}, I_{yy}, and I_{zz} are the moments of inertia of the ship and L_{G0}, M_{G0}, and N_{G0} are external moments acting on the ship.

Coupling of turning motion and waves induced drifting motion is not so significant when a ship turns in the sea with a small wave. It is expressed by super positioning yawing induced by waves on turning motion in still water. Therefore, when ship manoeuvring is investigated, motions in horizontal plane such as surge, sway, and yaw must be taken into consideration. Coupling of other motions are negligible from a practical point of view. By substituting $w = p = q = 0$ for Eqs. (2.1) and (2.2), the following equations are derived;

$$\left.\begin{array}{rl} \text{Surge:} & m(\dot{u} - vr) = X_{G0}, \\ \text{Sway:} & m(\dot{v} + ur) = Y_{G0}, \\ \text{Yaw:} & I_{zz}\dot{r} \quad\quad = N_{G0}. \end{array}\right\} \tag{2.3}$$

Eq. (2.3) shows standard equations of manoeuvring motion. The equation of roll motion should be added when the manoeuvrability of a ship of which metacentric height $\overline{GM}$ is small and ship speed is fast. The influence of roll motion on the manoeuvrability of such ship is not negligible. In the case of high speed vessel, pitch and surge motions may couple with other motions. When a ship sails in waves, the effect of wave exciting force should be taken into consideration.

2.2.2. Derivation of Equations of Manoeuvring Motion

Equations of motion of a ship in the earth fixed coordinate system $o - x_0 y_0$ in Fig. 2.2 are given by;

$$\left.\begin{aligned} m\ddot{x}_0 &= X_0, \\ m\ddot{y}_0 &= Y_0, \\ I_{zz}\ddot{\psi} &= N_0, \end{aligned}\right\} \tag{2.4}$$

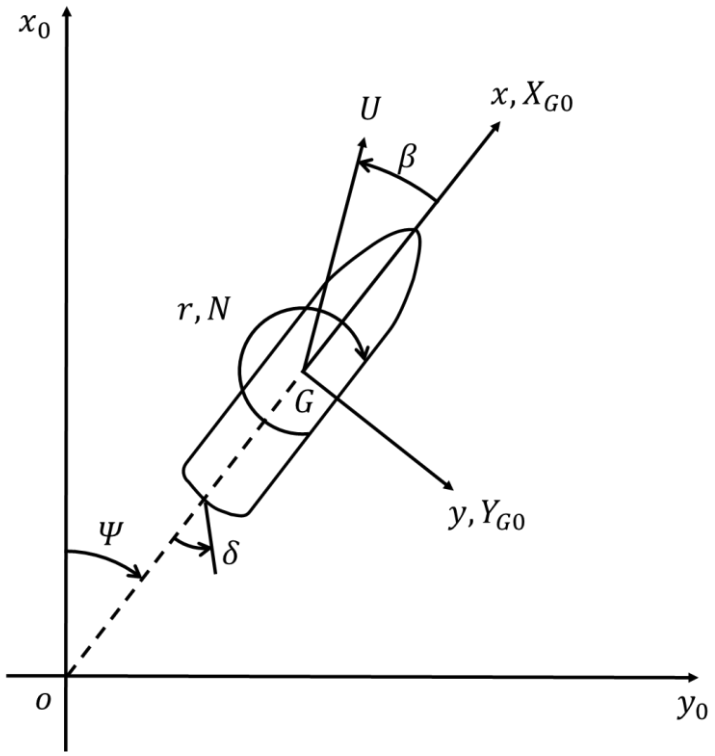

Figure 2.2 Body fixed coordinate system for ship manoeuvring motion

where, m and I_{zz} are ships mass and moment inertia around a vertical axis through G respectively. $\ddot{x}_0$ and $\ddot{y}_0$ represent components of acceleration in x_0 and y_0 axes separately and $\ddot{\psi}(=\dot{r})$ stands for the angular acceleration. X_0 and Y_0 are components of external forces in x_0 and y_0 axes and N_0 is external moment acting on the ship.

When x and y components of external force acting on a ship is expressed by X_{G0} and Y_{G0} in the body fixed coordinate system shown in Fig. 2.2, there is the following relation between X_{G0}, Y_{G0} and X_0, Y_0 which are x_0 and y_0 components in the earth fixed coordinate system.

$$\left.\begin{aligned} X_{G0} &= X_0 \cos\psi + Y_0 \sin\psi\,, \\ Y_{G0} &= Y_0 \cos\psi - X_0 \sin\psi\,. \end{aligned}\right\} \tag{2.5}$$

Substituting Eq. (2.4) for Eq. (2.5), the following equations are obtained;

$$\left.\begin{aligned} X_{G0} &= m(\ddot{x}_0 \cos\psi + \ddot{y}_0 \sin\psi), \\ Y_{G0} &= m(\ddot{y}_0 \cos\psi - \ddot{x}_0 \sin\psi). \end{aligned}\right\} \tag{2.6}$$

Furthermore, $\dot{x}_0, \dot{y}_0$ which are x_0 and y_0 components of the velocity of G in the earth fixed coordinate system is expressed by u and v which are x and y components of the velocity in the body fixed coordinate system.

$$\left.\begin{aligned} \dot{x}_0 &= u\cos\psi\ - v\sin\psi\,, \\ \dot{y}_0 &= v\cos\psi + u\sin\psi\,. \end{aligned}\right\} \tag{2.7}$$

Differentiating Eq. (2.7) by time, x_0 and y_0 components of the acceleration of G is given by;

$$\left.\begin{aligned} \ddot{x}_0 &= \dot{u}\cos\psi - u\dot{\psi}\sin\psi - \dot{v}\sin\psi + v\dot{\psi}\cos\psi\,, \\ \ddot{y}_0 &= \dot{v}\cos\psi - v\dot{\psi}\sin\psi + \dot{u}\sin\psi + u\dot{\psi}\cos\psi\,. \end{aligned}\right\} \tag{2.8}$$

Substituting Eq. (2.8) for Eq. (2.6), then taking $\dot{r} = \ddot{\psi}$ and $N_0 = N_{G0}$ into account, the following equations of motion are derived as follows;

$$\left.\begin{aligned} X_{G0} &= m\big(\dot{u} - v\dot{\psi}\big), \\ Y_{G0} &= m\big(\dot{v} + u\dot{\psi}\big), \\ N_{G0} &= I_{zz}\dot{r}. \end{aligned}\right\} \tag{2.9}$$

The external forces X_{G0}, Y_{G0} and moment N_{G0} are based on the inertia and viscosity of fluid. Separating these components, the forces and moment can be written as follows;

$$\left.\begin{aligned} X_{G0} &= \underline{-m_x\dot{u} + m_y v r} + m_y \alpha r^2 + X, \\ Y_{G0} &= \underline{-m_y\dot{v} - m_x u r} - m_y \alpha\dot{r} + Y, \\ N_{G0} &= \underline{-i_{zz}\dot{r}} - m_y \alpha\dot{v} - \big(m_y - m_x\big)uv - m_y \alpha u r + N, \end{aligned}\right\} \tag{2.10}$$

where, m_x and m_y are x and y components of added mass, I_{zz} is added moment of inertia around G and α represents distance between the point of application of added mass and G. X, Y and N stand for the components of forces and moment due to the viscosity of fluid.

Let us assume that α is negligible small and $-(m_y - m_x)uv$ term can be included in N. Substituting Eq. (2.10) for Eq. (2.9), then moving terms with the underline in the right side of Eq. (2.10) to the left side of Eq. (2.9), the following equations is derived.

$$\left.\begin{aligned} X &= (m + m_x)\dot{u} - (m + m_y)vr, \\ Y &= (m + m_y)\dot{v} + (m + m_x)ur, \\ N &= (I_{zz} + i_{zz})\dot{r}. \end{aligned}\right\} \tag{2.11}$$

Let U and β be the velocity and the drift angle of a ship at the center of gravity G. There is the following relation between U, β and u, v which are x and y components of ship velocity;

$$\left.\begin{aligned} u &= U\cos\beta\,, \\ v &= -U\sin\beta\,. \end{aligned}\right\} \tag{2.12}$$

Substituting Eq. (2.12) for Eq. (2.11), the equations of manoeuvring motion using U and β instead of u and v is derived as follows;

$$\left.\begin{aligned} X &= (m + m_x)(\dot{U}\cos\beta - \dot{\beta}U\sin\beta) + (m + m_y)Ur\sin\beta\,, \\ Y &= -(m + m_y)(\dot{U}\sin\beta + \dot{\beta}U\cos\beta) + (m + m_x)Ur\cos\beta\,, \\ N &= (I_{zz} + i_{zz})\dot{r}. \end{aligned}\right\} \tag{2.13}$$

By non-dimensionalizing Eq. (2.13), the following non-dimensionalized equations of manoeuvring motion is derived.

$$\left.\begin{aligned} X' &= (m' + m_x')\left(\frac{L}{U}\right)\left(\frac{\dot{U}}{U}\cos\beta - \dot{\beta}\sin\beta\right) + (m' + m_y')r'\sin\beta\,, \\ Y' &= -(m' + m_y')\left(\frac{L}{U}\right)\left(\frac{\dot{U}}{U}\sin\beta + \dot{\beta}\cos\beta\right) - (m' + m_x')r'\cos\beta\,, \\ N' &= (I_{zz}' + i_{zz}')\left(\frac{L}{U}\right)^2\left(\frac{\dot{U}}{L}r' + \frac{U}{L}\dot{r}'\right), \end{aligned}\right\} \tag{2.14}$$

where, " $'$ " indicates non-dimensionalized value according to the following equations;

$$\left.\begin{aligned} m', m'_x, m'_y &= \frac{m, m_x, m_y}{\frac{1}{2}\rho L^2 d}, \quad I'_{zz}, i'_{zz} = \frac{I_{zz}, i_{zz}}{\frac{1}{2}\rho L^4 d}, \\ X', Y' &= \frac{X, Y}{\frac{1}{2}\rho L d U^2}, \quad N' = \frac{N}{\frac{1}{2}\rho L^2 d U^2}, \quad r' = \frac{rL}{U}, \end{aligned}\right\} \tag{2.15}$$

where, L and d represent ship length and draft and ρ is the density of the water.

2.3. Mathematical Models for Lateral Force and Yawing Moment

The non-dimensional external forces and moments presented in the left-hand sides of Eq. (2.14) can be expressed by assuming that they consist of hull, propeller, and rudder components as follows,

$$\left.\begin{aligned} X' &= X'_H + X'_P + X'_R, \\ Y' &= Y'_H + Y'_P + Y'_R, \\ N' &= N'_H + N'_P + N'_R. \end{aligned}\right\} \tag{2.16}$$

Subscripts "H", "P" and "R" indicate non-dimensionalized hydrodynamic forces acting on a hull, a propeller, and a rudder, respectively. In this research, only lateral force Y'_H and yawing moment N'_H are investigated deeply due to the dominant influence on the accuracy of manoeuvring prediction.

Furthermore, Hydrodynamic forces and moments acting on a ship change with its motion and their characteristics are different depending on principal dimensions of a ship or types of motions. Therefore, a lot of parameters are necessary to express the hydrodynamic forces. By using the Taylor expansion, the characteristics of the hydrodynamic forces can be diminished into useful mathematical form with several variables. To use the Taylor expansion, the hydrodynamic forces and their derivatives should be continuous and should not go to infinity in the region of the values of the variables under consideration. This assumption holds very well with respect to hydrodynamic bodies, especially ships.

Assuming the value of a function $f(x)$ is desired for a certain value of x, it can be described in terms of the value of the function and its derivatives at some other value of x, say at $x = x_0$. An example of the Taylor expansion for one variable can be described as follow,

$$f(x) = f(x_0) + (x - x_0)\frac{df(x_0)}{dx} + \frac{(x - x_0)^2}{2!}\frac{d^2 f(x_0)}{dx^2} + \frac{(x - x_0)^3}{3!}\frac{d^3 f(x_0)}{dx^3} + \cdots, \tag{2.17}$$

where,

$f(x_0)$: The value of the function at $x = x_0$,

$d^n f(x_0)/dx^n$: The n-th derivative of the function evaluated at $x = x_0$.

Here, the following differential operator are introduced,

$$\partial_x = \frac{d}{dx}, \qquad \partial_x^n = \frac{d^n}{dx^n}, \qquad (x - x_0) = \Delta x, \tag{2.18}$$

Then substituting Eq. (2.18) to Eq. (2.17), the following expression is obtained,

$$\left.\begin{aligned} f(x) &= f(x_0) + \Delta x \partial_x f(x_0) + \frac{(\Delta x \partial_x)^2}{2!} f(x_0) + \frac{(\Delta x \partial_x)^3}{3!} f(x_0) + \cdots, \\ &= \left[1 + (\Delta x \partial_x) + \frac{(\Delta x \partial_x)^2}{2!} + \frac{(\Delta x \partial_x)^3}{3!} + \cdots\right] f(x_0). \end{aligned}\right\} \tag{2.19}$$

Eq. (2.19) is exactly the form for the Taylor series expansion of the exponential,

$$e^a = 1 + a + \frac{a^2}{2!} + \frac{a^3}{3!} + \cdots \ . \tag{2.20}$$

So that, the Taylor series expansion can be expressed as,

$$f(x) = e^{\Delta x \partial_x} f(x_0). \tag{2.21}$$

Moreover, for multiple variables, the Taylor expansion takes the following form,

$$f(x_1, \ldots, x_k) = \sum_{a=0}^{n} \frac{1}{a!}\left(\Delta x_1 \partial_{x_1} + \cdots + \Delta x_k \partial_{x_k}\right)^n f((x_1)_0, \ldots, (x_k)_0). \tag{2.22}$$

When the Taylor expansion is applied for hydrodynamic forces acting on a ship hull, a combination of non-dimensional sway velocity $v'(= v/U)$ and non-dimensional yaw rate r' or a combination of drift angle $\beta(\simeq \sin\beta = -v')$ and r' are often used as the variables such as $x_1, \cdots, x_k$.

Furthermore, there are two kinds of models according to the difference in the adoption of terms existing in the right-hand side of Eq. (2.22). If the third order polynomials are

selected, the Taylor expansion for the hydrodynamic forces acting on a ship hull would be expressed as,

$$f(v',r') = \left[e^{\Delta_{v'}\partial_{v'}+\Delta_{r'}\partial_{r'}+\Delta_{v'}^2\Delta_{r'}\partial_{v'v'r'}+\Delta_{v'}\Delta_{r'}^2\partial_{v'r'r'}+\Delta_{v'}^3\partial_{v'v'v'}+\Delta_{r'}^3\partial_{r'r'r'}}\right] \times f\left[v_0', r_0', {v_0'}^2 r_0', v_0' {r_0'}^2, {v_0'}^3, {r_0'}^3\right], \tag{2.23}$$

or,

$$f(\beta,r') = \left[e^{\Delta_\beta\partial_\beta+\Delta_{r'}\partial_{r'}+\Delta_\beta^2\Delta_{r'}\partial_{\beta\beta r'}+\Delta_\beta\Delta_{r'}^2\partial_{\beta r'r'}+\Delta_\beta^3\partial_{\beta\beta\beta}+\Delta_{r'}^3\partial_{r'r'r'}}\right] \times f\left[\beta_0, r_0', \beta_0^2 r_0', \beta_0 {r_0'}^2, \beta_0^3, {r_0'}^3\right], \tag{2.24}$$

A coupling term $v'r'$ (or $\beta r'$), square terms ${v'}^2$ (or β^2) and ${r'}^2$ and other higher order terms are generally neglected because their contribution is smaller than other terms shown in Eqs. (2.23) and (2.24).

On the other hand, the Taylor expansion with the second order polynomials for the hydrodynamic forces acting on a ship hull would be expressed as,

$$f(v',r') = \left[e^{\Delta_{v'}\partial_{v'}+\Delta_{r'}\partial_{r'}+\Delta_{v'}^2\partial_{v'v'}+\Delta_{r'}^2\partial_{r'r'}+\Delta_{v'}^2\Delta_{r'}\partial_{v'v'r'}+\Delta_{v'}\Delta_{r'}^2\partial_{v'r'r'}}\right] \times f\left[v_0', r_0', {v_0'}^2, {r_0'}^2, {v_0'}^2 r_0', v_0' {r_0'}^2\right], \tag{2.25}$$

or,

$$f(\beta,r') = \left[e^{\Delta_\beta\partial_\beta+\Delta_{r'}\partial_{r'}+\Delta_\beta^2\partial_{\beta\beta}+\Delta_{r'}^2\partial_{r'r'}+\Delta_\beta^2\Delta_{r'}\partial_{\beta\beta r'}+\Delta_\beta\Delta_{r'}^2\partial_{\beta r'r'}}\right] \times f\left[\beta_0, r_0', \beta_0^2, {r_0'}^2, \beta_0^2 r_0', \beta_0 {r_0'}^2\right]. \tag{2.26}$$

As same as the third order polynomials, a coupling term $v'r'$ (or $\beta r'$) and other higher order terms are generally neglected.

Therefore, mathematical models based on the Taylor series expansion about v' (or β) and r' are often expressed as follows,

$$\left.\begin{aligned} Y_H' &= Y_v' v' + Y_r' r' + Y_{NL}'(v',r'), \\ N_H' &= N_v' v' + N_r' r' + N_{NL}'(v',r'), \end{aligned}\right\} \tag{2.27}$$

or,

$$\left.\begin{aligned} Y'_H &= Y'_v v' + Y'_r r' + Y'_{NL}(\beta, r'), \\ N'_H &= N'_v v' + N'_r r' + N'_{NL}(\beta, r'), \end{aligned}\right\} \tag{2.28}$$

where, Y'_v, Y'_r, N'_v and N'_r $\left(Y'_\beta, Y'_r, N'_\beta \text{ and } N'_r\right)$ are linear hydrodynamic derivatives and Y'_{NL} and N'_{NL} indicate nonlinear terms. Combination of linear terms which are represented by the functions of v' (or β) and r' and their orders in the nonlinear terms are different according to research institutes.

The third order model based on non-dimensional sway velocity v' (Yasukawa and Yoshimura, 2015) is expressed by the following equations using the ship fixed coordinate system $G - xy$ shown in Fig. 2.2,

$$\left.\begin{aligned} Y'_H &= Y'_v v' + Y'_r r' + Y'_{vvv} v'^3 + Y'_{vvr} v'^2 r' + Y'_{vrr} v' r'^2 + Y'_{rrr} r'^3, \\ N'_H &= N'_v v' + N'_r r' + N'_{vvv} v'^3 + N'_{vvr} v'^2 r' + N'_{vrr} v' r'^2 + N'_{rrr} r'^3. \end{aligned}\right\} \tag{2.29}$$

Here, Y'_H and N'_H are the non-dimensional values of lateral force and yawing moment. The second order model based on drift angle β which has been conventionally adopted by Kyushu University (Kijima et al., 1990) is expressed by the following equations,

$$\left.\begin{aligned} Y'_H &= Y'_\beta \beta + Y'_r r' + Y'_{\beta\beta} \beta|\beta| + Y'_{rr} r'|r'| + \left(Y'_{\beta\beta r}\beta + Y'_{\beta rr} r'\right)\beta r', \\ N'_H &= N'_\beta \beta + N'_r r' + N'_{\beta\beta} \beta|\beta| + N'_{rr} r'|r'| + \left(N'_{\beta\beta r}\beta + N'_{\beta rr} r'\right)\beta r'. \end{aligned}\right\} \tag{2.30}$$

To express the change in the sign of the hydrodynamic force depending on the direction of motion, absolute symbols are added to the second order model terms of β and r'. The first model shown in Eq. (2.29) is the "cubic model" and the second model shown in Eq. (2.30) is the "quadratic model", respectively.

2.4. Calculation Conditions

Based on the two models shown in Eqs. (2.29) and (2.30), hydrodynamic forces measured by captive model tests for 12 model ships shown in Table 2.1 (total of 27 loading conditions) were reanalyzed to obtain hydrodynamic derivatives for the cubic model and the quadratic model. In Table 2.1, β is the range of drift angle where the hydrodynamic forces were measured, L is the length of a ship, B is a ship width, d_m is an average draft, and C_B is a block coefficient. SR108 and Esso Osaka are ships whose hull shapes, various experimental data and calculation results are widely disclosed. Ships A to J are ship types used in the captive model tests conducted at Kyushu University. For all these ships, there

are measurement data of hydrodynamic forces for fully loaded and ballast conditions, and for Ships D, F, and I, measurement of hydrodynamic forces for half loaded condition is also performed. Hydrodynamic derivatives derived from the measurements of the captive model tests for all ships for the cubic model and the quadratic model are shown in Tables 2.2 and 2.3, respectively.

Table 2.1 Principal dimensions of model ships

Ship No.	Ship Name	Ship Type	Loading Condition	β (deg.)	L (m)	B (m)	d_m (m)	C_B
1	SR108	Container C.	Fully loaded	-4.0 ~12.0	3.0	0.435	0.163	0.572
2			Ballast				0.094	0.518
3	Esso Osaka	VLCC	Fully loaded	-4.0 ~20.0	2.5	0.408	0.170	0.831
4			Ballast				0.080	0.793
5	Ship A	Car C.	Full loaded	-4.0 ~10.0	2.5	0.482	0.134	0.522
6			Ballast				0.111	0.491
7	Ship B	Cargo C.	Fully loaded	-4.0 ~10.0	2.5	0.419	0.140	0.698
8			Ballast				0.082	0.666
9	Ship C	ULCC	Fully loaded	-4.0 ~20.0	2.5	0.466	0.156	0.835
10			Ballast				0.076	0.802
11	Ship D	LNG C.	Fully loaded	-4.0 ~20.0	2.5	0.409	0.100	0.714
12			Half loaded				0.093	0.707
13			Ballast				0.086	0.703
14	Ship E	VLCC	Fully loaded	-4.0 ~20.0	2.5	0.436	0.157	0.802
15			Ballast				0.077	0.761
16	Ship F	Container C.	Fully loaded	-4.0 ~20.0	2.5	0.386	0.130	0.566
17			Half loaded				0.107	0.540
18			Ballast				0.085	0.516
19	Ship G	Cargo C.	Fully loaded	-4.0 ~20.0	2.5	0.376	0.158	0.651
20			Ballast				0.072	0.574
21	Ship H	Cargo C.	Fully loaded	-4.0 ~20.0	2.5	0.408	0.171	0.773
22			Ballast				0.071	0.711
23	Ship I	RO/RO	Fully loaded	-4.0 ~20.0	2.5	0.367	0.102	0.557
24			Half loaded				0.093	0.537
25			Ballast				0.083	0.512
26	Ship J	ULCC	Fully loaded	-4.0 ~20.0	2.5	0.556	0.183	0.821
27			Ballast				0.089	0.783

Table 2.2 Hydrodynamic derivatives for cubic model

Ship No.	Y'_v	Y'_{vvv}	Y'_r	Y'_{rrr}	Y'_{vrr}	Y'_{vvr}	N'_v	N'_{vvv}	N'_r	N'_{rrr}	N'_{vrr}	N'_{vvr}
1	0.234	3.272	-0.119	0.020	1.128	0.012	0.111	-0.288	-0.044	-0.047	-0.083	-0.579
2	0.202	2.073	-0.124	0.051	0.938	-0.268	0.062	-0.137	-0.030	-0.056	0.043	-0.554
3	0.430	1.452	-0.238	0.059	0.498	0.280	0.154	0.058	-0.071	-0.008	-0.117	-0.169
4	0.335	0.759	-0.235	0.016	0.376	0.134	0.079	0.075	-0.056	-0.011	-0.029	-0.187
5	0.346	2.437	-0.187	-0.109	1.085	-1.094	0.109	1.061	-0.069	-0.027	0.061	-0.605
6	0.317	7.566	-0.175	-0.097	0.811	-1.932	0.087	0.723	-0.063	-0.032	0.115	-0.684
7	0.320	4.768	-0.109	-0.060	0.521	-0.831	0.108	-0.088	-0.054	-0.024	-0.054	-0.228
8	0.229	3.252	-0.110	-0.165	0.830	-0.878	0.066	-0.088	-0.045	-0.017	0.057	-0.366
9	0.479	0.975	-0.269	-0.025	0.270	0.569	0.134	0.023	-0.055	-0.013	-0.018	-0.177
10	0.371	0.613	-0.247	-0.055	0.202	0.182	0.065	0.099	-0.043	-0.005	0.007	-0.168
11	0.359	0.948	-0.203	-0.005	0.281	0.153	0.076	-0.003	-0.044	-0.007	-0.017	-0.147
12	0.333	0.644	-0.193	-0.028	0.281	0.192	0.070	0.018	-0.042	-0.006	-0.006	-0.148
13	0.321	0.574	-0.193	-0.017	0.259	0.234	0.067	-0.033	-0.037	-0.010	-0.008	-0.116
14	0.381	1.559	-0.221	0.023	0.531	0.047	0.127	0.012	-0.059	-0.013	-0.099	-0.164
15	0.321	0.591	-0.205	-0.018	0.277	0.303	0.065	0.087	-0.046	-0.018	-0.030	-0.137
16	0.280	3.498	-0.101	-0.055	1.036	-1.891	0.093	0.089	-0.048	-0.040	0.012	-0.350
17	0.281	2.177	-0.093	-0.070	0.903	-1.246	0.076	0.067	-0.043	-0.042	0.073	-0.410
18	0.284	2.156	-0.089	-0.078	0.829	-1.215	0.063	0.169	-0.035	-0.042	0.076	-0.462
19	0.354	2.167	-0.155	-0.009	0.897	-0.901	0.125	0.095	-0.058	-0.041	-0.066	-0.275
20	0.247	1.034	-0.128	-0.035	0.600	-0.478	0.056	0.086	-0.031	-0.036	0.043	-0.341
21	0.295	2.470	-0.176	-0.023	0.546	-0.129	0.145	-0.157	-0.047	-0.026	-0.120	-0.135
22	0.320	0.484	-0.199	-0.031	0.283	0.273	0.064	-0.062	-0.038	-0.015	-0.072	-0.021
23	0.238	2.196	-0.124	-0.073	0.854	-1.486	0.075	0.213	-0.035	-0.033	0.123	-0.564
24	0.231	2.003	-0.144	-0.020	0.781	-1.259	0.067	0.199	-0.032	-0.039	0.146	-0.601
25	0.215	2.672	-0.124	-0.056	0.917	-1.733	0.058	0.322	-0.034	-0.041	0.166	-0.663
26	0.476	1.538	-0.278	-0.031	0.269	0.492	0.151	0.139	-0.056	-0.024	-0.056	-0.201
27	0.352	0.458	-0.285	-0.018	0.109	0.482	0.071	0.115	-0.048	-0.008	0.006	-0.215

Table 2.3 Hydrodynamic derivatives for quadratic model

Ship No.	Y'_{β}	$Y'_{\beta\beta}$	Y'_{r}	Y'_{rr}	$Y'_{\beta rr}$	$Y'_{\beta\beta r}$	N'_{β}	$N'_{\beta\beta}$	N'_{r}	N'_{rr}	$N'_{\beta rr}$	$N'_{\beta\beta r}$
1	0.179	0.899	-0.124	0.021	1.280	-0.427	0.118	-0.093	-0.034	-0.044	-0.151	-0.384
2	0.163	0.591	-0.135	0.049	0.994	-0.451	0.065	-0.047	-0.019	-0.052	-0.007	-0.410
3	0.372	0.601	-0.251	0.060	0.547	0.138	0.155	0.007	-0.068	-0.011	-0.128	-0.140
4	0.294	0.344	-0.240	0.020	0.404	0.049	0.074	0.034	-0.052	-0.013	-0.033	-0.174
5	0.409	-0.008	-0.141	-0.151	1.244	-1.771	0.091	0.279	-0.056	-0.041	0.073	-0.744
6	0.274	1.484	-0.132	-0.136	0.930	-2.716	0.073	0.203	-0.047	-0.048	0.125	-0.768
7	0.272	1.060	-0.082	-0.085	0.500	-0.719	0.110	-0.029	-0.043	-0.034	-0.088	-0.018
8	0.197	0.712	-0.043	-0.225	0.871	-1.143	0.068	-0.027	-0.038	-0.023	0.064	-0.399
9	0.435	0.405	-0.257	-0.037	0.277	0.541	0.136	-0.004	-0.049	-0.019	-0.023	-0.155
10	0.345	0.248	-0.223	-0.077	0.240	0.077	0.061	0.039	-0.041	-0.007	0.005	-0.157
11	0.323	0.383	-0.199	-0.009	0.279	0.146	0.076	-0.005	-0.040	-0.010	-0.012	-0.158
12	0.300	0.285	-0.179	-0.042	0.250	0.261	0.068	0.006	-0.040	-0.008	-0.011	-0.134
13	0.288	0.262	-0.185	-0.024	0.260	0.216	0.069	-0.019	-0.033	-0.013	-0.014	-0.093
14	0.305	0.695	-0.231	0.032	0.604	-0.185	0.125	0.003	-0.052	-0.020	-0.115	-0.111
15	0.297	0.236	-0.197	-0.025	0.302	0.220	0.061	0.035	-0.038	-0.026	-0.031	-0.126
16	0.127	1.530	-0.079	-0.075	1.093	-2.077	0.089	0.035	-0.029	-0.057	-0.006	-0.283
17	0.180	0.969	-0.064	-0.096	0.926	-1.321	0.073	0.026	-0.025	-0.060	0.065	-0.373
18	0.185	0.953	-0.057	-0.106	0.876	-1.345	0.056	0.071	-0.016	-0.059	0.067	-0.417
19	0.263	0.930	-0.148	-0.016	0.957	-1.111	0.123	0.027	-0.039	-0.059	-0.071	-0.241
20	0.203	0.441	-0.112	-0.051	0.624	-0.563	0.053	0.033	-0.014	-0.052	0.025	-0.282
21	0.179	1.102	-0.167	-0.032	0.591	-0.305	0.156	-0.091	-0.035	-0.038	-0.139	-0.064
22	0.307	0.170	-0.185	-0.045	0.276	0.271	0.069	-0.037	-0.031	-0.021	-0.085	0.021
23	0.143	0.956	-0.093	-0.101	0.851	-1.487	0.065	0.095	-0.020	-0.047	0.092	-0.461
24	0.140	0.890	-0.133	-0.031	0.748	-1.170	0.059	0.082	-0.015	-0.055	0.121	-0.509
25	0.092	1.192	-0.097	-0.081	0.943	-1.806	0.044	0.139	-0.016	-0.059	0.152	-0.605
26	0.416	0.633	-0.264	-0.044	0.300	0.371	0.147	0.045	-0.046	-0.034	-0.063	-0.173
27	0.334	0.179	-0.277	-0.025	0.112	0.445	0.067	0.043	-0.044	-0.011	0.001	-0.194

2.5. Course Stability Index

Based on the linear hydrodynamic derivatives presented in Eqs. (2.29) and (2.30), course stability index Δ can be calculated by the following equation,

$$\Delta = -Y_v' N_r' + N_v' \{Y_r' - (m' + m_x')\} = Y_\beta' N_r' - N_\beta' \{Y_r' - (m' + m_x')\}. \tag{2.31}$$

The condition for determining whether the course stability of a ship is stable or unstable is shown by the sign of Δ, namely positive Δ means the ship is unstable and negative Δ means the ship is stable.

On the other hand, Eq. (2.31) can be rewritten as follows,

$$\begin{aligned} \Delta &= -Y_v' \{Y_r' - (m' + m_x')\} \left\{ \frac{N_r'}{Y_r' - (m' + m_x')} - \frac{N_v'}{Y_v'} \right\} \\ &= -Y_v' \{Y_r' - (m' + m_x')\} (l_r' - l_v'), \end{aligned} \tag{2.32}$$

$$\begin{aligned} \Delta &= Y_\beta' \{Y_r' - (m' + m_x')\} \left\{ \frac{N_r'}{Y_r' - (m' + m_x')} - \frac{N_\beta'}{Y_\beta'} \right\} \\ &= Y_\beta' \{Y_r' - (m' + m_x')\} \left(l_r' - l_\beta' \right), \end{aligned} \tag{2.33}$$

where,

$$l_r' = \frac{N_r'}{Y_r' - (m' + m_x')}, \qquad l_v' = \frac{N_v'}{Y_v'}, \qquad l_\beta' = \frac{N_\beta'}{Y_\beta'}. \tag{2.34}$$

l_r' indicates the position of yaw damping force application point and both l_v' and l_β' represent the position of sway damping force application point. The course stability of a ship can also be evaluated by the relative positions of these force application points. If the yaw damping force application point exists in front of the sway damping force application point, the ship is stable, otherwise the ship becomes unstable.

The course stability indices both for the cubic model and the quadratic model are compared to see the influence of different model approach based on Eqs. (2.31) to (2.34). Fig. 2.3 shows linear hydrodynamic derivatives obtained by analyzing measured hydrodynamic forces based on the cubic and the quadratic models. They are used to calculate the course stability indices.

Fig. 2.4 shows comparison between calculated course stability indices based on the cubic and the quadratic models for all model ships and loading conditions shown in Table 2.1. The horizontal axis represents the number of ships (1 to 27). It can be observed that some ships have different signs of course stability indices for the cubic and the quadratic models. There are some factors that may cause the difference between the two models. One of the causes is likely happen because of the difference in the mathematical characteristics of both models.

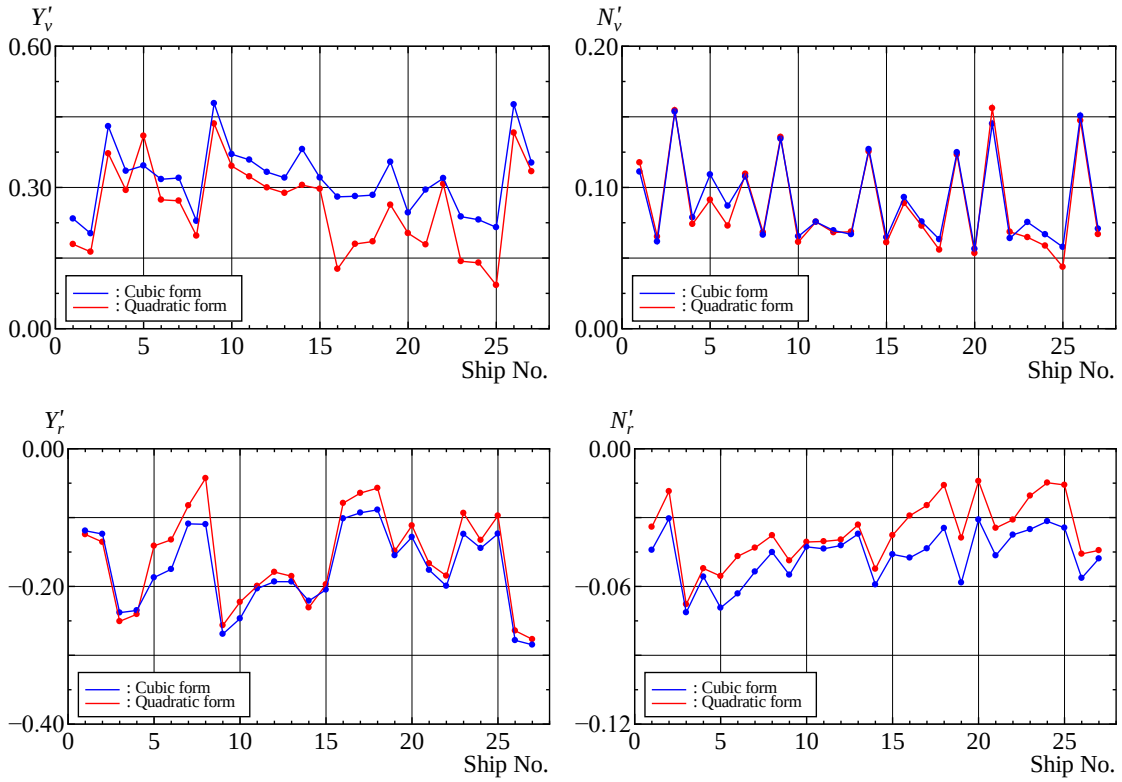

Figure 2.3 Linear hydrodynamic derivatives based on cubic and quadratic models

To have better understanding about the phenomenon, relation between course stability index and the linear hydrodynamic derivatives of the cubic and the quadratic models for all ships are examined. Then, all the 27 ships are divided into three categories for easier understanding based on the results of calculated course stability index:

I. Ships which have the same sign of Δ for the cubic and the quadratic models on all loading conditions.

II. Ships which have the different sign of Δ for the cubic and the quadratic models on some loading conditions.

III. Ships which have the different sign of Δ for the cubic and the quadratic models on all loading conditions.

Fig. 2.5 shows examples for the three categories. Furthermore, Table 2.4 shows the distribution of the ships which are suitable for each category.

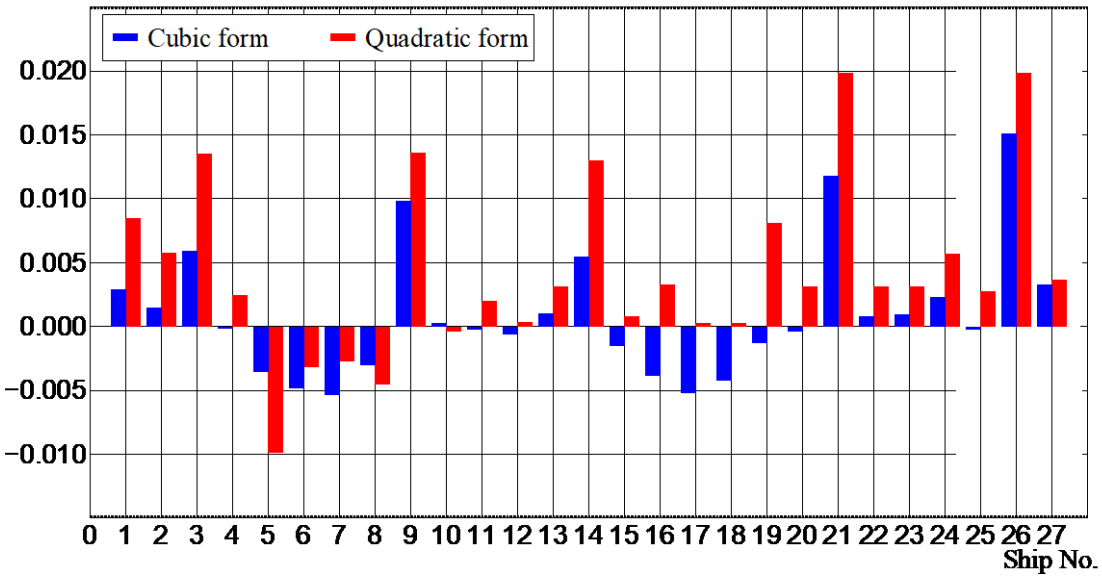

Figure 2.4 Course stability index Δ for cubic model vs quadratic model

Table 2.4 List of ships

Category I	Category II	Category III
SR108	Esso Osaka	Ship F
Ship A	Ship C	Ship G
Ship B	Ship D	
Ship H	Ship E	
Ship J	Ship I	

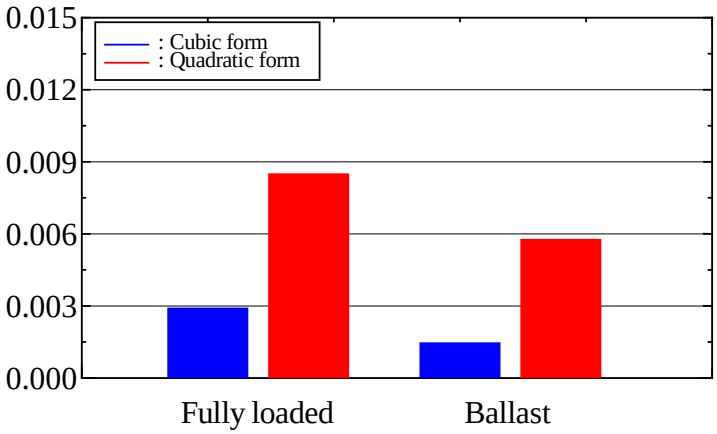

(a) Category I – SR108

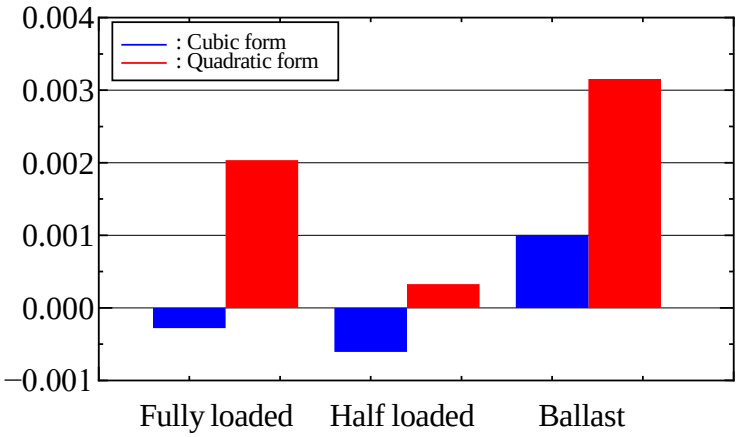

(b) Category II – Ship C

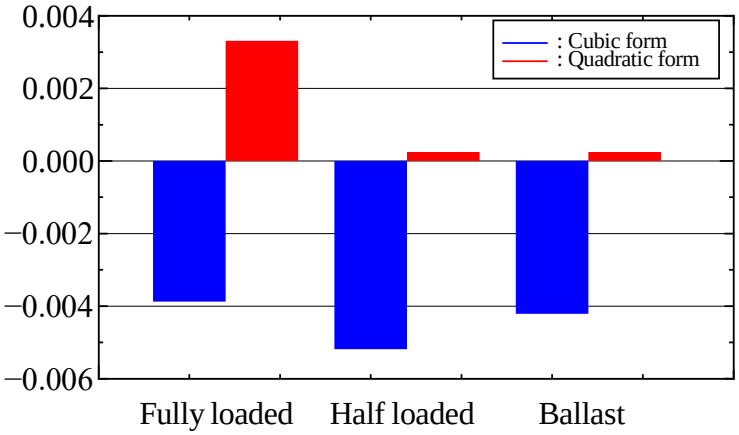

(c) Category III – Ship F

Figure 2.5 Examples of course stability index Δ for three categories

For category I, Fig. 2.6 shows the Y'_H and N'_H curves of SR108 (Ships No. 1 and 2) for fully loaded and ballast conditions respectively fit by the cubic and the quadratic models in the range of $-10° < \beta < 20°$ at $r' = 0$. The horizontal axis represents drift angle β. Red and blue solid lines show fitting curves using the hydrodynamic derivatives for the cubic and the quadratic models derived from captive model test data. Dash lines shown in the figures represent the slopes of the lateral force and yawing moment curves at the origin. They are equivalent with the linear hydrodynamic derivatives for β. Hereafter, the dash line is noted as a slope line. Furthermore, the experimental data are also presented in the figures by circle marks. It is observed that the inclination of the slope line of the cubic model for lateral force has a larger value than that of the quadratic model. On the other hand, it shows opposite tendency for yawing moment. These tendencies are found in both loading conditions.

There is large difference between Y'_H and N'_H curves fit by the cubic and the quadratic models in the large range of drift angle β. Generally, fitting curve using a cubic function based on least square method gives larger value outside the range of input data comparing with fitting curve using a quadratic function. Therefore, it is considered that this difference is caused by the lack of experimental data in the range of large drift angle.

For category II, Fig. 2.7 shows the Y'_H and N'_H curves of Ship C (Ships No. 9 and 10) for fully loaded and ballast conditions, respectively. The difference of Δ signs between Ships No. 9 and 10 are mainly caused by the difference in a slope line of yawing moment with respect to drift angle β. In both ships, the inclination of a slope line of the quadratic model for lateral force with respect to β has a smaller value than that of the cubic model. Different tendency can be observed for yawing moment. On the Ship No. 9, the inclination of a slope line of the quadratic model with respect to β is slightly larger than that of the cubic model. While on the Ship No. 10, the opposite tendency is observed. This tendency is not shown in category I, which is all the Δ have the same sign. The different sign of Δ caused by the difference in the slope lines is coming from the difference of linear hydrodynamic derivative between two models as shown in Fig. 2.10.

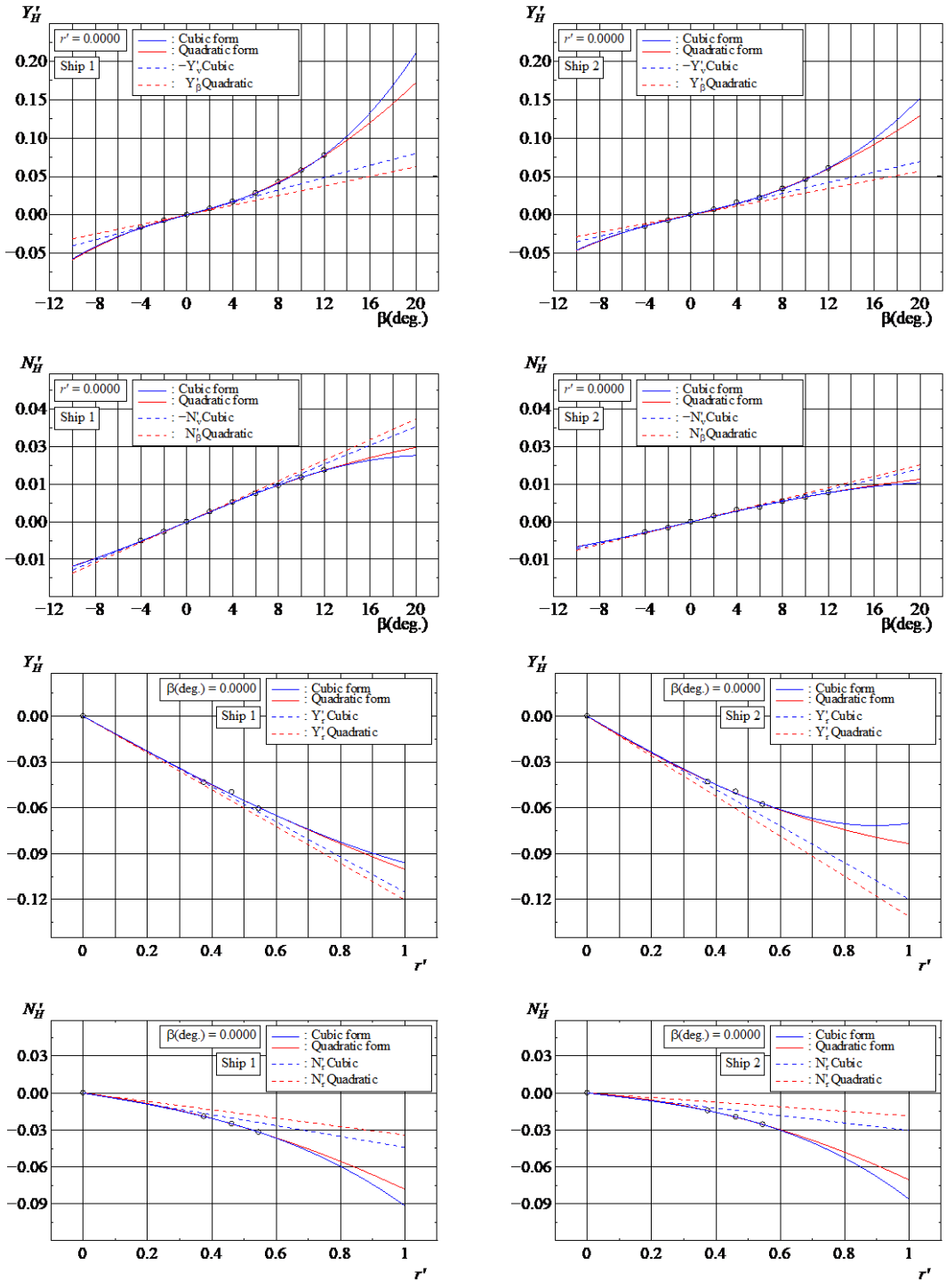

(a) Fully loaded condition (b) Ballast condition

Figure 2.6 Category I - Y'_H and N'_H curves of SR108 fit by cubic and quadratic models for fully loaded and ballast conditions

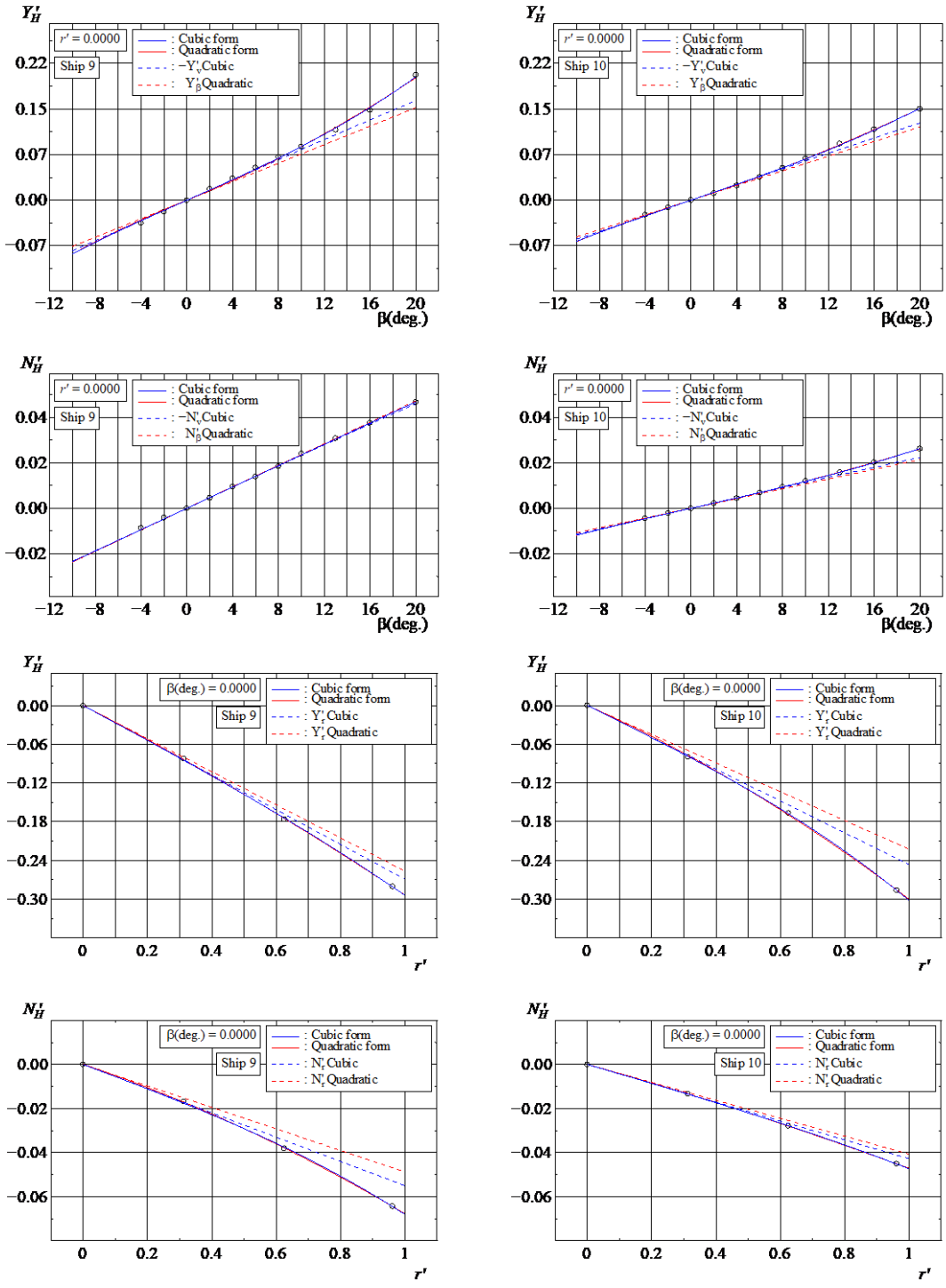

(a) Fully loaded condition (b) Ballast condition

Figure 2.7 Category II - Y'_H and N'_H curves of Ship C fit by cubic and quadratic models for fully loaded and ballast conditions

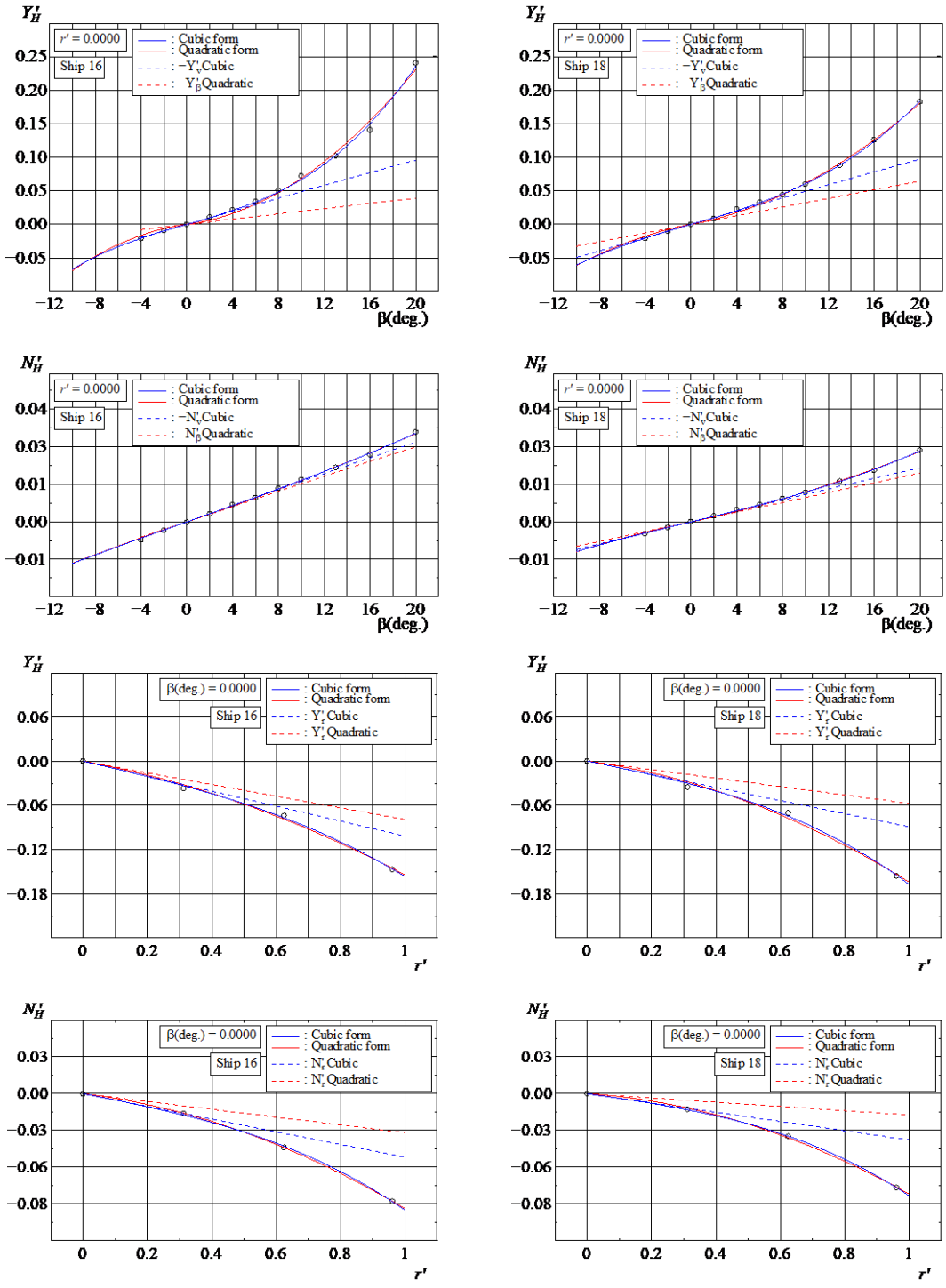

(a) Fully loaded condition (b) Ballast condition

Figure 2.8 Category III - Y'_H and N'_H curves of Ship F fit by cubic and quadratic models for fully loaded and ballast conditions

For category III, Fig. 2.8 shows the Y'_H and N'_H curves of Ship F (Ships No. 16 and 18) for fully loaded and ballast conditions, respectively. There is no significant difference between Y'_H and N'_H curves for fully loaded and ballast conditions. However, the inclination of a slope line of the quadratic model is smaller than that of the cubic model for lateral force and yawing moment with respect to drift angle β. On the other hand, the inclination of a slope line of the quadratic model for lateral force and yawing moment with respect to non-dimensional yaw rate r' is larger than that of the cubic model. This tendency can also be observed in Fig. 2.3.

Previously, comparison between loading conditions to examine the difference of the value of course stability index Δ and hydrodynamic derivatives between the cubic and the quadratic models with the same ship types are focused on. There is a lot of ships that have a different sign of Δ between the cubic and the quadratic models. It is important to know the reason why both models have such results of Δ. Based on that, ships in each category are compared again.

By checking the values of the first and second terms of course stability index shown in Eq. (2.30), which consists of two terms of the combinations of linear hydrodynamic derivatives, it can be easily know that the main cause of the different results between the cubic and the quadratic models. Fig. 2.9 shows the comparison between the absolute values of the first and second terms of course stability index Δ for all ships and both models. The ships which have different sign of Δ mainly have different values of linear derivatives between the cubic and the quadratic models. For example, Ship No. 17 has a different sign of course stability index. Based on Fig. 2.9, the absolute value of $Y'_\beta N'_r$ is smaller than that of $N'_\beta\{Y'_r - (m' + m'_x)\}$ in the quadratic model, but the cubic model shows the opposite. This opposite relation comes from the differences in the characteristics of the cubic and the quadratic functions. If the nonlinearity of measured data is small, a quadratic function generally has a small linear derivative comparing with that of the cubic model. As shown in Fig. 2.9 where almost all the absolute values of the first and second terms of course stability index for the quadratic model is smaller than those of the cubic model.

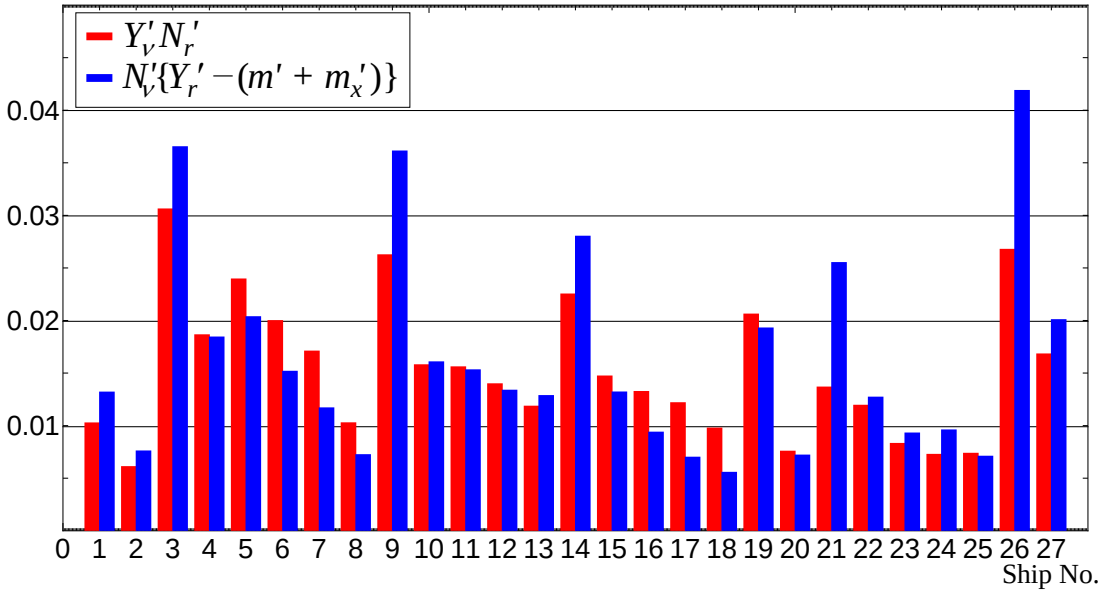

(a) Cubic model

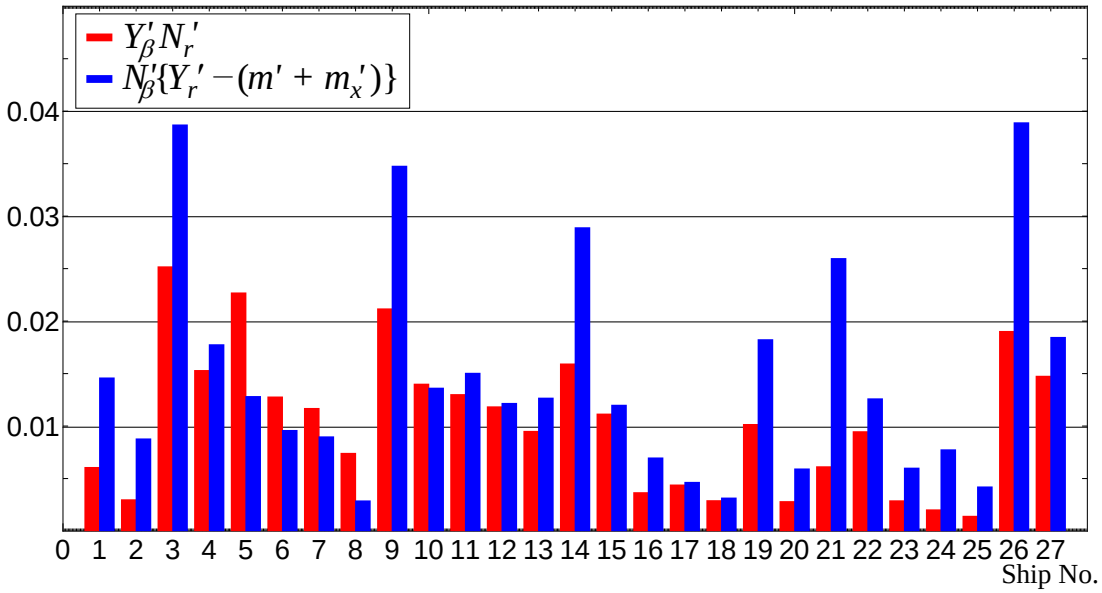

(b) Quadratic model

Figure 2.9 Comparison of the absolute value of linear derivatives

Furthermore, almost all the different signs of Δ between the cubic and the quadratic models are observed for ships having fully loaded and ballast conditions such as Esso Osaka (Ships No. 3 and 4), Ship C (Ships No. 9 and 10), Ship D (Ships No. 11 to 13), Ship E (Ships No. 14 and 15), and Ship I (Ships No. 23 to 25), though there are some exceptions like Ship F (Ships No. 16 to 18) and Ship G (Ships No. 19 and 20). Both of ship F and ship G have different signs of Δ between the cubic and the quadratic models in all loading conditions.

In the category I, both models always show identical results whether the value of $Y'_\beta N'_r$ is larger than $N'_\beta\{Y'_r - (m' + m'_x)\}$ or vice versa. Differently, ships in categories II and III share the same tendency. The value of $Y'_\beta N'_r$ is larger than that of $N'_\beta\{Y'_r - (m' + m'_x)\}$ for the quadratic model but not for the cubic model. It suggests that taking more attention to the difference between the values of linear hydrodynamic derivatives based on the cubic model or the quadratic model when evaluating course stability index for ballast condition.

Next, ships from category I and ships from category II or III for all loading conditions are compared. In this case, SR108 (Ships No. 1 and 2) from category I and Ship F (Ships No. 16 and 18) from category III are chosen because both ships are container carriers, but have different tendency in course stability index to be investigated.

Fig. 2.10 shows the comparison of the absolute values of the first and the second terms of Eq. (2.30) between Ship No. 1 and Ship No. 16. Based on the figure, both of the cubic and the quadratic models for Ship No. 1, the absolute value of $Y'_\beta N'_r$ is smaller than the value of $N'_\beta\{Y'_r - (m' + m'_x)\}$. On the other hand, only the cubic model for Ship No. 16 shows the opposite result. As already explained before, this difference in the absolute values of the first and second terms of Eq. (2.30) is mainly comes from the lack of experimental data and the mathematical characteristics between the two models.

It is confirmed that existence of measured hydrodynamic forces in the large range of drift angle tends to give different result between the cubic and the quadratic models. For the purpose to investigate more the difference between the two models when calculating course stability index, the application points of yaw damping force and sway damping

force for all ships are examined. Fig. 2.11 shows the comparison of course stability index evaluated by the relative positions of l'_r and l'_β or l'_v for both models. Noticed that the quadratic model tends to have a minus value than the cubic model.

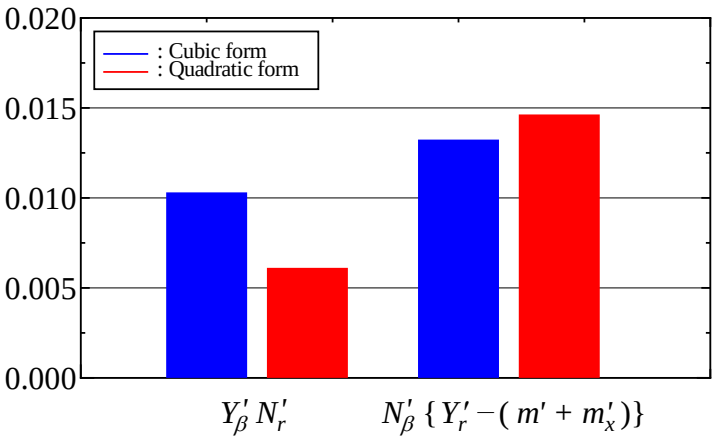

(a) Ship No. 1

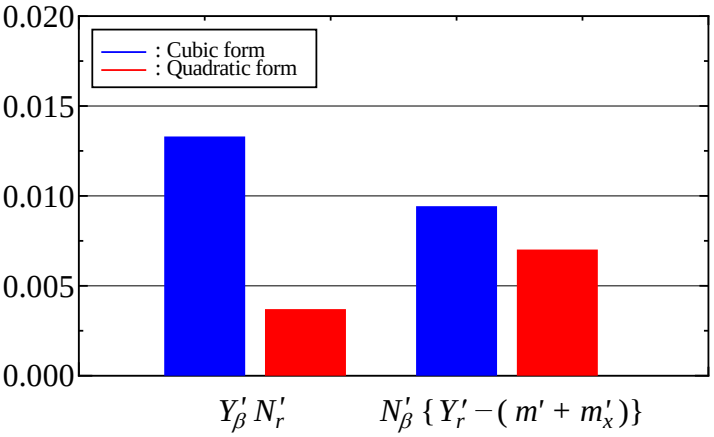

(b) Ship No. 16

Figure 2.10 Comparison of $Y'_\beta N'_r$ and $N'_\beta \{Y'_r - (m' + m'_x)\}$

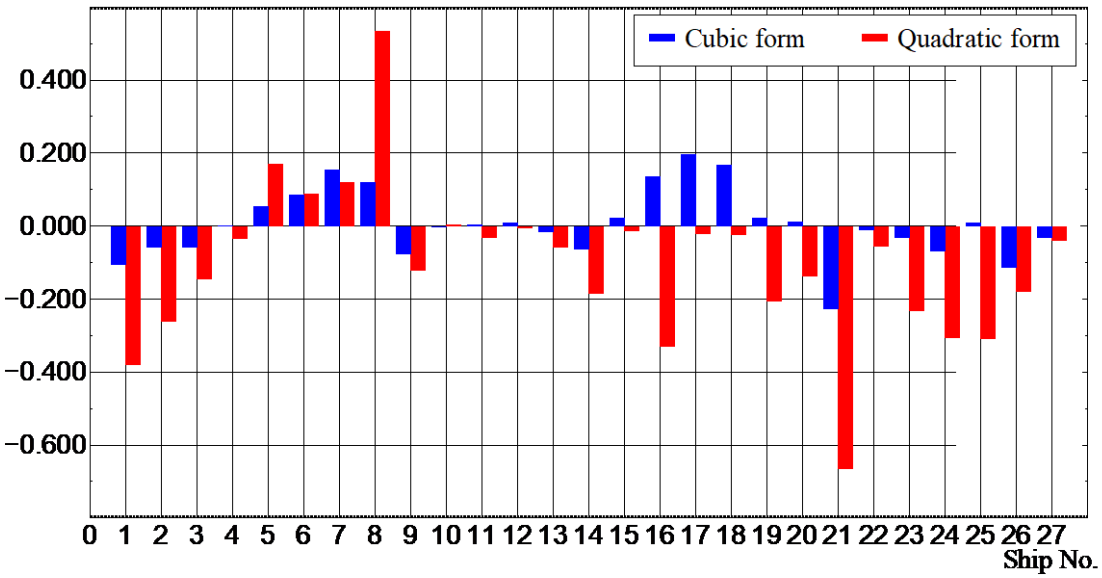

Figure 2.11 Comparison of $l'_r - l'_v$ (for cubic model) and $l'_r - l'_\beta$ (for quadratic model)

2.6. Conclusion

The equations of manoeuvring motion have been presented. Two kinds of mathematical model for lateral force and yawing moment based on cubic polynomials and quadratic polynomials are also represented.

The results of course stability index between the cubic and the quadratic models are reviewed. The different sign of course stability index caused by the difference of linear hydrodynamic derivative between the two models. The first and second terms of course stability index are also investigated. Almost all the absolute values of the first and second terms of course stability index for the quadratic model is smaller than those of the cubic model. It is confirmed that existence of measured hydrodynamic forces in the large range of drift angle tends to give different result between the cubic and the quadratic models. It suggests that taking more attention to the difference between the values of linear hydrodynamic derivatives based on the cubic model or the quadratic model when evaluating course stability index for ballast condition.

Chapter 3 Sensitivity Analysis on Simulated Manoeuvring Motion

3.1. Introduction

Sensitivity analysis is the study of how uncertainty in the output of a model can be apportioned to different sources of uncertainty in a model input (Saltelli, 2002). It may be used to determine input variables that contribute the most to an output behaviour, and non-influential inputs, or to ascertain some interaction effects within the model. The process of sensitivity analysis leads to the analysis and computation of the indicator influence of input variables with respect to the output of the model. The measurement of each undetermined input variable on the response uncertainty provides a deeper understanding of the modelling to reduce the response uncertainties in the most effective way (Helton et al., 2006, Kleijnen, 1997, Saltelli et al., 2000).

There are several approaches to sensitivity analysis. One approach to sensitivity analysis is global sensitivity analysis, often implemented using probabilistic tools and numerous statistical such as regression, statistical learning, and Monte Carlo Simulations. A sensitivity analysis is considered to be global when all the input factors are varied simultaneously and the sensitivity is evaluated over the entire range of each input factor (Zhou and Lin, 2008). Global sensitivity analysis does not distinguish any initial set of model input values, but considers the numerical model in the entire domain of possible input parameter variations (Saltelli et al., 2000).

Another approach is local sensitivity analysis, which is derivative based (numerical or analytical). Mathematically, the sensitivity of the cost function with respect to certain parameters is equal to the partial derivative of the cost function with respect to those parameters (Turanyi, 1990). The term local refers to the fact that all derivatives are taken at a single point. For simple cost functions, this approach is efficient. However, this approach can be infeasible for complex models, where formulating the cost function (or the partial derivatives) is nontrivial. For example, models with discontinuities do not always have derivatives.

There are various uses of sensitivity analysis; one can mention model verification and understanding, model simplifying, factor prioritization, model calibration, and assisting with the decision-making process.

In manoeuvring studies, sensitivity analysis provides a basis for determining the importance and the required accuracy of the individual terms in the mathematical model. This is done through analysis of simulations performed with systematic variations of each term. Such studies have been stimulated by the need for more accurate manoeuvring predictions at the design stage.

In this chapter, sensitivity of simulated ship manoeuvring motion to hydrodynamic derivatives derived from measured lateral force and yawing moment including measurement error coming from the resolution of measurement equipment, fluctuation of towing speed and angular velocity of a carriage, setting error in drift angle, and so on is investigated for a model ship of KVLCC2. The Monte Carlo simulation method is used to analyze the sensitivity. Varying the assumed values of measurement error randomly, evaluation indices such as advance, transfer and tactical diameter for turning motion and the first and the second overshoot angles for 10°/10° and 20°/20° zigzag manoeuvres are evaluated to quantify the influence of the measurement error on manoeuvring performance. By assuming the measurement error, close relation between linear and non-linear derivatives can be included in the sensitivity analyses.

Furthermore, it is well known that linear hydrodynamic derivatives based on a cubic polynomials and a quadratic polynomials have different values even if same dataset of measured hydrodynamic forces are used to drive the derivatives due to the difference of fitting characteristics between the two models. Therefore, the author also focuses on the difference of the sensitivity between hydrodynamic derivatives based on the cubic model and the quadratic model and clarify the advantages and the disadvantages of both models.

3.2. Influence of Measurement Error on Hydrodynamic Derivatives

To evaluate ship manoeuvrability based on numerical simulations, hydrodynamic derivatives which is necessary to express lateral force and yawing moment acting on a ship hull are one of parameters which have much influence on simulated results. It is important to use accurate hydrodynamic derivatives to simulate ship manoeuvring motion

precisely. The Monte Carlo simulation method has been often used to investigate the sensitivity of ship manoeuvrability to the hydrodynamic derivatives, by varying the value of each derivative randomly (Dash et al., 2015, Shenoi et al., 2015, Sung et al., 2014, Shin et al., 2012).

In these investigations, hydrodynamic derivatives are randomly changed one by one, independently. However, it is well known that there is strong relation between linear and non-linear derivatives. Therefore, it is considered that the value of each derivative should not be varied independently to grasp the sensitivity of manoeuvring performance to hydrodynamic derivatives precisely.

On the other hand, the hydrodynamic derivatives are generally derived by analyzing lateral force and yawing moment measured by conducting captive model tests in a model basin using a model ship. However, measurements of the hydrodynamic forces in same condition are not repeated in general, because it consumes long time to carry out the measurement even for one condition. Therefore, measurement error included in the measured results is directly reflected to the values of hydrodynamic derivatives. It means that simulated manoeuvring motion is also affected by the measurement error through the hydrodynamic derivatives. Then, it should be necessary to understand the influence of the measurement error on the hydrodynamic derivatives and simulation results to evaluate ship manoeuvrability properly.

3.2.1. Preparation of Pseudo Measurement Data of Lateral Force and Yawing Moment including Artificial Measurement Error

It is necessary to use accurate hydrodynamic derivatives presented in the cubic model and the quadratic model to simulate ship manoeuvring motion with high accuracy. The hydrodynamic derivatives are derived by fitting lateral force and yawing moment measured by conducting captive model tests in a model basin with the cubic polynomials or the quadratic polynomials shown in Eqs. (2.29) and (2.30). Therefore, it is important to obtain measured hydrodynamic forces having a good quality. Iterating measurements or taking average of measured values are one of the practical ways to reduce measurement error. However, measurements of the hydrodynamic forces in the same condition are rarely repeated in general because it requires a long time to carry out the measurement

even for one condition and there are many combinations of drift angle β and non-dimensional yaw rate r' to be considered to measure the hydrodynamic forces. Once measurement error occurs in the captive model tests, it is directly reflected to the values of the hydrodynamic derivatives. Therefore, grasping the influence of measurement error on the derived values of hydrodynamic derivatives is important.

The principal particulars of KVLCC2 is shown in Table 3.1. To evaluate the influence of measurement error on the hydrodynamic derivatives, pseudo measurement data for a model ship of KVLCC2 are prepared because it is impossible to obtain true hydrodynamic forces and difficult to extract precise errors from measured hydrodynamic forces. By adding the assumed measurement error to "provisional true data", pseudo measurement data can be created. "provisional true data" can be obtained by using hydrodynamic derivatives shown in Table 3.2 (Yasukawa and Yoshimura, 2015). Detail of the pseudo measurement error including artificial measurement error are described later.

As the true values of measured hydrodynamic forces, calculated lateral force and yawing moment using hydrodynamic derivatives presented in Table 3.2 (Yasukawa and Yoshimura, 2015) are used. Red lines shown in Fig. 3.1 represent non-dimensional lateral force Y'_H and yawing moment N'_H for non-dimensional yaw rate r' =0.0, 0.2, 0.4, 0.6, and 1.0 for the variation of drift angle β in the range of -4.0° and 20.0°. It should be noted that the effect of centrifugal force is contained in Y'_H and N'_H presented in Fig. 3.1. They are expressed as $-(m' + m'_x)r'$ for lateral force and $x'_G m' r'$ for yawing moment, respectively. x'_G stands for non-dimensional distance between the midship and the centre of gravity of a ship. Furthermore, circles presented in Fig. 3.1 are deemed as the true values of non-dimensional lateral force and yawing moment when the pseudo measurement data including artificial measurement error are created. Hereafter, the data is noted as "provisional true data."

Table 3.1 Principal particulars of KVLCC2

		Model	Full scale
L	(m)	2.902	320.0
B	(m)	0.527	58.0
d	(m)	0.189	20.8
C_b		0.810	0.810

Table 3.2 Hydrodynamic derivatives for cubic model

Y'_v	–0.315	N'_v	–0.137
Y'_{vvv}	–1.607	N'_{vvv}	–0.030
$Y'_r - (m' + m'_x)$	–0.233	$N'_r - x'_G m'$	–0.059
Y'_{rrr}	0.008	N'_{rrr}	–0.013
Y'_{vrr}	–0.391	N'_{vrr}	0.055
Y'_{vvr}	0.379	N'_{vvr}	–0.294

Table 3.3 Hydrodynamic derivatives for quadratic model

Y'_v	–0.235	N'_v	–0.135
Y'_{vv}	–0.761	N'_{vv}	–0.014
$Y'_r - (m' + m'_x)$	–0.235	$N'_r - x'_G m'$	–0.055
Y'_{rr}	0.009	N'_{rr}	–0.015
Y'_{vrr}	–0.391	N'_{vrr}	0.055
Y'_{vvr}	0.379	N'_{vvr}	–0.294

Before creating the pseudo measurement data, hydrodynamic derivatives for the quadratic model are derived by using the provisional true data. They are shown in Table 3.3 and calculated Y'_H and N'_H using the hydrodynamic derivatives are shown in Fig. 3.2. There is slight difference between the red lines and the blue lines. Reproducibility of the fitting curves based on the quadratic model is lower than that of the cubic model. The lower reproducibility might occur by having used the provisional true data generated by the cubic model.

It is expected to use the exact characteristics of real measurement error to prepare pseudo measurement data containing assumed measurement error. However, it is difficult to know the exact characteristics of real measurement error because there are so many sources of the measurement error such as resolution and inherent characteristics of measurement equipment, fluctuation of towing speed and angular velocity of a carriage,

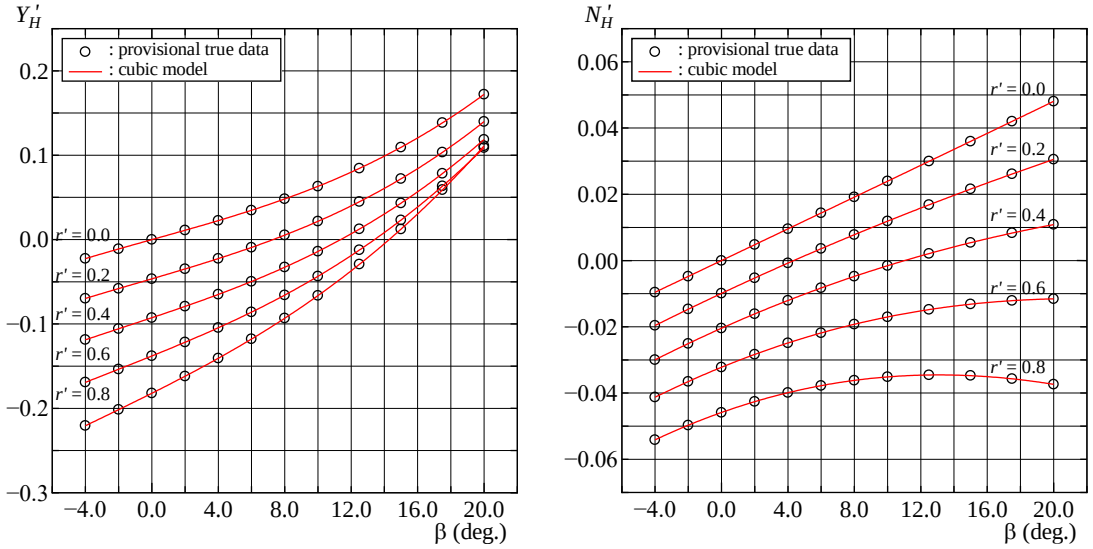

(a) Y'_H (b) N'_H

Figure 3.1 Substitute data for true non-dimensional lateral force Y'_H and yawing moment N'_H and their fitting lines based on cubic model

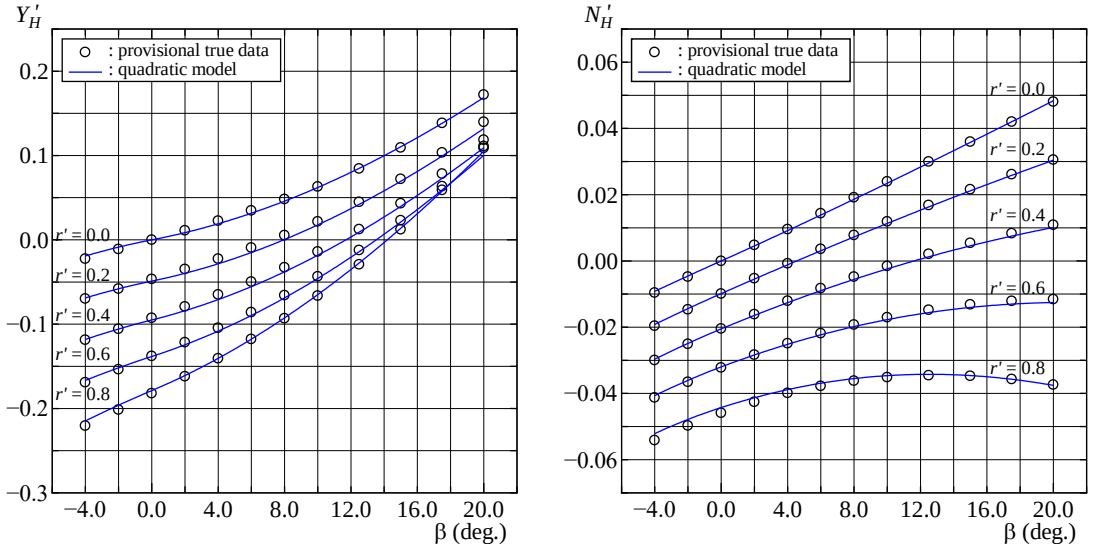

(a) Y'_H (b) N'_H

Figure 3.2 Substitute data for true non-dimensional lateral force Y'_H and yawing moment N'_H and their fitting lines based on quadratic model

setting error in drift angle, facility bias, and so on. Therefore, the measurement error is assumed to be normally distributed and its standard deviation is also assumed to be expressed by σ. Based on these assumptions, pseudo measurement data is represented as follows in Monte Carlo simulations which are described later.

$$F'_{\mathrm{pm}} = F'_{\mathrm{pt}} \pm 2n\sigma. \tag{3.1}$$

F'_{pm} and F'_{pt} represent the pseudo measurement data of hydrodynamic force and the provisional true data of hydrodynamic force, respectively. This calculation is carried out for each combination of drift angle β and non-dimensional yaw rate r' using a normal random number n chosen in the range of -1.0 and 1.0.

3.2.2. Monte Carlo Simulations for Evaluation of Influence of Measurement Error on Hydrodynamic Derivatives

Monte Carlo simulations are conducted to evaluate the influence of measurement error on hydrodynamic derivatives. Pseudo measurement data are created by using Eq. (3.1) for each simulation and 10^5 times of simulations are repeated to derive the values of hydrodynamic derivatives for the cubic model and the quadratic model. The value of standard deviation of the measurement error σ is assumed to be 0.5%, 1.0%, 1.5%, and 2.0% of the positive maximum value of the provisional true data shown in Fig. 3.1. Namely, the maximum value is selected as the value of Y'_H or N'_H at β = 20° and r' = 0.0.

Hydrodynamic derivatives of the cubic model and the quadratic model are derived using all pseudo measurement data created in the Monte Carlo simulations. Fig. 3.3 shows an example of the pseudo measurement data created based on Eq. (3.1) when the value of standard deviation σ is assumed to be 1.0% of the maximum value. It can be observed that the pseudo measurement data shown with green circles deviate from the provisional true data shown with black circles, but the difference between them are not so big. That is likely observed in actual captive model tests. Red and blue lines provide fitting curves obtained by using the hydrodynamic derivatives for the cubic model and the quadratic model derived from the pseudo measurement data shown with green circles.

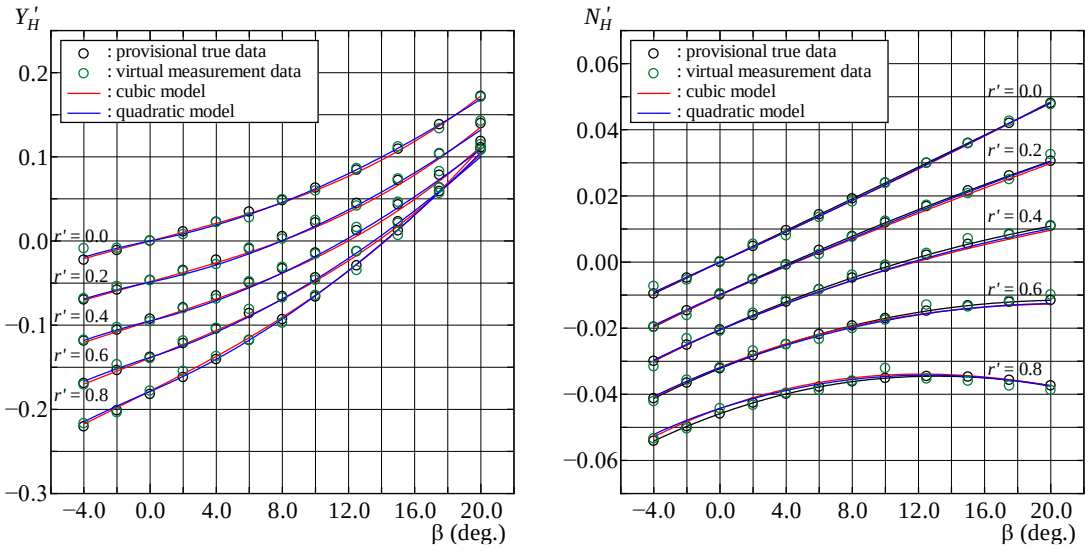

(a) Y_H' (b) N_H'

Figure 3.3 Example of artificial measurement data of Y_H' and N_H' and their fitting lines based on cubic model.

After the Monte Carlo simulations are completed, standard deviation for each hydrodynamic derivatives are calculated by this following formula,

$$D_{derivatives} = D_i'/D_{\mathrm{pt}}'. \tag{3.2}$$

D_i' stands for each hydrodynamic derivative derived by using the *i*-th pseudo measurement data and D_{pt}' represents each hydrodynamic derivative derived by using the provisional true data. The standard deviations for all kinds of hydrodynamic derivatives are presented in Table 3.4. It can be understood that the values of standard deviations for all kinds of hydrodynamic derivatives for the cubic model are smaller than those for the quadratic model. Therefore, it is expected that the cubic model is less susceptible to measurement error comparing with the quadratic model. It is also observed that the standard deviations of linear derivatives such as Y_v', $Y_r' - (m' + m_x')$, N_v', and $N_r' - x_G' m'$ are smaller than those of non-linear derivatives. This is because linear and non-linear derivatives related to the same parameter have close relation each other. Once a linear derivative deviate from the provisional true value, non-linear derivative which is subordinate to the linear derivative is much affected by variation of the linear derivative. It suggests that assuming uniform standard deviations for all hydrodynamic derivatives

which is often used to evaluate the sensitivity of ship manoeuvrability to each hydrodynamic derivative by conducting Monte Carlo simulations is not appropriate.

Table 3.4 Standard deviation for each hydrodynamic derivatives

	Cubic model	Quadratic model
$(Y'_v)_i/(Y'_v)_{\mathrm{pt}}$	0.041	0.091
$(Y'_{vvv})_i\ /(Y'_{vvv})_{\mathrm{pt}}$	0.097	–
$(Y'_{vv})_i/(Y'_{vv})_{\mathrm{pt}}$	–	0.101
$\frac{\{Y'_r-(m'+m'_x)\}_i}{\{Y'_r-(m'+m'_x)\}_{\mathrm{pt}}}$	0.035	0.055
$(Y'_{rrr})_i/(Y'_{rrr})_{\mathrm{pt}}$	2.019	–
$(Y'_{rr})_i/(Y'_{rr})_{\mathrm{pt}}$	–	2.042
$(Y'_{vrr})_i/(Y'_{vrr})_{\mathrm{pt}}$	0.129	0.191
$(Y'_{vvr})_i/(Y'_{vvr})_{\mathrm{pt}}$	0.325	0.444
$(N'_v)_i/(N'_v)_{\mathrm{pt}}$	0.027	0.044
$(N'_{vvv})_i/(N'_{vvv})_{\mathrm{pt}}$	1.440	–
$(N'_{vv})_i/(N'_{vv})_{\mathrm{pt}}$	–	1.510
$\frac{(N'_r-x'_Gm')_i}{(N'_r-x'_Gm')_{\mathrm{pt}}}$	0.039	0.066
$(N'_{rrr})_i/(N'_{rrr})_{\mathrm{pt}}$	0.346	–
$(N'_{rr})_i/(N'_{rr})_{\mathrm{pt}}$	–	0.349
$(N'_{vrr})_i/(N'_{vrr})_{\mathrm{pt}}$	0.254	0.377
$(N'_{vvr})_i/(N'_{vvr})_{\mathrm{pt}}$	0.117	0.159

3.3. Simulation of Ship Manoeuvring Motions Considering Influence of Measurement Error

3.3.1. Conditions of Simulations and Simulation Results without Measurement Error

Eqs. (2.29) and (2.30) can be simulated by the Runge-Kutta method. As for the values of parameters such as hydrodynamic derivatives for X'_H and interaction coefficients among ship hull, propeller, and rudder which are essential to obtain accurate simulation results, values shown in a reference (Yasukawa and Yoshimura, 2015) are used except for the

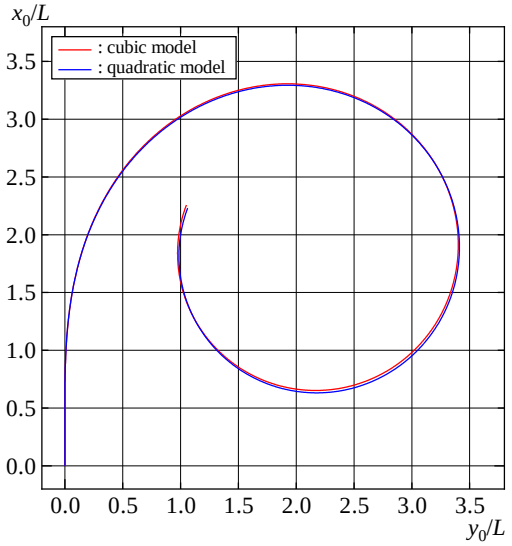

(a) Turning trajectories

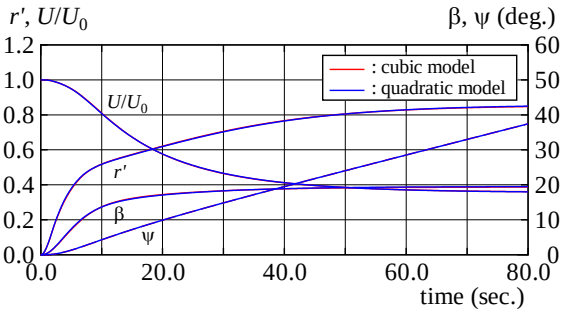

(b) Time histories of r', U/U_0, β, and ψ

Figure 3.4 Trajectories and time histories of r', U/U_0, β, and ψ in turning motion with rudder angle of 35°

Table 3.5 Values of evaluation indices for provisional true data

Evaluation indices	Cubic model	Quadratic model
Advance, $A_{D\mathrm{pt}}/L$	3.234	3.222
Transfer, $T_{R\mathrm{pt}}/L$	1.440	1.446
Tactical Dia., $D_{T\mathrm{pt}}/L$	3.331	3.341

hydrodynamic derivatives for Y'_H and N'_H presented in the previous section. Initial ship speed U_0 in the simulations is set as 0.73576 m/s which corresponds to 15 knots in full scale.

Fig. 3.4 shows turning trajectories with rudder angle of 35° and the time histories of non-dimensional yaw rate r', speed drop ratio U/U_0, drift angle β, and heading angle ψ simulated by using hydrodynamic derivatives based on the provisional true data. The values of advance A_D, transfer T_R, and tactical diameter D_T are shown in non-dimensional form in Table 3.5. There are hardly difference between the simulated results for the cubic model and the quadratic model.

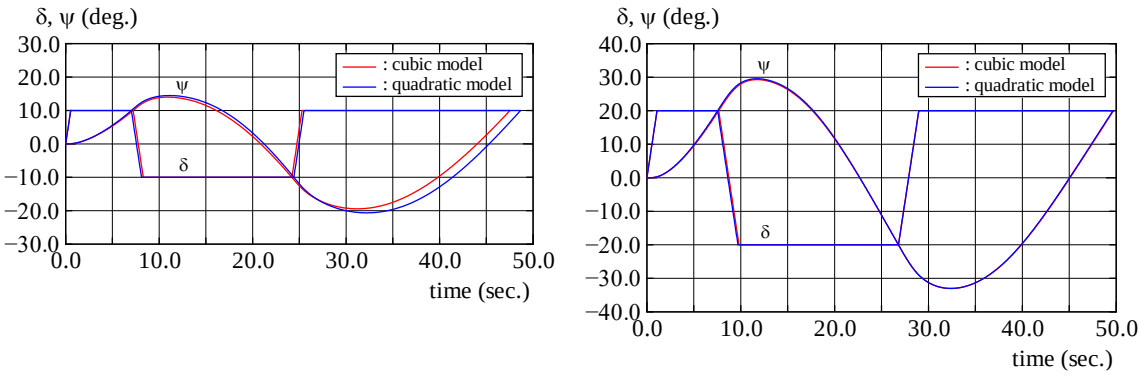

(a) 10°/10° zigzag (b) 20°/20° zigzag

Figure 3.5 Times histories of δ and ψ in 10°/10° and 20°/20° zigzag manoeuvres

Table 3.6 Values of evaluation indices for provisional true data

Evaluation indices	Cubic model	Quadratic model
1st overshoot angle of 10°/10° zigzag, $\psi_{1\mathrm{pt}}^{(10)}$	3.995°	4.476°
2nd overshoot angle of 10°/10° zigzag, $\psi_{2\mathrm{pt}}^{(10)}$	9.420°	10.637°
1st overshoot angle of 20°/20° zigzag, $\psi_{1\mathrm{pt}}^{(20)}$	9.277°	9.547°
2nd overshoot angle of 20°/20° zigzag, $\psi_{2\mathrm{pt}}^{(20)}$	13.021°	13.006°

Simulated time histories of rudder angle δ and heading angle ψ for 10°/10° and 20°/20° zigzag manoeuvres are shown in Fig. 3.5 and the values of overshoot angles are presented in Table 3.6. It is observed that the first and second overshoot angles of 10°/10° zigzag manoeuvre for the quadratic model are larger than those for the cubic model. It can be considered that the difference originates from lower reproducibility of the quadratic model as described in the previous section. Therefore, the authors only focus on the variation of evaluation indices such as advance, transfer, tactical diameter, and overshoot angles when hydrodynamic derivatives for Y_H' and N_H' derived by using the *i*-th pseudo measurement data are used.

3.3.2. Sensitivity of Simulated Manoeuvring Motion to Measurement Error

Simulations of turning motion with rudder angle of 35° and 10°/10° and 20°/20° zigzag manoeuvres are conducted using 10^5 sets of hydrodynamic derivatives for Y_H' and N_H' created by the Monte Carlo simulations considering the effect of the pseudo measurement

error. Advance A_D, transfer T_R, and tactical diameter D_T are selected as evaluation indices to investigate the sensitivity of ship turning motion to hydrodynamic derivatives. On the other hand, $\psi_1^{(10)}$ and $\psi_2^{(10)}$ which are the first and the second overshoot angles of 10°/10° zigzag and $\psi_1^{(20)}$ and $\psi_2^{(20)}$ for 20°/20° zigzag are used as evaluation indices to observe the sensitivity of zigzag manoeuvres.

Fig. 3.6 shows normalized histograms of $I_i - I_{\mathrm{pt}}$ for turning motion when the value of standard deviation σ used in Eq. (3.1) is assumed to be 1.0% of the maximum value. Here, I_i stands for an evaluation index obtained by using hydrodynamic derivatives for Y'_H and N'_H based on the *i*-th pseudo measurement data in the Monte Carlo simulations. I_{pt} is an evaluation index for the provisional true data which is presented in Table 3.5. Therefore, $I_i - I_{\mathrm{pt}}$ represents the variation of each evaluation index. Vertical axes indicate normalized frequencies of the variation. Furthermore, the mean value μ and the standard deviation σ of each evaluate index I_i are shown in Table 3.7.

It is observed that the quadratic model tends to have a larger standard deviation comparing with that of the cubic model. This tendency is consistent with the larger variation of hydrodynamic derivatives caused by the pseudo measurement error as shown in Table 3.4. It suggests that further quality control of measurement in captive model tests is required when the quadratic model is adopted to express lateral force and yawing moment acting on a ship hull. It is also observed that the variation range of $T_{Ri} - T_{R\mathrm{pt}}$ is the narrowest among three evaluation indices both for the cubic model and the quadratic model as presented in Table 3.7. The impact of measurement error for simulated values of advance is approximately equivalent to that of tactical diameter.

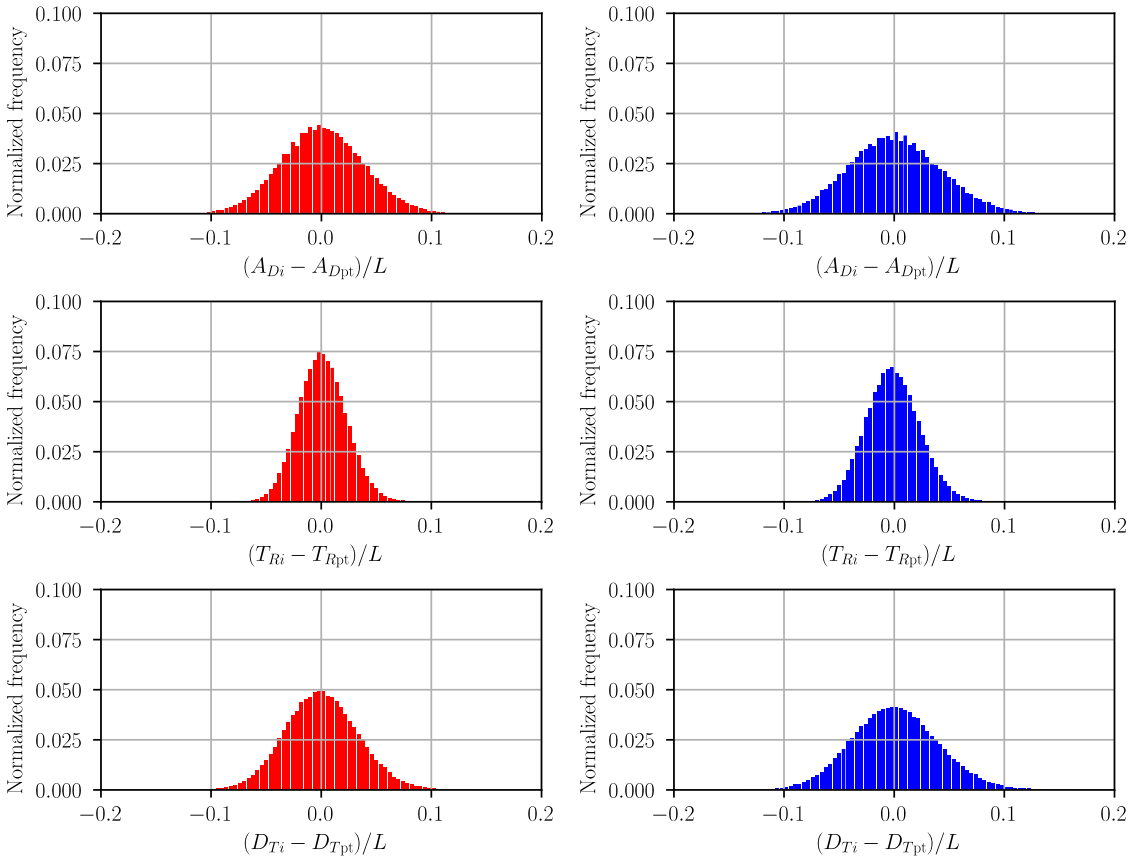

(a) Cubic model (b) Quadratic model

Figure 3.6 Normalized histograms for each evaluation index for turning motion

Table 3.7 Mean value and standard deviation for each evaluation index for turning motion

Evaluation indices	Cubic model		Quadratic model	
	μ	σ	μ	σ
A_{Di}/L	3.235	0.037	3.223	0.042
T_{Ri}/L	1.442	0.022	1.445	0.024
D_{Ti}/L	3.332	0.033	3.342	0.039

Examples of simulation results picked up from the 10^5 times of simulations are shown in Fig. 3.7. Trajectory and time histories drawn by red solid lines are same as the trajectory and the time histories for the cubic model presented in Fig. 3.4. Additional two kinds of lines (dotted line and broken line) indicate the simulation results of which the values of advance A_D are nearly equal to $\mu + 2\sigma$ or $\mu - 2\sigma$, respectively. It can be considered that most of simulation results exist between these two lines. Hydrodynamic derivatives used

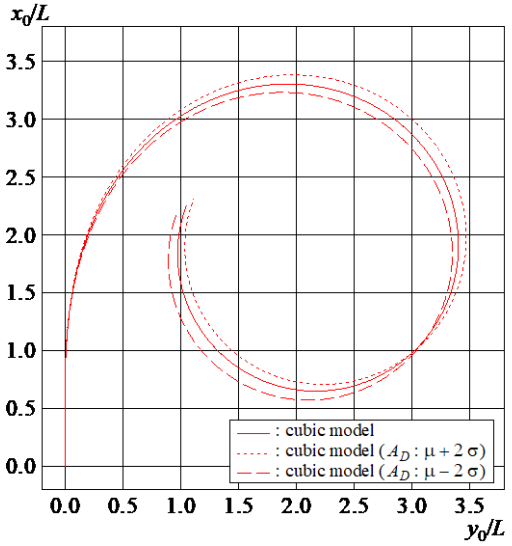

(a) Turning trajectories

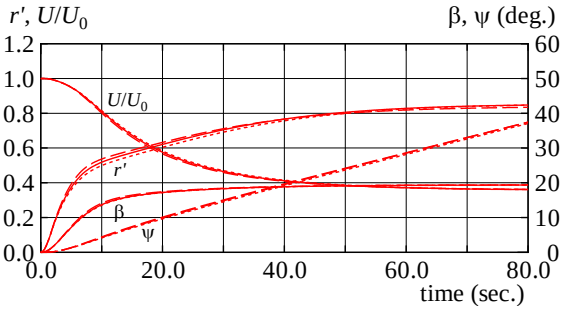

(b) Time histories of r', U/U_0, β, and ψ

Figure 3.7 Trajectories and time histories of r', U/U_0, β, and ψ in turning motion with rudder angle of 35°

Table 3.8 Hydrodynamic derivatives of cubic model

	Original	A_D : μ + 2σ	A_D : μ − 2σ
Y'_v	−0.315	−0.312	−0.305
Y'_{vvv}	−1.607	−1.680	−1.739
$Y'_r - (m' + m'_x)$	−0.233	−0.234	−0.238
Y'_{rrr}	0.008	0.008	0.012
Y'_{vrr}	−0.391	−0.439	−0.387
Y'_{vvr}	0.379	0.247	0.381
N'_v	−0.137	−0.127	−0.143
N'_{vvv}	−0.030	−0.147	0.027
$N'_r - x'_G m'$	−0.059	−0.060	−0.056
N'_{rrr}	−0.013	−0.012	−0.016
N'_{vrr}	0.055	0.021	0.093
N'_{vvr}	−0.294	−0.387	−0.230

in these simulations are presented in Table 3.8. When the three kinds of values for each hydrodynamic derivative are compared, difference among them is not so big, though obviously different simulation results are obtained.

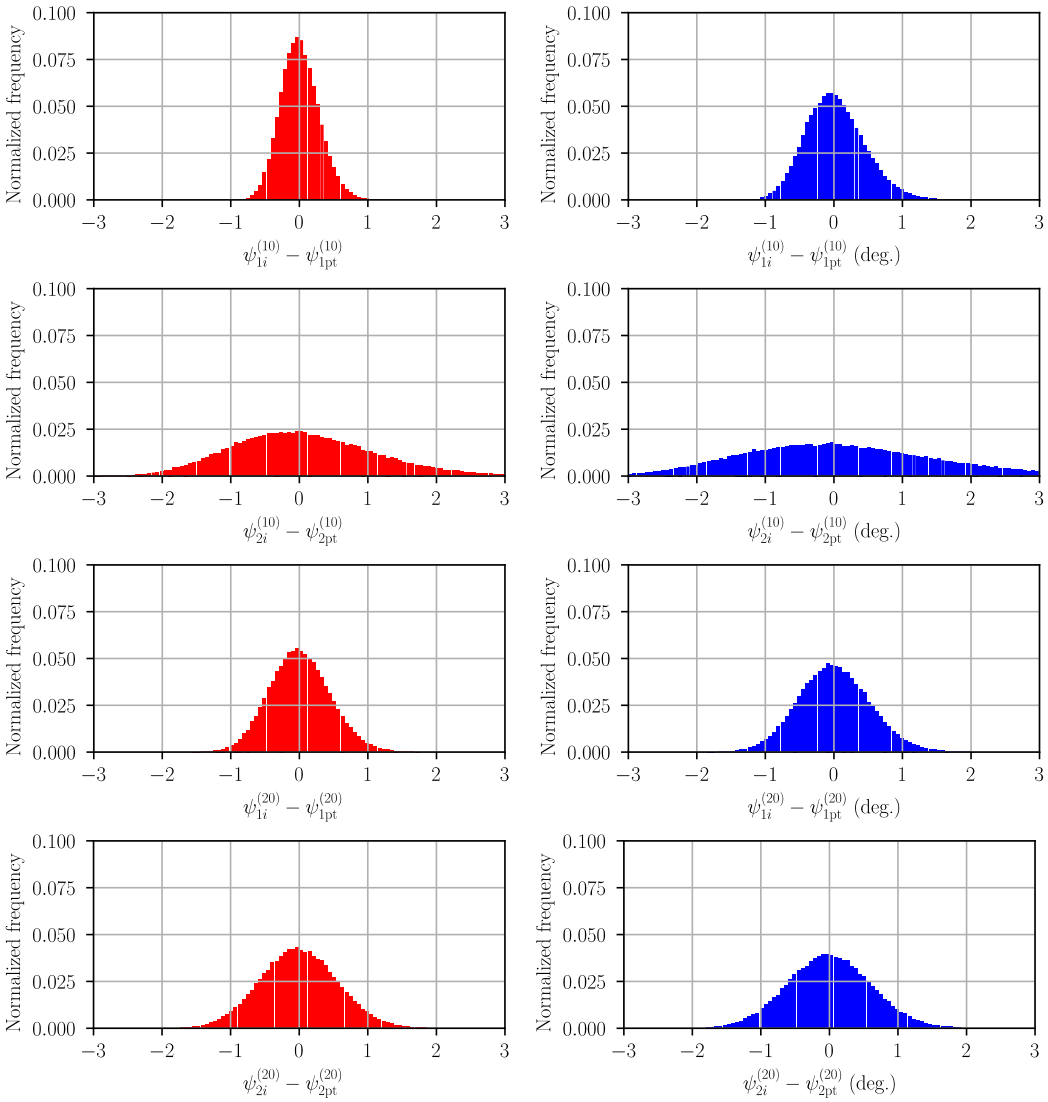

(a) Cubic model (b) Quadratic model

Figure 3.8 Normalized histograms for each evaluation index for turning motion

Normalized histograms of the variation of each evaluation index $I_i - I_{\mathrm{pt}}$ for 10°/10° and 20°/20° zigzag manoeuvres are shown in Fig. 3.8 and the mean value μ and the standard deviation σ of each evaluate index are presented in Table 3.9. As same as the comparison between the characteristics of the cubic model and the quadratic model in turning motion, the quadratic model tends to have a larger standard deviation. It is obvious that the

Table 3.9 Mean value and standard deviation for each evaluation index for 10°/10° and 20°/20° zigzag manoeuvres

Evaluation Indices	Cubic model		Quadratic model	
	μ	σ	μ	σ
$\psi_{1i}^{(10)}$	4.005	0.281	4.499	0.432
$\psi_{2i}^{(10)}$	9.488	1.054	10.754	1.465
$\psi_{1i}^{(20)}$	9.284	0.440	9.556	0.518
$\psi_{2i}^{(20)}$	13.015	0.563	13.006	0.610

distribution range of $\psi_{2i}^{(10)} - \psi_{2\mathrm{pt}}^{(10)}$ is the widest among all overshoot angles. It means the second overshoot angle of 10°/10° zigzag is considerably affected by the measurement error. It can be confirmed by the standard deviation presented in Table 3.9.

Examples of simulation results picked up from the 10^5 times of simulations are shown in Fig. 3.9. Time histories of δ and ψ drawn by red solid lines are same as the lines for the cubic model presented in Fig. 3.5. Additional two kinds of lines indicate simulation results of which the value of $\psi_1^{(10)}$ or $\psi_1^{(20)}$ is nearly equal to $\mu + 2\sigma$ or $\mu - 2\sigma$. According to Fig. 3.9 (a), it is confirmed that the variation of the first overshoot angle causes considerable variation of the second overshoot angle in 10°/10° zigzag manoeuvre. Therefore, it can be concluded that measurement error included in measured hydrodynamic forces have much influence on transient motion which is observed in 10°/10° zigzag manoeuvre.

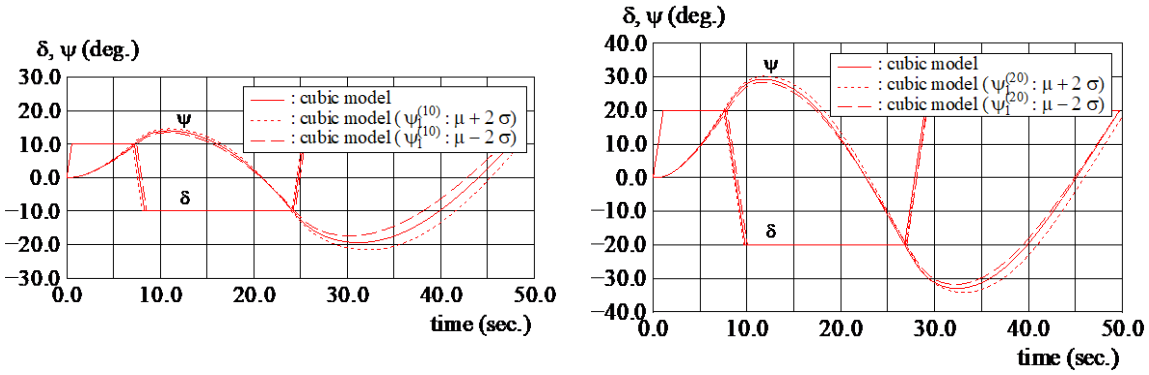

(a) 10°/10° zigzag (b) 20°/20° zigzag

Figure 3.9 Times histories of δ and ψ in 10°/10° and 20°/20° zigzag manoeuvres

3.3.3. Effect of Standard Deviation of Measurement Error

Finally, effect of the assumed standard deviation of measurement error on simulation results of manoeuvring motions are investigated using the cubic model. Table 3.10 shows the variation of standard deviation for each evaluation index for turning motion and 10°/10° and 20°/20° zigzag manoeuvres when the standard deviation of the pseudo measurement error is changed as 0.5%, 1.0%, 1.5%, and 2.0% of the maximum values described in the previous section. According to Table 3.10, the standard deviation for each evaluation index is proportional to the assumed standard deviation of the pseudo measurement error. Therefore, it can be concluded that 10°/10° zigzag manoeuvre is the most sensitive to the measurement error included in hydrodynamic forces measured by conducting captive model tests, though the degree of influence should be investigated further considering realistic measurement error.

Table 3.10 Variation of standard deviation for each evaluation index for turning motion and 10°/10° and 20°/20° zigzag manoeuvres by difference of pseudo measurement error

	0.5%	1.0%	1.5%	2.0%
A_{Di}/L	0.019	0.037	0.056	0.075
T_{Ri}/L	0.011	0.022	0.032	0.043
D_{Ti}/L	0.016	0.033	0.049	0.066
$\psi_{1i}^{(10)}$	0.140	0.281	0.426	0.576
$\psi_{2i}^{(10)}$	0.521	1.054	1.610	2.202
$\psi_{1i}^{(20)}$	0.220	0.440	0.661	0.884
$\psi_{2i}^{(20)}$	0.282	0.563	0.843	1.120

3.4. Conclusion

Sensitivity of simulated manoeuvring motion to hydrodynamic derivatives derived from measured lateral force and yawing moment including measurement error was investigated and the following conclusions were obtained.

- It is expected that the cubic model is less susceptible to measurement error comparing with the quadratic model.
- Assuming uniform standard deviations for all hydrodynamic derivatives is not appropriate for the Monte Carlo simulations method because the standard deviations of non-linear derivatives are larger than those of linear derivatives.
- Manoeuvring indices such as advance, tactical diameter, and overshoot angles predicted by using hydrodynamic derivatives based on the quadratic model tends to have a larger standard deviation comparing with those based on the cubic model.
- Measurement error included in measured hydrodynamic forces have much influence on transient motion of a ship such as 10°/10° zigzag manoeuvre.
- The standard deviation for each evaluation index is proportional to the assumed standard deviation of the pseudo measurement error.

Though influence of hydrodynamic derivatives for Y'_H and N'_H on simulated manoeuvring motion was only investigated, there are many parameters which have significant impact on ship manoeuvrability. They should be further investigated considering realistic measurement error.

Chapter 4 Source and Quasi Vortex Lattice Method (SQCM)

4.1. Introduction

The sensitivity of simulated ship manoeuvring motion using hydrodynamic derivatives to measurement error included in measured lateral force and yawing moment has been investigated in the previous chapter. In order to simulate manoeuvring motion precisely, conducting captive model tests is necessary paying much attention to the accuracy of measurement. However, captive model tests are time and cost consuming and the number of facilities where captive model tests can be conducted is limited. It becomes general problem with these model tests. Hence, development of practical calculation methods for hydrodynamic forces acting on a ship hull is expected.

In this chapter, a calculation method to predict lateral force and yawing moment acting on a ship hull representing the shape of the hull accurately is introduced. This calculation method is based on the SQCM (Source and Quasi Continuous vortex lattice Method) which is one of the panel methods as explained in Chapter 1. It has been confirmed that the SQCM had good accuracy to calculate hydrodynamic force produced by a propeller.

Generally, the SQCM is based on two methods proposed by Hess and Smith (1964) and Lan (1970), respectively. The Hess and Smith method is used to represent the shape of the body expressed by several panels and sources are distributed for each panel. Then, Lan (1970) represented circulation around the body by discrete vortices arranged along the central longitudinal plane of the body.

The SQCM is applied to predict hydrodynamic forces acting on a ship hull in drift motion. In this method, ship hull is treated as a thick wing. To represent the flow field around the hull appropriately, vortex models considering deformation of free vortices are introduced. Then, two kinds of vortex models are examined to improve the estimation accuracy of lateral force and yawing moment in the range of large drift angle.

4.2. Basic Theory of SQCM

Fig. 4.1 shows the schematic view of the SQCM. For simplicity, a target object is represented by two-dimensional body. In the SQCM, the shape of the body is expressed by several panels based on the Hess and Smith method (1964) and sources are distributed

for each panel. Furthermore, according to Lan (1970), circulation around the body is expressed by vortices arranged along the central longitudinal plane of the body. Hydrodynamic forces acting on a body in uniform flow can be estimated by locating calculation points on the surface of each panel and the vortex points as shown by blue cross marks in Fig. 4.1 and by calculating the strength of the sources and the vortices that satisfy boundary conditions at the calculation points. Like the QCM method, the Kutta condition is automatically satisfied as the strength of the vortices become zero at the trailing edge of the wing-shaped body. Since there is no need to perform repetitive calculation, the SQCM is an efficient calculation method with respect to calculation time.

Consequently, total flow velocity around the body in uniform flow is expressed as follows,

$$\vec{V} = \overrightarrow{V_0} + \overrightarrow{V_s} + \overrightarrow{V_v}, \tag{4.1}$$

where,

$\vec{V}$: total flow velocity vector,

$\overrightarrow{V_0}$: flow velocity vector by uniform flow around the body,

$\overrightarrow{V_s}$: induced velocity vector by source panels,

$\overrightarrow{V_v}$: induced velocity vector by vortices.

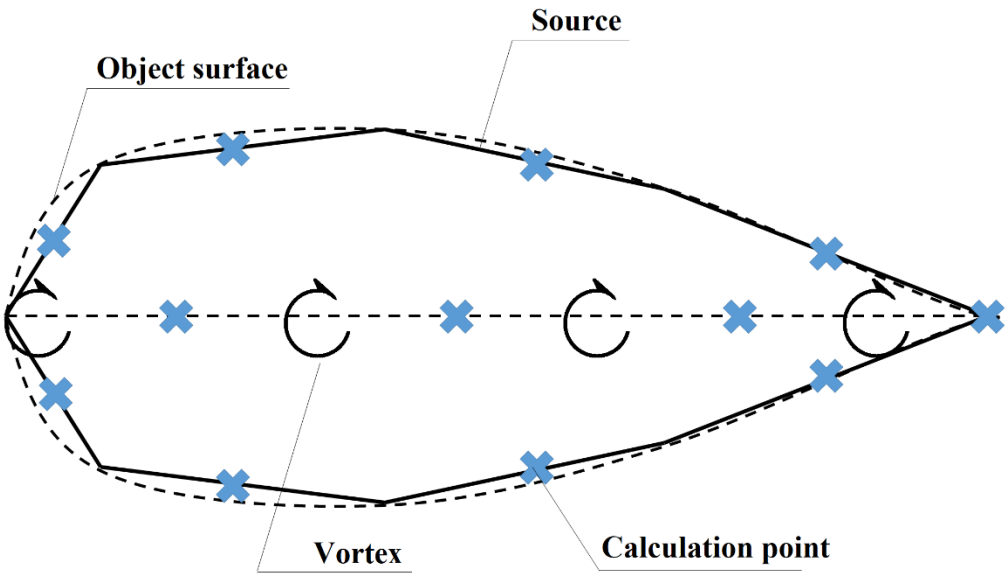

Figure 4.1 Schematic diagram of SQCM

4.3. Calculation Method of Induced Velocity by Sources

4.3.1. Hess and Smith Method

Assuming a double body model of a body in uniform flow, the origin of the basic coordinate system $o-xyz$ is defined as shown in Fig. 4.2. Body surface is represented by discrete points which are placed on its surface. These are identified as a group of four to form the quadrilateral surface element which is treated as a source panel. To form the quadrilateral surface element from a four given point, two diagonal vectors, each of which is simply the vector between the two of the four points are formed. Here, $\vec{n}$ is a cross product of the two diagonal vectors, taken as the normal vector to the quadrilateral surface element. The four points which are projected parallel to the normal vector into the plane of the element to obtain the points at the corners of the quadrilateral. The element plane as defined here is equidistant from the four points used to form the element.

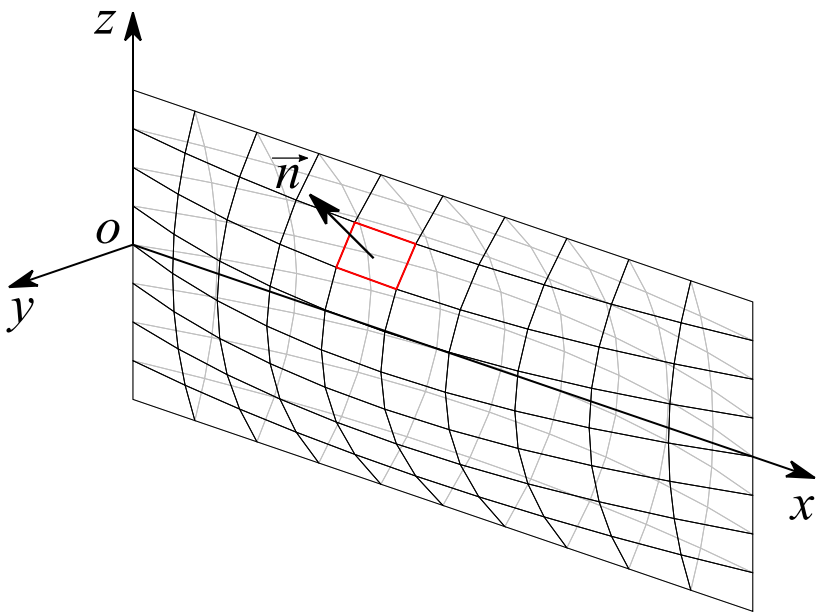

Figure 4.2 Representation of body shape and basic coordinate system.

The basic formula of the Hess and Smith method gives induced velocity by a quadrilateral source panels with a unit source density at a point in the space. Let the surface of the body have an equation of the form,

$$F(x, y, z) = 0, \tag{4.2}$$

where, x, y, and z are the coordinates in the basic coordinate system. The undisturbed flow coming to the body is taken as uniform flow of unit magnitude. This flow is described by the following equation,

$$V_\infty = \left(V_{\infty x}^2 + V_{\infty y}^2 + V_{\infty z}^2\right)^{1/2} = 1. \tag{4.3}$$

The fluid velocity at an arbitrary point may be denoted as the negative gradient of a velocity potential function ϕ, which must satisfy the following three conditions; it must satisfy Laplace's equation, it should have a zero normal derivative on the surface body, and it should reach the proper uniform flow potential at infinity, as follows,

$$\Delta\phi = 0 \quad \text{in} \quad R, \tag{4.4}$$

$$\frac{\partial\phi}{\partial n} \equiv \vec{n} \cdot \text{grad}\phi|_{F=0} = 0, \tag{4.5}$$

$$\phi \to -\left(xV_{\infty x} + yV_{\infty y} + zV_{\infty z}\right) \quad \text{for} \quad (x^2 + y^2 + z^2)^{1/2} \to \infty. \tag{4.6}$$

Here, Δ stands for the Laplacian operator and $\vec{n}$ is the unit normal vector at an arbitrary point of the body surface. For convenience, ϕ can be written as:

$$\phi = \varphi_\infty + \varphi, \tag{4.7}$$

where φ_∞ is the uniform flow potential and φ is the disturbance potential due to the body. φ will be denoted as the potential of source density distribution over the surface S of the body. The potential at arbitrary point $P(x, y, z)$ in the basic coordinate system due to a unit point source located at a point q on the body surface is $1 / r(P, q)$, where, $r(P, q)$ is the distance between the points P and q. Accordingly, the potential φ at P due to a source density distribution $\sigma(q)$ on the surface of the body is given by,

$$\varphi_{(x,y,z)} = \oiint_S \frac{\sigma(q)}{r(P,q)} dS. \tag{4.8}$$

4.3.2. Basic Coordinate System to Panel Fixed Coordinate System Conversion Method

Fig. 4.3 shows the panel fixed coordinate system $O - \xi\eta\zeta$. ζ axis is set in the direction of the outward normal vector $\vec{n}$ on the quadrilateral surface. In addition, one point is selected where the fluid velocity normal to the quadrilateral surface is required to vanish and where tangential velocity and pressure are eventually evaluated. The origin O of the panel fixed coordinate system is designated as a null point which is a point that does not receive the induced velocity by the panel itself.

The conversion sequence from the basic coordinate system $O - xyz$ to the panel fixed coordinate system $O - \xi\eta\zeta$ is performed in the procedure from (a) to (c) as shown in Fig. 4.4. The coordinate system $O_3 - x_3y_3z_3$ in (c) is the same as the panel fixed coordinate system $O - \xi\eta\zeta$. The details of how to obtain the transformation matrix $\boldsymbol{M}$ for performing this transformation will be described.

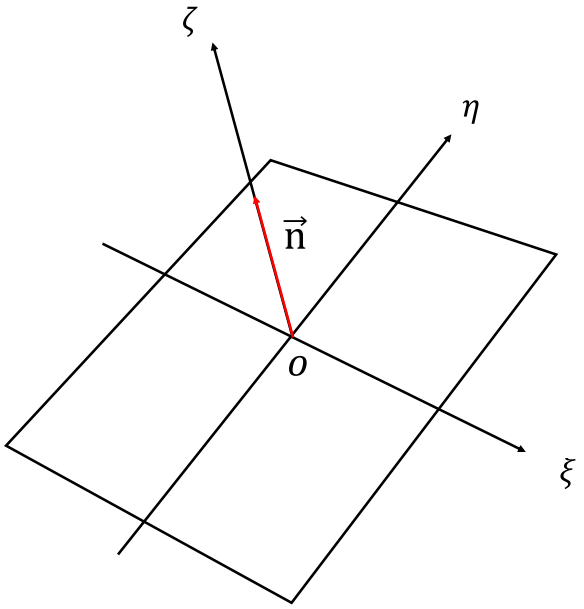

Figure 4.3 panel fixed coordinate system

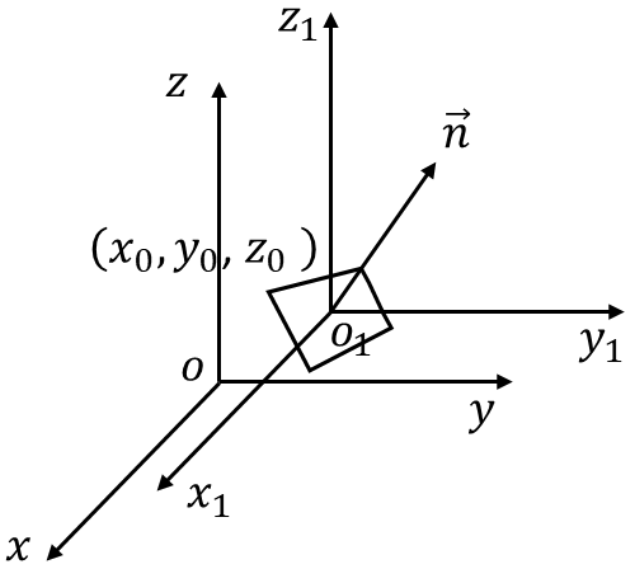

Figure 4.4 Conversion of flow coordinate – translation of the origin

First, in Fig. 4.4, let the coordinate (x_0, y_0, z_0) in the basic coordinate system $O - xyz$ be the origin of a coordinate system $O_1 - x_1y_1z_1$. In here, (x_0, y_0, z_0) is the average value of the coordinates of the four vertices of the panel. At this time, the coordinate of an arbitrary point (x, y, z) defined in the basic coordinate system is expressed as (x_1, y_1, z_1) in the $O_1 - x_1y_1z_1$ by using the following equations,

$$\begin{pmatrix} x_1 \\ y_1 \\ z_1 \end{pmatrix} = \begin{pmatrix} x \\ y \\ z \end{pmatrix} - \begin{pmatrix} x_0 \\ y_0 \\ z_0 \end{pmatrix} = \begin{pmatrix} x - x_0 \\ y - y_0 \\ z - z_0 \end{pmatrix}. \tag{4.9}$$

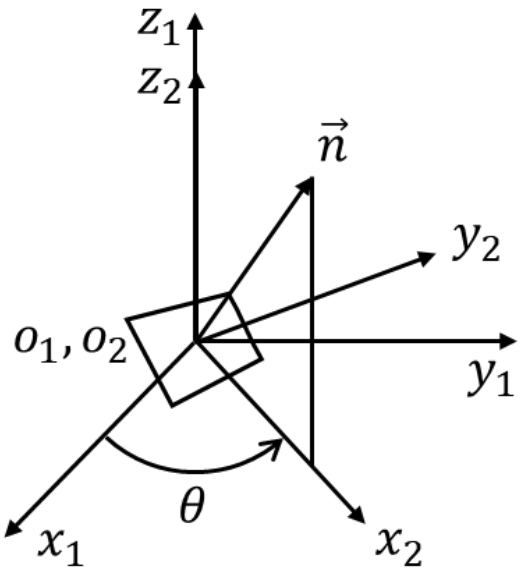

Figure 4.5 Conversion of flow coordinate – Rotation around z_1 axis

Next, as shown in Fig. 4.5, let θ be the angle between the straight line projected from the normal vector $\vec{n}$ onto the x_1y_1 plane and the x_1 axis. Then, let $O_1 - x_1y_1z_1$ to be rotated counterclockwise by the angle θ around z_1 axis. In here, the rotated coordinate system will be deemed as $O_2 - x_2y_2z_2$. At this time, the coordinate of an arbitrary point (x_1, y_1, z_1) defined in the $O_1 - x_1y_1z_1$ is expressed as (x_2, y_2, z_2) in the $O_2 - x_2y_2z_2$ by using the following equations.

$$\begin{pmatrix} x_2 \\ y_2 \\ z_2 \end{pmatrix} = \begin{pmatrix} \cos\theta & \sin\theta & 0 \\ -\sin\theta & \cos\theta & 0 \\ 0 & 0 & 1 \end{pmatrix} \begin{pmatrix} x_1 \\ y_1 \\ z_1 \end{pmatrix}. \tag{4.10}$$

Here, $\cos\theta$ and $\sin\theta$ are given by the following equations.

$$\cos\theta = \frac{n_x}{\sqrt{n_x^2 + n_y^2}}, \quad \sin\theta = \frac{n_y}{\sqrt{n_x^2 + n_y^2}}. \tag{4.11}$$

However, if $\cos\theta$ and $\sin\theta$ matches the direction normal vector $\vec{n}$ of the z_1 axis, the calculation of $1/\sqrt{n_x^2 + n_y^2}$ will be diverges, so the following values are given.

$$\cos\theta = 1, \quad \sin\theta = 0. \tag{4.12}$$

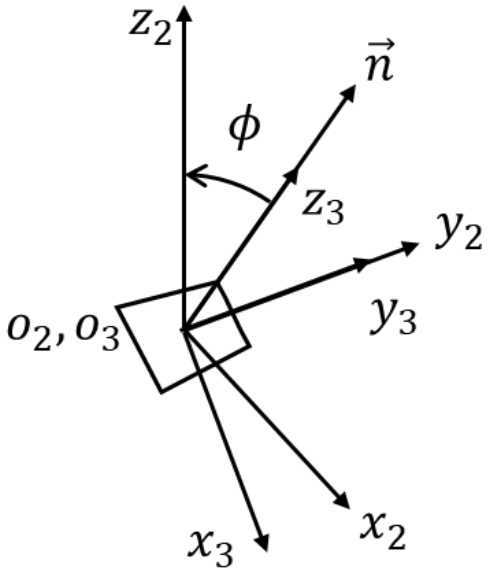

Figure 4.6 Conversion of flow coordinate – Rotation around z_2 axis

Furthermore, ϕ is the angle formed by the normal vector $\vec{n}$ and z_2 axis as shown in Fig. 4.6. Let $O_2 - x_2y_2z_2$ to be rotated clockwise by the angle ϕ. Here, the rotated coordinate system will be deemed as $O_3 - x_3y_3z_3$. At this time, the coordinate of an arbitrary point (x_2, y_2, z_2) defined in the $O_2 - x_2y_2z_2$ is expressed as (x_3, y_3, z_3) in the $O_3 - x_3y_3z_3$ by using the following equations.

$$\begin{pmatrix} x_3 \\ y_3 \\ z_3 \end{pmatrix} = \begin{pmatrix} \cos\phi & 0 & -\sin\phi \\ 0 & 1 & 0 \\ \sin\phi & 0 & \cos\phi \end{pmatrix} \begin{pmatrix} x_2 \\ y_2 \\ z_2 \end{pmatrix}. \tag{4.13}$$

Here, $\cos\phi$ and $\sin\phi$ are given by the following equations.

$$\cos\phi = n_z, \quad \sin\phi = \sqrt{n_x^2 + n_y^2}. \tag{4.14}$$

From the above, z_3 axis of the $O_3 - x_3y_3z_3$ is in the same direction with normal vector $\vec{n}$ of the object panel, which is same as the panel fixed coordinate system $O - \xi\eta\zeta$. The coordinate transformation from the basic coordinate system $O - xyz$ to the panel fixed coordinate system $O - \xi\eta\zeta$ is summarized as follows.

$$\begin{aligned}
\begin{pmatrix}\xi\\ \eta\\ \zeta\end{pmatrix} &= \begin{pmatrix}x_3\\ y_3\\ z_3\end{pmatrix} = \begin{pmatrix}\cos\phi & 0 & -\sin\phi\\ 0 & 1 & 0\\ \sin\phi & 0 & \cos\phi\end{pmatrix}\begin{pmatrix}x_2\\ y_2\\ z_2\end{pmatrix}\\
&= \begin{pmatrix}\cos\phi & 0 & -\sin\phi\\ 0 & 1 & 0\\ \sin\phi & 0 & \cos\phi\end{pmatrix}\begin{pmatrix}\cos\theta & \sin\theta & 0\\ -\sin\theta & \cos\theta & 0\\ 0 & 0 & 1\end{pmatrix}\begin{pmatrix}x_1\\ y_1\\ z_1\end{pmatrix}\\
&= \begin{pmatrix}\cos\phi\cos\theta & \cos\phi\sin\theta & -\sin\phi\\ -\sin\theta & \cos\theta & 0\\ \sin\phi\cos\theta & \sin\phi\sin\theta & \cos\phi\end{pmatrix}\begin{pmatrix}x - x_0\\ y - y_0\\ z - z_0\end{pmatrix}\\
&= \boldsymbol{M}\begin{pmatrix}x - x_0\\ y - y_0\\ z - z_0\end{pmatrix},
\end{aligned} \tag{4.15}$$

where,

$$\boldsymbol{M} = \begin{pmatrix}\cos\phi\cos\theta & \cos\phi\sin\theta & -\sin\phi\\ -\sin\theta & \cos\theta & 0\\ \sin\phi\cos\theta & \sin\phi\sin\theta & \cos\phi\end{pmatrix}. \tag{4.16}$$

On the other hand, since the hydrodynamic forces acting on the body is handled in the basic coordinate system, it is crucial to convert the induced velocity in the panel fixed coordinate system to the basic coordinate system. For that purpose, matrix $\boldsymbol{M^{-1}}$ is created to transform the panel fixed coordinate system $O - \xi\eta\zeta$ to the basic coordinate system $O - xyz$. The transformation matrix $\boldsymbol{M^{-1}}$ is given by this following equation.

$$\begin{pmatrix}x\\ y\\ z\end{pmatrix} = \boldsymbol{M^{-1}}\begin{pmatrix}\xi\\ \eta\\ \zeta\end{pmatrix} + \begin{pmatrix}x_0\\ y_0\\ z_0\end{pmatrix}. \tag{4.17}$$

4.3.3. Induced Velocity by Source of Quadrilateral Plane

Let $(\xi_k, \eta_k, 0)(k = 1, 2, 3, 4)$ be represented as the coordinates of the points at the corners of the quadrilateral in the panel fixed coordinate system as shown in Fig. 4.7. Further, the point at the corners of the quadrilateral are set to clockwise direction as seen from the angle of the unit normal vector to the plane of the quadrilateral. The velocity potential φ at the point $P(x, y, z)$ by the quadrilateral is given by the following equation,

$$\varphi = \iint_A \frac{dA}{r} = \iint_A \frac{d\xi d\eta}{[(x-\xi)^2 + (y-\eta)^2 + z^2]^{1/2}}, \tag{4.18}$$

where, r is the distance between the point $P(x, y, z)$ and the point $(\xi, \eta, 0)$ on the quadrilateral surface, and the range of integration is the area A of the quadrilateral surface. Therefore, if the velocity vector induced at the point P in the panel fixed coordinate system is $\overrightarrow{V_{sl}}(V_{sl_x}, V_{sl_y} V_{sl_z})$ then the components of the velocity vector are given by,

$$\left.\begin{aligned} V_{sl_x} &= -\frac{\partial \varphi}{\partial x} = \iint_A \frac{(x-\xi) d\xi d\eta}{r^3}, \\ V_{sl_y} &= -\frac{\partial \varphi}{\partial y} = \iint_A \frac{(y-\eta) d\xi d\eta}{r^3}, \\ V_{sl_z} &= -\frac{\partial \varphi}{\partial z} = \iint_A \frac{z d\xi d\eta}{r^3}. \end{aligned}\right\} \tag{4.19}$$

The potential function for the inside and the outside of the quadrilateral source panel shown in Fig. 4.7 is composed as the sum of the potentials of two semi-infinite source strips, each of whose boundaries consists of the side of the quadrilateral and two semi-infinite lines parallel to the one of the coordinate axes. The region corresponding to the inside of the quadrilateral has a value of source density $\sigma = +1/2$, and for the outside $\sigma = -1/2$. From Figs. 4.7 and 4.8, the source densities on the strips are canceled outside of the quadrilateral and added inside to give a unit value. Thus, the potential and velocity of the quadrilateral are given as the sum of the potentials and velocities of the four sets of semi-infinite strips.

Now, assuming that the induced velocity component on the y-axis direction at the point P due to the pair of semi-infinite strips corresponding to the points (ξ_k, η_k) and

(ξ_{k+1}, η_{k+1}) is $V_{sl_{y\,k,k+1}}(k = 1, \cdots, 4; \xi_5 = \xi_1, \eta_5 = \eta_1)$, it is given by the following equation,

$$V_{sl_{xk,k+1}} = \frac{1}{2}\int_{\xi k}^{\xi k+1} d\xi \left[\int_{-\infty}^{\eta k,k+1} - \int_{\eta k,k+1}^{\infty}\right] \frac{(y-\eta)d\eta}{[(x-\xi)^2 + (y-\eta)^2 + z^2]^{3/2}}, \tag{4.20}$$

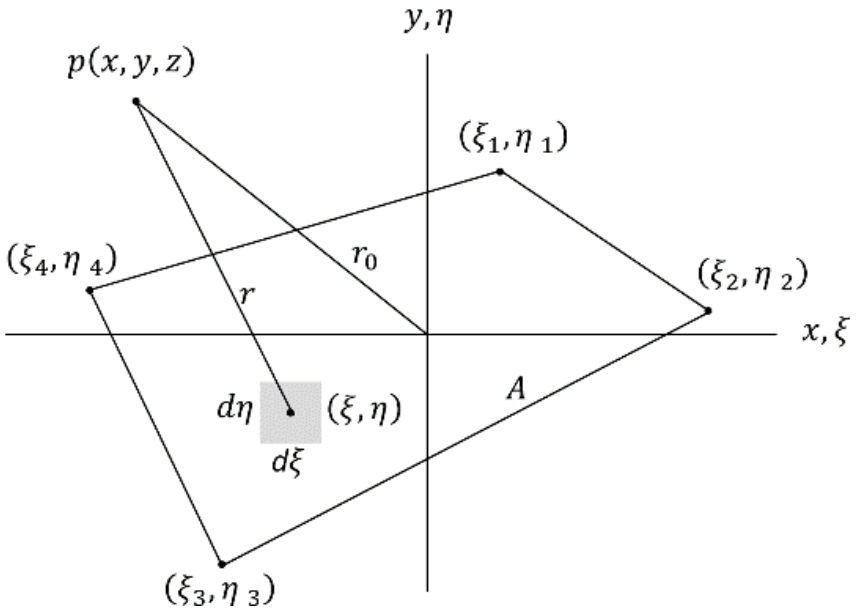

Figure 4.7 Source panel on xy plane

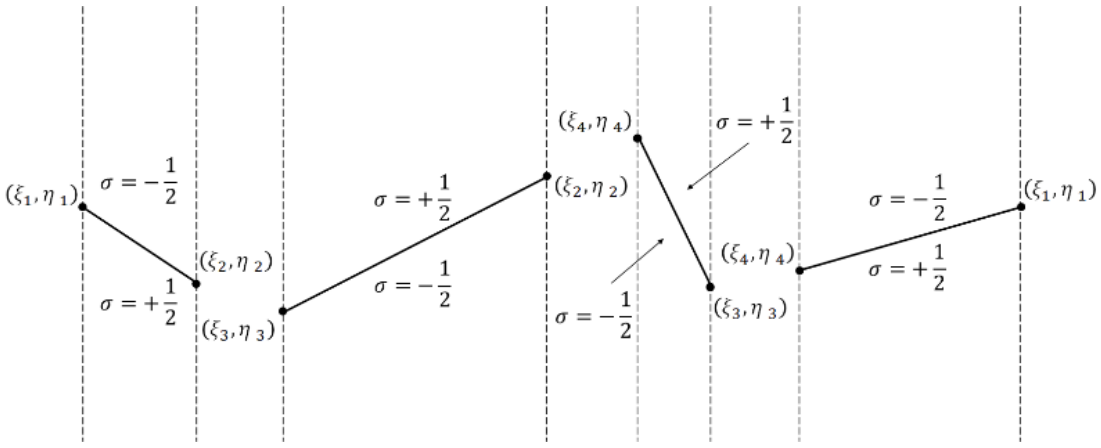

Figure 4.8 Quadrilateral strip split

where, $\eta_{k,k+1}$ indicates the η coordinate of a point on the side of the quadrilateral. Furthermore, the following equations are obtained by executing the integration shown in the Eq. (4.20).

$$\left.\begin{aligned} V_{sl_{xk,k+1}} &= \frac{\eta_{k+1}-\eta_k}{d_{k,k+1}} \ln\left(\frac{r_k + r_{k+1} - d_{k,k+1}}{r_k + r_{k+1} + d_{k,k+1}}\right), \\ V_{sl_{yk,k+1}} &= \frac{\xi_{k+1}-\xi_k}{d_{k,k+1}} \ln\left(\frac{r_k + r_{k+1} - d_{k,k+1}}{r_k + r_{k+1} + d_{k,k+1}}\right), \\ V_{sl_{zk,k+1}} &= \tan^{-1}\frac{m_{k,k+1}e_k - h_k}{zr_k} - \tan^{-1}\frac{m_{k,k+1}e_{k+1} - h_{k+1}}{zr_{k+1}}, \end{aligned}\right\} \tag{4.21}$$

where,

$$\left.\begin{aligned} r_k &= [(x-\xi_k)^2 + (y-\eta_k)^2 + z^2]^{1/2}, \\ r_{k+1} &= [(x-\xi_{k+1})^2 + (y-\eta_{k+1})^2 + z^2]^{1/2}, \\ d_{k,k+1} &= [(\xi_{k+1}-\xi_k)^2 + (\eta_{k+1}-\eta_k)^2]^{1/2}, \\ e_k &= z^2 + (x-\xi_k)^2, \\ e_{k+1} &= z^2 + (x-\xi_{k+1})^2, \\ h_k &= (y-\eta_k)(x-\xi_k), \\ h_{k+1} &= (y-\eta_{k+1})(x-\xi_{k+1}), \\ m_{k,k+1} &= \frac{\eta_{k+1}-\eta_k}{\xi_{k+1}-\xi_k}. \end{aligned}\right\} \tag{4.22}$$

Finally, induced velocity vector $\overrightarrow{V_{sl}}$ are given by the sum of the induced velocity by the four pairs of semi-infinite strips as follows,

$$\overrightarrow{V_{sl}} = \sum_{k=1}^{4} \left(\overrightarrow{\iota_\xi} V_{sl_{xk,k+1}} + \overrightarrow{J_\eta} V_{sl_{yk,k+1}} + \overrightarrow{k_\zeta} V_{sl_{zk,k+1}}\right), \tag{4.23}$$

where, $\overrightarrow{\iota_\xi}$, $\vec{j}_\eta$, and $\overrightarrow{k_\zeta}$ are unit vectors in the panel coordinate system.

After calculating the induced velocity from the sources expressed in the panel fixed coordinate system, it is necessary to convert it back to the basic coordinate system. This is because hydrodynamic forces acting on the body is handled in the basic coordinate system. The induced velocity vector $\overrightarrow{V_s}$ at arbitrary point by a source of strength σ in the basic coordinate system is expressed by the following equation using the induced velocity vector $\overrightarrow{V_{sl}}$,

$$\overrightarrow{V_s} = \sigma \boldsymbol{M}^{-1} \overrightarrow{V_{sl}}, \tag{4.24}$$

where, $\boldsymbol{M}$ is the conversion matrix to perform the conversion from the panel fixed coordinate system $O-\xi\eta\zeta$ to the basic coordinate system $O-xyz$ based on Eq. (4.16).

4.3.4. Induced Velocity by All Sources distributed on Quadrilateral Surface

Total induced velocity vector by all sources distributed on quadrilateral panels is expressed as the sum of the induced velocity vectors due to each quadrilateral panel. Let M be the number of quadrilateral panels used to approximate the body surface and i be the number of arbitrary quadrilateral panel, then the induced velocity vector $\overrightarrow{V_s}$ by the entire source panels is given by the following equation,

$$\overrightarrow{V_s} = \sum_{i=1}^{M} \sigma_i \boldsymbol{M}_i^{-1} \overrightarrow{V_{sl}}. \tag{4.25}$$

By using normal vector $\vec{n}$ at an arbitrary calculation point, the boundary conditions at the calculation point is expressed by the following equation,

$$\overrightarrow{V_s} \cdot \vec{n} = \sum_{i=1}^{M} \sigma_i C_{si}, \tag{4.26}$$

where,

$$C_{si} = \boldsymbol{M}_i^{-1} \overrightarrow{V_{sl_i}} \cdot \vec{n}\,. \tag{4.27}$$

C_{si} is influence coefficient representing the velocity induced by the i-th source panel having unit source strength.

4.4. Calculation Method of Induced Velocity by Horseshoe Vortices

4.4.1. Horseshoe Vortices

Assuming a body in uniform flow is represented by its central longitudinal plane, the basic coordinate system shown in Fig. 4.9 is expressed as same as the coordinate system shown in Fig. 4.2. In here, the positive directions of x, y, and z axes are backward, port side, and upward, respectively. Then discrete horseshoe vortices having shedding angle

Θ with respect to the xz plane are distributed on the central longitudinal plane. The x coordinate of each horseshoe vortex is defined as follows,

$$x_{\mu\nu} = \frac{L}{2}\left(1 - \cos\frac{2\nu - 1}{2N_\nu}\pi\right), \quad \mu = 1,\cdots,N_\mu, \quad \nu = 1,\cdots,N_\nu, \tag{4.28}$$

where, L is ship length and N_μ and N_ν are the numbers of division in vertical and longitudinal directions of the central longitudinal plane, respectively.

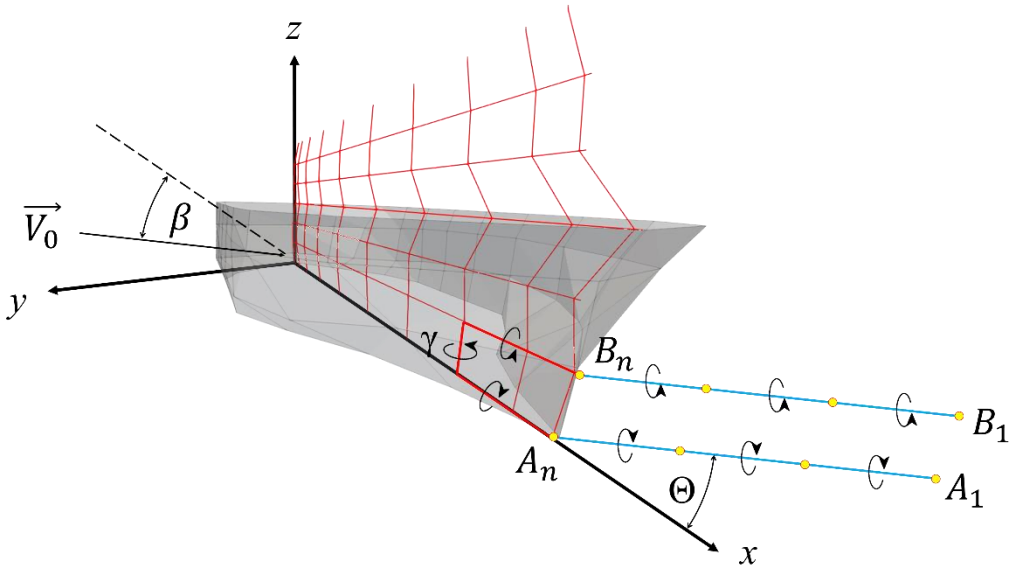

Figure 4.9 Horseshoe vortex implemented at the stern part of the ship hull

4.4.2. Induced Velocity by Horseshoe Vortices

Let assume that a horseshoe vortex $A_1A_nB_nB_1$ shown in Fig. 4.9 is the one of the horseshoe vortices distributed on the central longitudinal plane and it has unit vortex strength. The horseshoe vortex consists of a bound vortex (A_nB_n) and two free vortices (A_1A_n and B_nB_1) represented by red and blue lines, respectively. Furthermore, the free vortices are formed by some vortex elements with nodes represented by yellow dots to consider the deformation of the free vortices. One single free vortex element consists of one blue line and two yellow dots. Then, the number of elements in each free vortex is represented by n_E.

Theoretically, the length of free vortex l_v is infinity. In here, assumption is introduced to the length of free vortex. The closer free vortex node to the calculation point placed on the central longitudinal plane, the larger the influence caused by that. On the other hand, the farthest free vortex node to the calculation point gives very small influence. Based on these, it is assumed that the length of free vortex is limited until the influence of the farthest position of free vortex node to the calculation point are very small or almost 0. After assuming the length of free vortex l_v, the length of each vortex element l_E is defined as follow,

$$l_E = l_v/n_E, \tag{4.29}$$

where, n_E is the number of vortex elements in a free vortex. Then, distance between κ-th node in a free vortex and the assumed endpoint of the free vortex can be defined by this following formula,

$$\lambda_\kappa = l_v - l_E(\kappa - 1), \qquad \kappa = 1,\cdots, n_E + 1. \tag{4.30}$$

Based on Eq. (4.30), the coordinate of each node in the basic coordinate system $O - xyz$ are defined by this following equations,

$$\left.\begin{aligned} P^\kappa_{\mu\nu_x} &= x_{\mu\nu} + \lambda_\kappa \cos\Theta, \quad \mu = 1,\cdots,N_\mu, \quad \nu = 1,\cdots N_\nu, \quad \kappa = 1,\cdots,n_E+1,\\ P^\kappa_{\mu\nu_y} &= \lambda_\kappa \sin\Theta, \qquad \kappa = 1,\cdots,n_E+1,\\ P^\kappa_{\mu\nu_z} &= (\mu-1)\frac{d}{N_\mu}, \qquad \mu = 1,\cdots,N_\mu+1, \end{aligned}\right\} \tag{4.31}$$

where,

$P^\kappa_{\mu\nu_x}, P^\kappa_{\mu\nu_y}, P^\kappa_{\mu\nu_z}$: Coordinate of each node of free vortex corresponding $x_{\mu\nu}$ in the basic coordinate system,

$x_{\mu\nu}$: x coordinate of k-th horseshoe vortex based on Eq. (4.28),

Θ : Shedding angle of free vortex,

d : Ship draft.

By using Biot-Savart law, velocity vector $\vec{v}$ induced by the horseshoe vortex $A_1A_nB_nB_1$ at an arbitrary point $P(x,y,z)$ is given by the following equation,

$$\vec{v} = \left\{K^{(b)}(x,y,z) + K^{(f1)}(x,y,z) + K^{(f2)}(x,y,z)\right\}\vec{e}, \tag{4.32}$$

where,

$$\left.\begin{aligned} K^{(b)}(x,y,z) &= \frac{1}{4\pi\left|\overrightarrow{PH_b}\right|}\left(\frac{\overrightarrow{PB}\cdot\overrightarrow{AB}}{\left|\overrightarrow{PB}\right|\left|\overrightarrow{AB}\right|} - \frac{\overrightarrow{PA}\cdot\overrightarrow{AB}}{\left|\overrightarrow{PA}\right|\left|\overrightarrow{AB}\right|}\right), \\ K^{(f1)}(x,y,z) &= \sum_{j=1}^{n_E}\frac{1}{4\pi\left|\overrightarrow{PH_{f1,n}}\right|}\left(\frac{\overrightarrow{PA_{J+1}}\cdot\overrightarrow{A_JA_{J+1}}}{\left|\overrightarrow{PA_{J+1}}\right|\left|\overrightarrow{A_JA_{J+1}}\right|} - \frac{\overrightarrow{PA_J}\cdot\overrightarrow{A_JA_{J+1}}}{\left|\overrightarrow{PA_J}\right|\left|\overrightarrow{A_JA_{J+1}}\right|}\right), \\ K^{(f2)}(x,y,z) &= \sum_{j=1}^{n_E}\frac{1}{4\pi\left|\overrightarrow{PH_{f2,n}}\right|}\left(\frac{\overrightarrow{PB_{J+1}}\cdot\overrightarrow{B_JB_{J+1}}}{\left|\overrightarrow{PB_{J+1}}\right|\left|\overrightarrow{B_JB_{J+1}}\right|} - \frac{\overrightarrow{PB_J}\cdot\overrightarrow{B_JB_{J+1}}}{\left|\overrightarrow{PB_J}\right|\left|\overrightarrow{B_JB_{J+1}}\right|}\right). \end{aligned}\right\} \tag{4.33}$$

H_b, H_{f1}, and H_{f2} are the feet of perpendicular drawn from the point P to the line segments of the bound vortex A_nB_n, the free vortex A_jA_{j+1}, and the free vortex $B_{j+1}B_j$. $K^{(b)}$, $K^{(f1)}$, and $K^{(f2)}$ are influence functions of the vortices, respectively, n_E is the number of elements in single free vortex and j is the number of nodes of the free vortex. The vector $\vec{e}$ is a unit vector representing the direction of the induced velocity.

4.4.3. Induced Velocity by Horseshoe Vortices Distributed on Central Longitudinal Plane of Body

Let the strength of each horseshoe vortex be $\gamma_{\mu\nu}(\mu = 1,\cdots,N_\mu;\ \nu = 1,\cdots,N_\nu)$ and the induced velocity vector by a horseshoe vortex having unit strength be $\overrightarrow{v_{\mu\nu}}$, the induced velocity vectors $\overrightarrow{V_v}$ by all the horseshoe vortices on the central longitudinal plane of the body are given by the following equation,

$$\overrightarrow{V_v} = \frac{\pi}{2N_\nu}\sum_{\mu=1}^{N_\mu} L\sum_{\nu=1}^{N_\nu}\gamma_{\mu\nu}\overrightarrow{v_{\mu\nu}}\sin\left(\frac{2\nu-1}{N_\nu}\pi\right). \tag{4.34}$$

Further, assuming that the number of horseshoe vortices is $N\left(= N_\nu \times N_\mu\right)$ and normal vector at an arbitrary calculation point, Eq. (4.34) can be expressed as the following equation,

$$\overrightarrow{V_\nu} \cdot \vec{n} = \sum_{j=1}^{N} \gamma_j C_{\nu j}, \tag{4.35}$$

where,

$$C_{\nu j} = \frac{\pi L}{2N_\nu} \sin\left(\frac{2\nu - 1}{N_\nu}\pi\right) \overrightarrow{v_{\mu\nu}} \cdot \vec{n}, \quad j = (\mu - 1) \times N_\nu + \nu, \quad \left(\mu = 1, \cdots, N_\mu \;\; ; \;\; \nu = 1, \cdots, N_\nu\right). \tag{4.36}$$

j represents the sequential number of the horseshoe vortices, and C_{ν_j} is an influence coefficient representing the induced velocity by the j-th horseshoe vortex having unit strength. ν and μ are the numbers of division in the x-axis and z-axis directions, respectively.

4.5. Vortex Model

In this study, two kinds of vortex models shed from the hull are investigated. The simplified version of first and the second models (later referred as model 1 and model 2 respectively) are shown in Fig. 4.10. In the model 1, all free vortices of horseshoe vortices distributed along the central longitudinal plane are assumed to be shed from the stern of the hull. On the other hand, in the model 2, free vortices of horseshoe vortices located at ship bottom are assumed to be shed from the bottom. It is considered that this model is close to real phenomenon around the bottom of the hull. Free vortices of other horseshoe vortices are shed from the stern as same as the model 1.

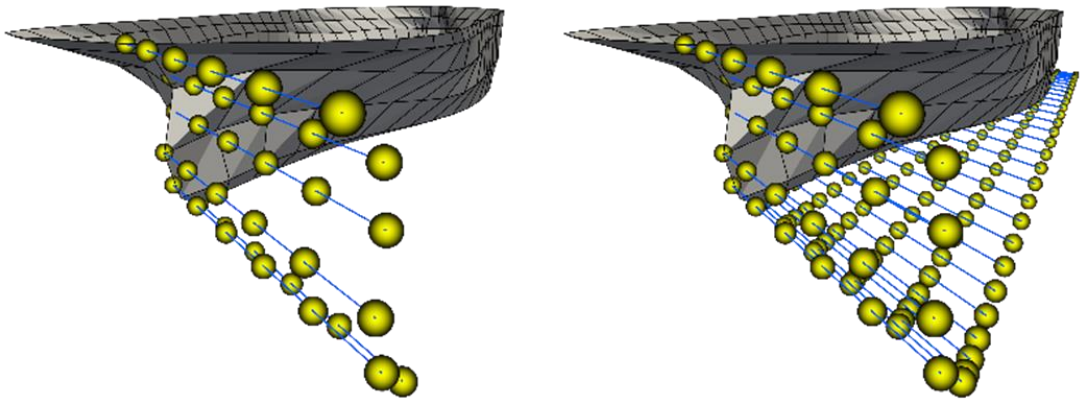

Figure 4.10 Model 1 (left) and model 2 (right) outflow method

4.6. Boundary Conditions

In the SQCM, the source strength σ_i $(i = 1, \cdots, M)$ and the vortex strength γ_j $(j = 1, \cdots, N)$ are resolved by satisfying the boundary conditions assuming that the flow does not pass through the body surface where the source panel is placed and the central longitudinal plane of the body where the vortex is arranged. The boundary conditions are represented by the following equation,

$$\overrightarrow{V_k} \cdot \overrightarrow{n_k} = 0 \quad (k = 1,2, \dots, M + N), \tag{4.37}$$

where, $\overrightarrow{V_k}$ and $\overrightarrow{n_k}$ are the flow velocity and the normal vector at the k-th calculation point. From Eq. (4.37), the following equation can be obtained,

$$\sum_{i=1}^{M} \sigma_i C_{si,k} + \sum_{j=1}^{N} \gamma_j C_{vj,k} + H_k = 0 \quad (k = 1,2, \dots, M + N), \tag{4.38}$$

where,

$$H_k = \overrightarrow{V_0} \cdot \overrightarrow{n_k} \quad (k = 1,2, \dots, M + N). \tag{4.39}$$

$\overrightarrow{V_0}$ is flow velocity vector by uniform flow around the body. When Eq. (4.38) is displayed in a matrix, it can be expressed as follows,

$$\begin{pmatrix} C_{s_{1,1}} & \cdots & C_{s_{1,M}} & C_{v_{1,1}} & \cdots & C_{v_{1,N}} \\ \vdots & \ddots & \vdots & \vdots & \ddots & \vdots \\ C_{s_{M,1}} & \cdots & C_{s_{M,M}} & C_{v_{M,1}} & \cdots & C_{v_{M,N}} \\ C_{s_{M+1,1}} & \cdots & C_{s_{M+1,M}} & C_{v_{M+1,1}} & \cdots & C_{v_{M+1,N}} \\ \vdots & \ddots & \vdots & \vdots & \ddots & \vdots \\ C_{s_{M+N,1}} & \cdots & C_{s_{M+N,M}} & C_{v_{M+N,1}} & \cdots & C_{v_{M+N,N}} \end{pmatrix} \begin{pmatrix} \sigma_1 \\ \vdots \\ \sigma_M \\ \gamma_1 \\ \vdots \\ \gamma_N \end{pmatrix} + \begin{pmatrix} H_1 \\ \vdots \\ H_M \\ H_{M+1} \\ \vdots \\ H_{M+N} \end{pmatrix} = 0. \tag{4.40}$$

By solving Eq. (4.40), the source strength σ_i of each hull panel and the vortex strength γ_j of each horseshoe vortex can be determined.

4.7. Additional Node and Moving Node of Free Vortex

After solving the matrix equation Eq. (4.40), the source strength and vortex strength which satisfy the boundary conditions can be obtained. Then, induced velocity at arbitrary points by all source panels can be calculated by Eq. (4.25) and induced velocity by all

horseshoe vortices can be calculated by Eq. (4.34), respectively. By multiplying total velocity which consists of uniform flow velocity and induced velocities by source panels and horseshoe vortices with time step settled in advance, the moving distance of free vortex node s_{V_x}, s_{V_y}, and s_{V_z} for each time step in each direction can be expressed as follow,

$$\left.\begin{aligned} s_{V_x} &= \left(V_{0_x} + V_{s_x} + V_{v_x}\right)\Delta t, \\ s_{V_y} &= \left(V_{0_y} + V_{s_y} + V_{v_y}\right)\Delta t, \\ s_{V_z} &= \left(V_{0_z} + V_{s_z} + V_{v_z}\right)\Delta t, \end{aligned}\right\} \tag{4.41}$$

where,

Δt : Time step (second).

By adding moving distance calculated by Eq. (4.41) to the coordinate of free vortex node defined by Eq. (4.31), it will make the nodes of free vortices move from their original position. After obtaining new coordinates of free vortices nodes, Eq. (4.40) is solved again to obtain new source strength and new vortex strength. According to the induced velocity calculated by using updated source strength and vortex strength, the coordinates of the new positions of free vortices nodes are calculated again.

Figs. 4.11 and 4.12 show the original position of free vortices and simplified example of moving free vortices in $O - xz$ plane of the basic coordinate system shown in Fig. 4.10, respectively. After several iterations of time steps, length between the position of the last vortex node which is located at the central longitudinal plane of a ship and a vortex node which is the nearest to the last node becomes longer than other vortex elements as shown in Fig. 4.12. The distance can be expressed as follows,

$$l_{E_{near}} = \sqrt{\left(P_{move_x} - P_{base_x}\right)^2 + \left(P_{move_y} - P_{base_y}\right)^2 + \left(P_{move_z} - P_{base_z}\right)^2}, \tag{4.42}$$

where P_{base} indicates the position of the last node at the central longitudinal plane and P_{move} indicates the position of the nearest node.

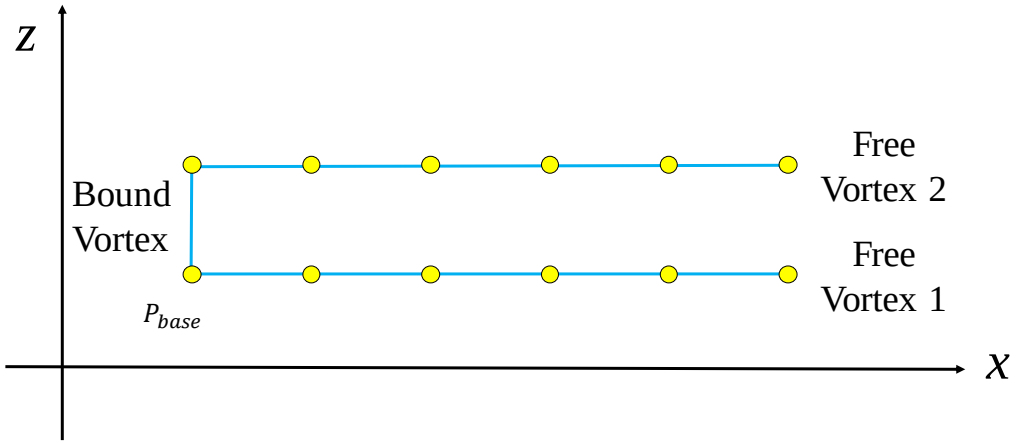

Figure 4.11 Original position of free vortices

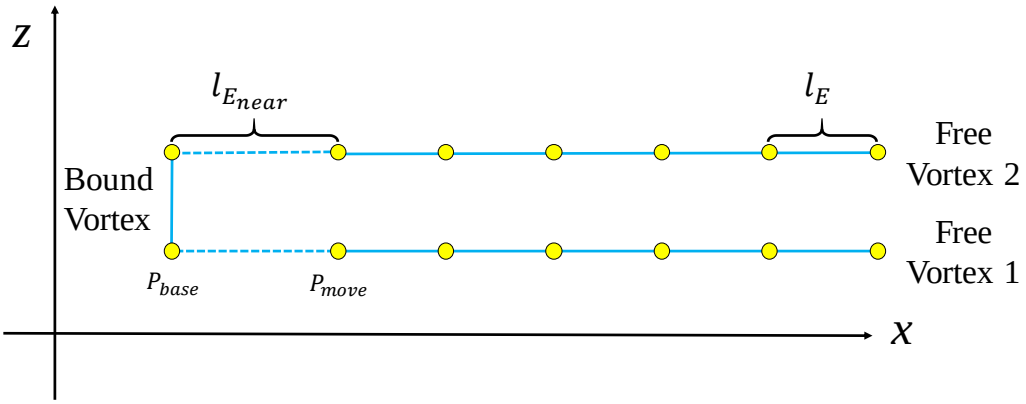

Figure 4.12 Example of moving free vortices

When the length of $l_{E_{near}}$ exceeds the length of l_E which is the general length of vortex node calculated by Eq. (4.29), an additional node of free vortex node is added at P_{plus} which is located between the position of last node, P_{base} and the position of the nearest node, P_{move} as shown in Fig. 4.13 to calculate the deformation of free vortex properly. Then, the coordinate of the additional node of free vortex can be determined by the following formula,

$$\left.\begin{aligned} P_{plus_x} &= P_{move_x} + \left(\frac{l_E}{l_{E_{near}}}\right)\left(P_{move_x} - P_{base_x}\right), \\ P_{plus_y} &= P_{move_y} + \left(\frac{l_E}{l_{E_{near}}}\right)\left(P_{move_y} - P_{base_y}\right), \\ P_{plus_z} &= P_{move_z} + \left(\frac{l_E}{l_{E_{near}}}\right)\left(P_{move_z} - P_{base_z}\right). \end{aligned}\right\} \quad (4.43)$$

After obtaining the coordinates of additional nodes, the length of the nearest vortex element for each free vortex is needed to be calculated again.

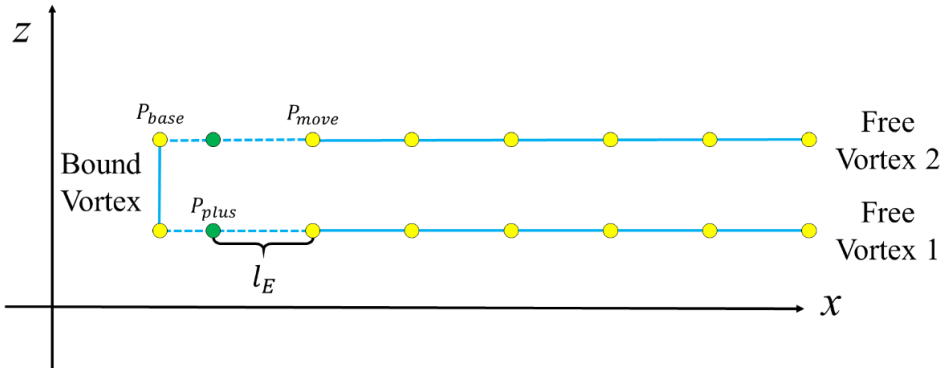

Figure 4.13 Additional node of free vortex

Fig. 4.14 shows the examples of deformation of free vortices for the vortex model 1 and the model 2, respectively. From the viewpoint of visibility, the numbers of free vortices and iteration shown in the figures are smaller than those used in calculations.

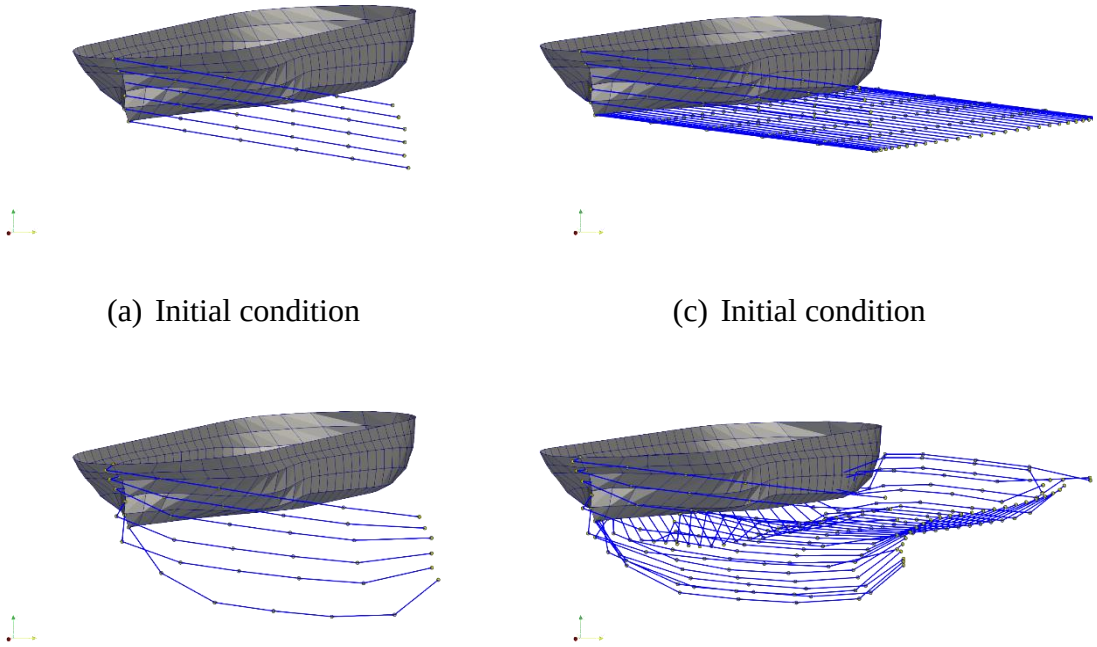

(a) Initial condition (c) Initial condition

(b) After 10th iteration (d) After 10th iteration

Figure 4.14 Examples of deformation of free vortex for model 1 (left) and model 2 (right)

4.8. Calculation Method of SQCM for Every Time Step

Fig. 4.15 shows the calculation flow of the SQCM. First, input data such as number of source panels, number of free vortex elements, the length of free vortex, etc. are determined. Hull panels based on the input data are created and null point calculated to obtained normal vector $\vec{n}$. Then, influence coefficient by source panels to source panels can be determined by using Eq. (4.27).

Calculation points and vortex points are determined to calculate influence coefficient by free vortices. The coordinates of free vortices nodes are calculated by using Eq. (4.31) and the length of free vortex are determined. Furthermore, influence coefficient by source panels to free vortices nodes, influence coefficient by free vortices to free vortices, and influence coefficient by free vortices to source panels can be calculated.

By calculating all possible influences from source panels and free vortices, boundary conditions can be obtained. Then, by solving matrix equation from Eq. (4.40) the source strength for each source panel and the vortex strength for each free vortex can be determined.

Fig. 4.16 shows the schematic method of the SQCM for every time step. After getting the values of source and vortex strength from Eq. (4.40), flow velocity at every nodes of free vortices can be calculated. This will make every nodes of free vortices move due to the influence of uniform flow and induced velocities by sources and other vortices. Based on that, the author considers the deformation of the shape of free vortices. Then, Eq. (4.40) is solved again to obtain the values of source and vortex strength which satisfy new boundary conditions updated by the motions of free vortices. These procedures are iterated for several time steps until the values of lateral force and yawing moment almost converge.

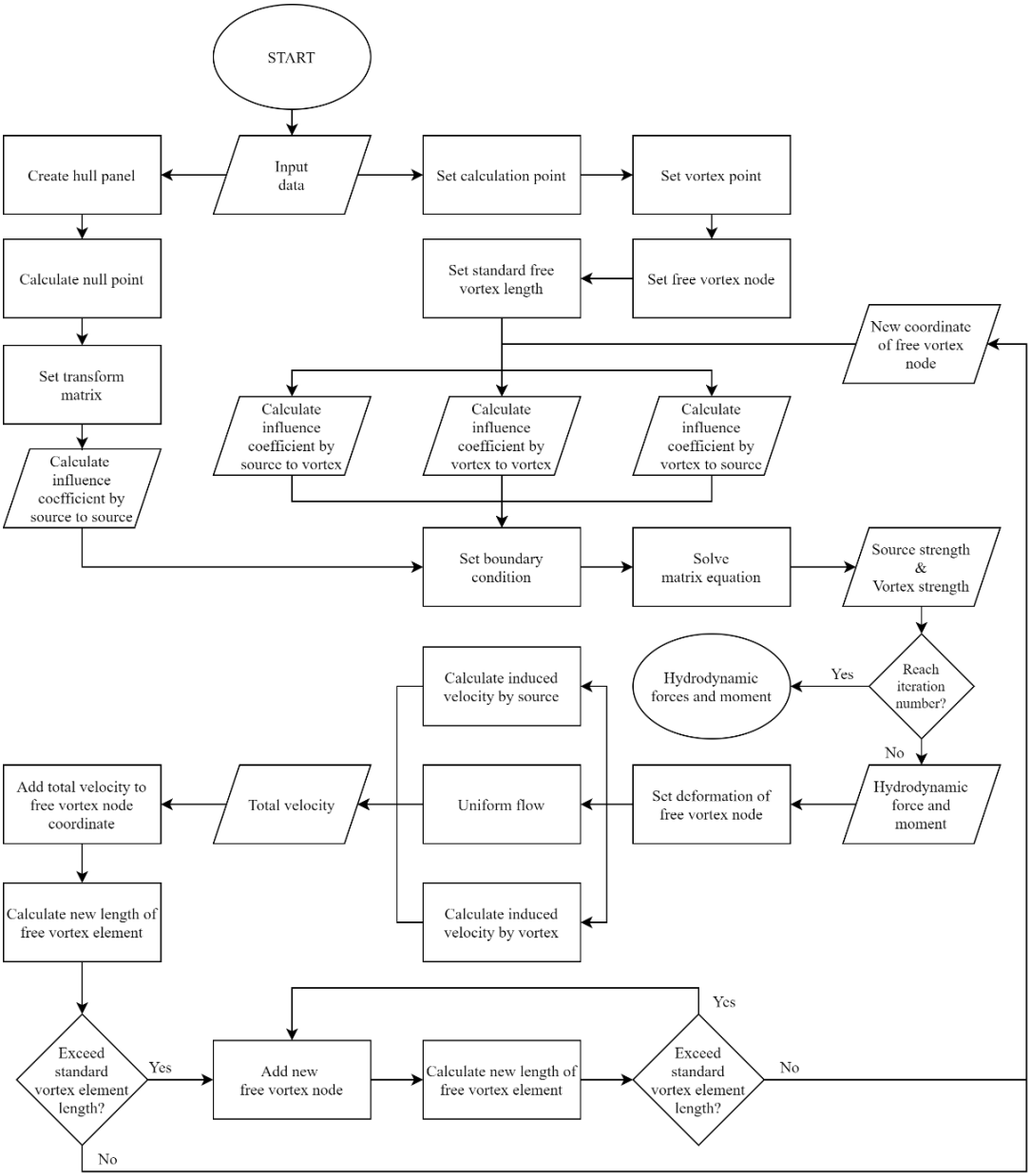

Figure 4.15 SQCM flowchart

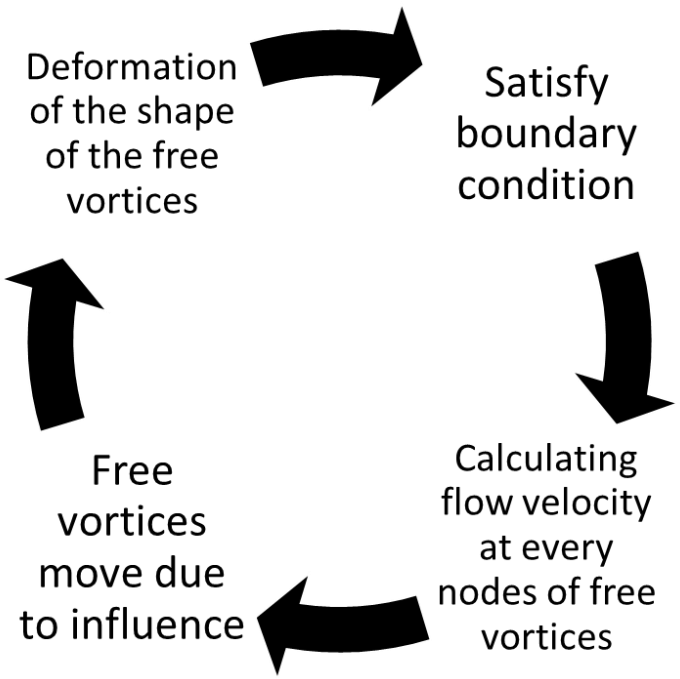

Figure 4.16 Calculation method of SQCM for every time step

4.9. Calculation Method of Hydrodynamic Force Coefficients

After the source strength σ and the vortex strength γ are obtained, the flow velocity vector $\vec{V}$ of the entire flow field can be determined. By using this entire flow velocity vector, the pressure coefficient C_p on the body surface is given by the following equation according to Bernoulli's theorem,

$$C_p = 1 - \frac{\left|\vec{V}\right|^2}{\left|\overrightarrow{V_0}\right|^2}. \tag{4.44}$$

Further, the lateral force F_y and the yawing moment M_z acting on the hull can be obtained by the following equations using the pressure coefficient C_p.

$$\left.\begin{aligned} F_y &= -\frac{\rho\left|\vec{V}\right|^2}{2}\int_S C_p n_y dS = -\frac{\rho\left|\vec{V}\right|^2}{2}\sum_{i=1}^{M} C_{p_i} n_{y_i} A_i\,, \\ M_z &= -\frac{\rho\left|\vec{V}\right|^2}{2}\int_S C_p\left(n_x y - n_y x\right) dS = -\frac{\rho\left|\vec{V}\right|^2}{2}\sum_{i=1}^{M} C_{p_i} n_{y_i} A_i\left(n_{x_i} y - n_{y_i} x\right), \end{aligned}\right\} \quad (4.45)$$

where,

ρ : fluid density,

i : source panel number,

n_{xi}, n_{yi} : x and y components of the i-th panel normal vector,

x, y : x and y coordinate of the i-th panel,

A_i : area of the i-th panel.

Finally, the following formulae are used to non-dimensionalize the hydrodynamic forces acting on the hull.

$$C_y = \frac{F_y}{\frac{1}{2}\rho S {V_0}^2}, \qquad C_m = \frac{M_z}{\frac{1}{2}\rho L^2 d {V_0}^2}, \quad (4.46)$$

where, S is the wetted surface area of the hull.

4.10.Conclusion

This chapter introduced the SQCM to predict lateral force and yawing moment acting on a ship hull representing the shape of the hull accurately. In this method, ship hull is treated as a thick wing. Hydrodynamic forces acting on the hull can be obtained by calculating induced velocity by sources and induced velocity by vortices. The Hess and Smith method is introduced to calculate induced velocity by sources and Biot-Savart law is applied to calculate induced velocity by vortices. Then, two kinds of vortex models with considering deformation of free vortices are proposed to represent the flow field around the hull. Furthermore, by satisfying the boundary conditions assuming the flow does not pass through the body surface and central longitudinal plane, source strength and vortex strength can be resolved. Finally, the flow velocity vector of the entire flow field and hydrodynamic forces acting on the hull can be determined.

Chapter 5 Application of SQCM

5.1. Introduction

In the previous chapter, the basic equation of the SQCM is introduced to predict lateral force and yawing moment acting on a ship hull. The calculation process of a flow field based on the SQCM can be divided into two main components. One is a calculation of induced velocity by sources and the other is calculation of induced velocity by horseshoe vortices. The distribution of sources is calculated based on the Hess and Smith (1964) method and the distribution of free vortices around a ship hull is represented based on the QCM presented by Lan (1970).

After getting the values of source and vortex strength which satisfy the boundary conditions, flow velocities at every nodes of free vortices can be calculated. This will make every nodes of free vortices move due to the influence of uniform flow and induced velocities by sources and other vortices. Based on that, vortex models considering deformation of free vortices are introduced in the previous chapter to represent the flow field around the hull appropriately.

In this chapter, the SQCM is applied to the three types of ship hull to investigate the applicability of the SQCM on the prediction of hydrodynamic forces acting on a ship hull. Two kinds of vortex models are applied to each hull to examine the estimation accuracy of lateral force and yawing moment acting on a ship hull in oblique motion. Pressure distribution and flow field around a ship hull are also investigated.

5.2. Application of SQCM to Wigley Hull

5.2.1. Hull Shape

The Wigley hull is a mathematical hull form that is symmetrical with respect to all directions. The shape of the Wigley hull is expressed by the following formula,

$$y(x,z) = \frac{B}{2}\left\{1-\left(\frac{x}{l}\right)^2\right\}\left\{1-\left(\frac{z}{c}\right)^2\right\}, \tag{5.1}$$

where,

B : Ship breadth,

l : Half ship length ($L/2$),

d : Ship draft.

Table 5.1 shows the principal particulars of a model ship of the Wigley hull that was used in a captive model test conducted at Kyushu University by Nakatake et al. (1994).

Table 5.1 Principal particulars of a model ship of Wigley hull

L (m)	2.500
B (m)	0.250
d (m)	0.156
C_b	0.444

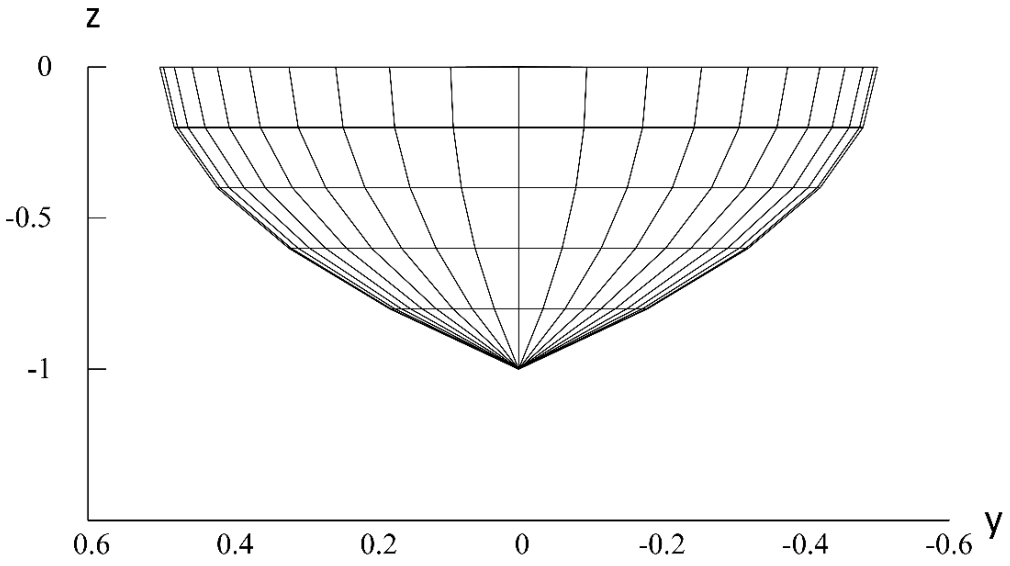

Figure 5.1 Body plan of Wigley hull

As shown in Fig. 5.1, the Wigley hull form has no flat part at the bottom of the ship and draws an arc from the keel in lateral direction of the ship. On the other hand, as shown in Fig. 5.2, the bow and the stern of the ship are vertical, and the distance between the bow

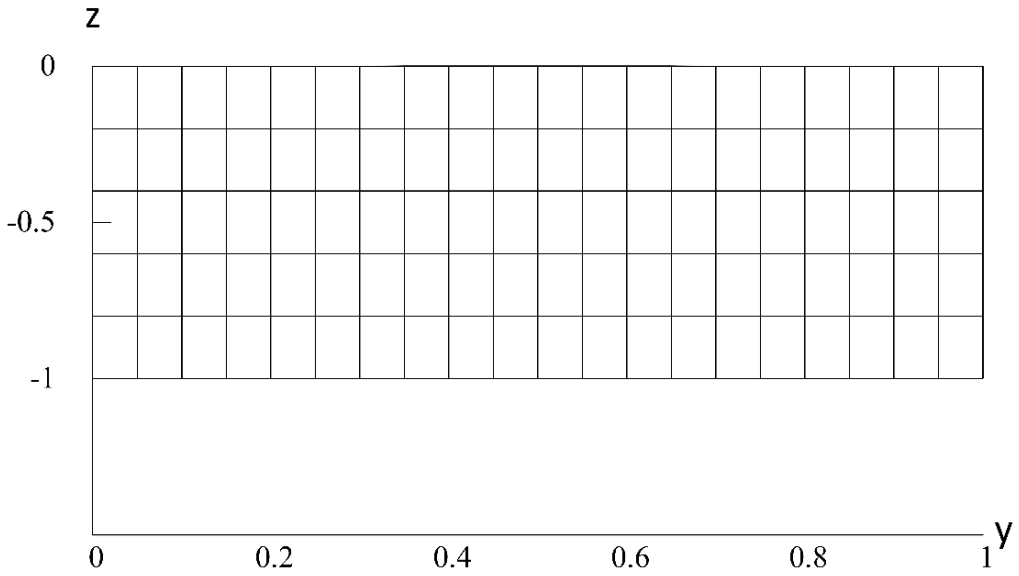

Figure 5.2 Side view of Wigley hull

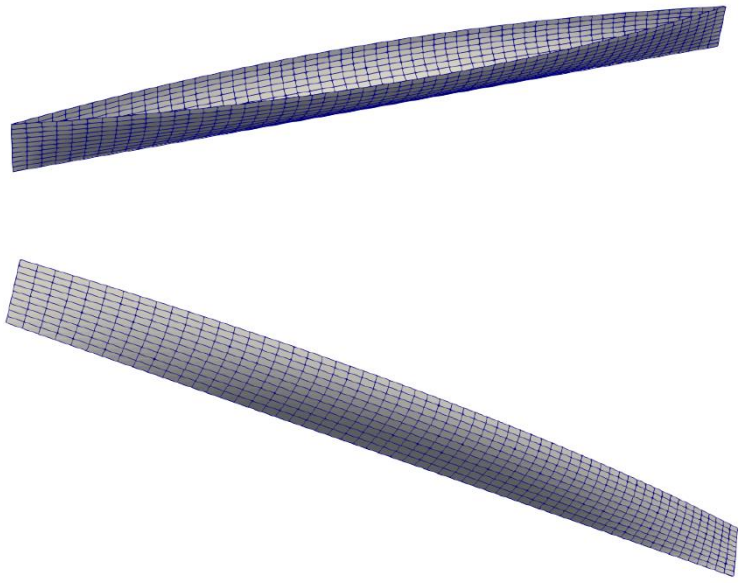

Figure 5.3 Wigley hull form

and the stern is equal regardless of the height from the bottom. Therefore, the shape is different from the actual ship hull form. Fig. 5.3 shows the Wigley hull form based on division numbers used in this research which are described later.

5.2.2. Calculation Conditions

Convergence test is executed to decide the number of divisions in vertical and longitudinal directions and the number of free vortex elements in the horseshoe vortices, at first. Table 5.2 shows the results of simulation time obtained from the convergence tests for the Wigley hull. The number of divisions in longitudinal direction ν is set from 30 to 50 at an interval of 10 and the number of divisions in vertical direction μ is set as 5 and 10. Then the number of free vortex elements is set as 50. The value of drift angle β is set as 10° and the vortex model 2 presented in the previous chapter is applied. Initial shedding angle of free vortices Θ is same as the value of drift angle β and a ship speed V_0 is set at 0.5 m/s.

Fig. 5.4 shows the comparison of non-dimensional lateral force coefficient C_y and non-dimensional yawing moment coefficient C_m for each longitudinal division number ν at drift angle $\beta = 10°$ using the vortex model 2. In the figure, lateral axis indicates the number of iteration and vertical axis represents the values of C_y or C_m. It is observed from the figure that similar results on the values of C_y and C_m for all longitudinal and vertical divisions numbers.

Table 5.2 Convergence test results.

Division number		Iteration number	Number of free vortex element
			50
ν	μ		Simulation time (minutes)
30	5	100	25
40			58
50			135
30	8		43
40			129
50			277

Based on the convergence test results and taking account of required simulation time, the numbers of divisions for the Wigley hull are selected as $\nu = 30$ in longitudinal direction and $\mu = 5$ in vertical direction and the number of free vortex element is set as 50.

Accordingly, the number of source panels arranged on the port and starboard sides of the hull becomes 600 ($= 30 \times 5 \times 2 \times 2$) including its mirror images. On the other hand, the number of free vortex arranged on the longitudinal plane of the hull is 300 ($= 30 \times 5 \times 2$).

5.2.3. Lateral Force and Yawing Moment

The shapes of free vortices are changed due to the influence of uniform flow and induced velocities by sources and other vortices. This will make the shape of free vortex deformed for every time step and cause the variation of the calculation results of lateral force and yawing moment with respect to time. Based on that, calculations are iterated until the value of lateral force and yawing moment become steady as shown in Fig. 5.4. According to the result shown in Fig. 5.4, it can be concluded that the values of lateral force and yawing moment become almost steady after the number of iterations n exceeds 60. Following this conclusion, the last iteration number ($n = 100$) is chosen as the base to evaluate the results of lateral force and yawing moment and then the values are compared with measured data.

Fig. 5.5 shows the calculation results of lateral force coefficient C_y and yawing moment coefficient C_m of the Wigley hull for the model 1 and the model 2 as the function of drift angle β. It can be observed that calculated lateral force coefficient C_y for the model 1 shown with red solid line in Fig. 5.5 (a) is too smaller than the measured results presented by black circles. Same tendency is also found in the results of yawing moment coefficient C_m. On the other hand, improvement of prediction accuracy for the lateral force coefficient C_y is observed for the model 2 as shown with blue solid line in Fig. 5.5 (a). However, the yawing moment coefficient C_m shown with blue solid line in Fig. 5.5 (b) is still smaller than the measured results, though the value of C_m for large drift angle is bigger than that for the model 1.

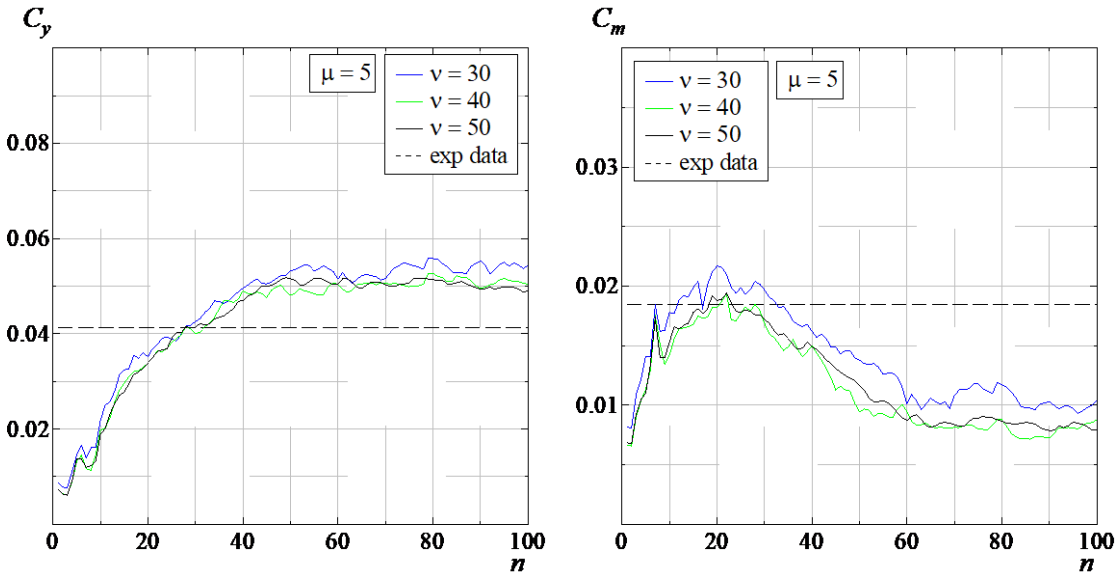

(a) C_y (μ = 5)

(b) C_m (μ = 5)

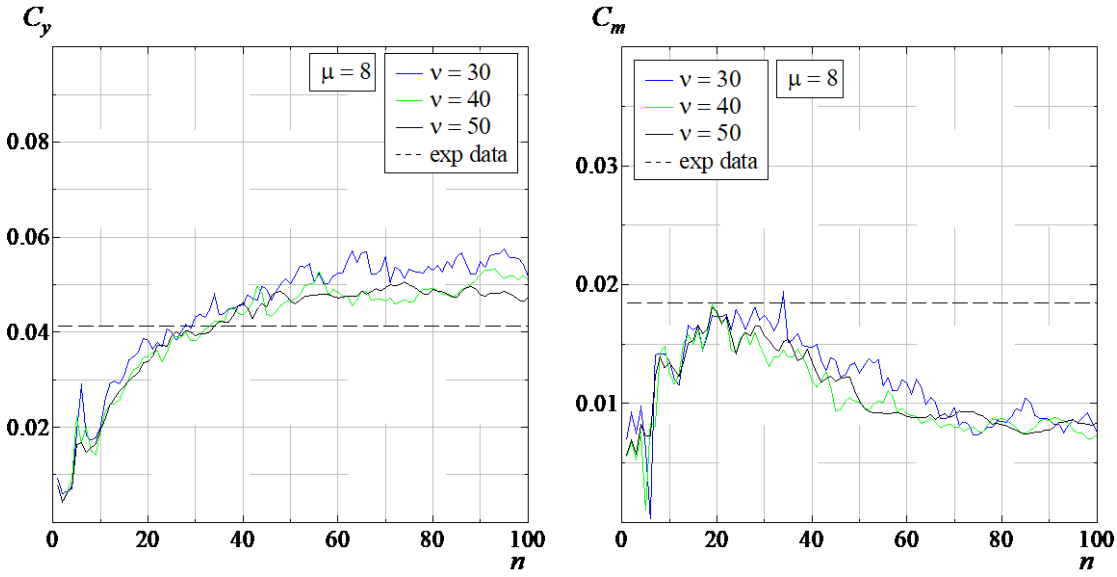

(c) C_y (μ = 8)

(d) C_m (μ = 8)

Figure 5.4 Comparison of lateral force coefficient C_y and yawing moment coefficient C_m (n_E = 50)

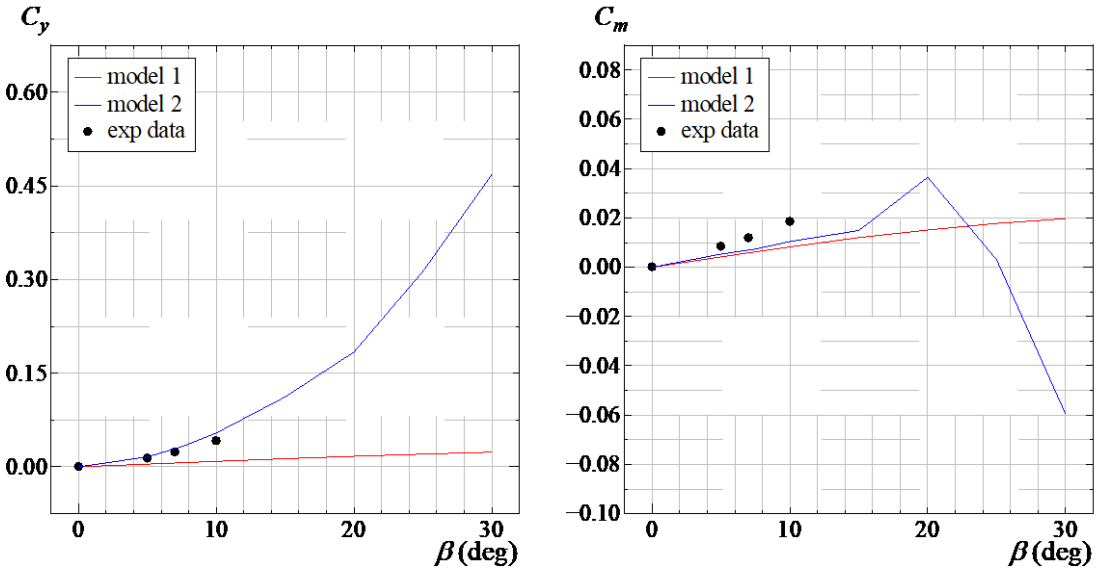

(a) Lateral force coefficient C_y (b) Yawing moment coefficient C_m

Figure 5.5 Wigley lateral force coefficient C_y and yawing moment coefficient C_m

5.2.4. Pressure Distribution

Pressure distributions around the ship hull at drift angle $\beta = 20°$ are presented in Figs. 5.6 and 5.7 for the Wigley hull with the vortex models 1 and 2. All of these results are presented at the iteration number $n = 100$. These figures show the values of pressure coefficient C_p with the positive pressure being red, the negative pressure being blue, and the 0 pressure being white. For simplicity, a mirror part of the double body model is omitted in the figure.

Upper and lower figures in Figs. 5.6 and 5.7 show pressure distributions on the port and the starboard sides for the vortex model 1 and the model 2, respectively. As for the pressure coefficients on the port side for both vortex models, no significant difference is seen in any of the models except for the pressure distribution at the bottom of the hull and around the stern. Lower pressure distribution is observed for the model 1.

On the other hand, significant difference can be observed between the pressure coefficients on the starboard sides for the vortex models 1 and 2. Pressure distribution on the starboard side for the model 1 is almost same as that on the port side. It can be considered that the small lateral force coefficient for the model 1 is caused by these small difference of pressure distribution between the starboard and the port sides. In contrast, difference in pressure distributions between the starboard and the port sides is clear for the model 2. It means that free vortices which are assumed to be shed from the bottom have remarkable effect on hydrodynamic forces acting on the hull.

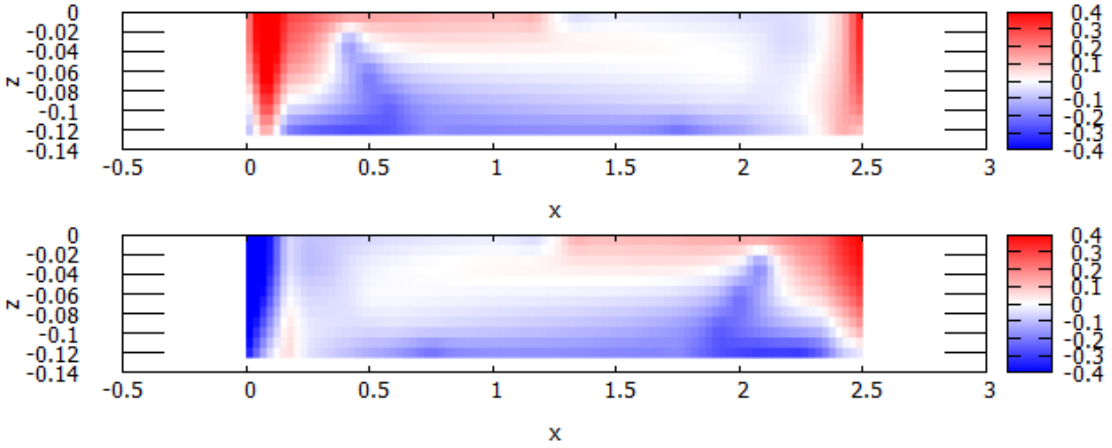

Figure 5.6 Pressure distribution on port side (up) and starboard side (down) of Wigley hull for model 1 ($\beta = 20°$)

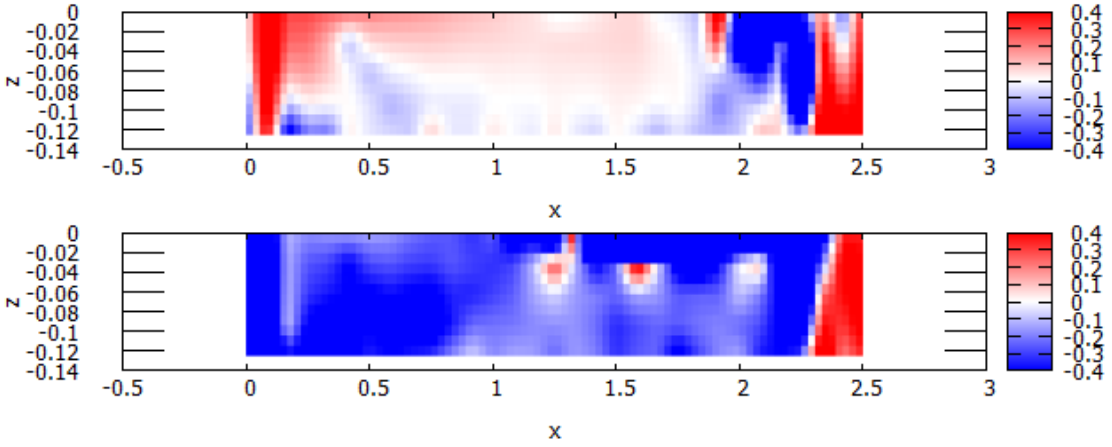

Figure 5.7 Pressure distribution on port side (up) and starboard side (down) of Wigley hull for model 2 ($\beta = 20°$)

5.2.5. Velocity Field

Figs. 5.8 and 5.9 show velocity fields around the starboard side of the Wigley hull including a mirror part of the double body model at the midship for the model 1 and the model 2, respectively. The value of drift angle β is set as 30°. Two batches of figures are sets of flow fields at the iteration number $n = 1$ and $n = 100$ to see the effect of free vortices deformation to flow velocity around the hull. Dots in the figures indicate the positions of reference points in the flow field and the length of arrows indicate the magnitude of flow velocity vector at the points. The size of presented flow field is set as 6 times of draft in z direction and 6 times of breadth in y direction of the basic coordinate system shown in Fig. 4.10.

It is understood from Fig. 5.8 that the model 1 in which vortices are shed only from the stern does not have deformation of free vortex around midship, because the velocity vectors at the midship remains almost same after 100 iterations. On the other hand, remarkable differences between flow fields at $n = 1$ and $n = 100$ is observed in Fig. 5.9. Rotational flow after leaving the hull bottom can be observed more clearly for the model 2.

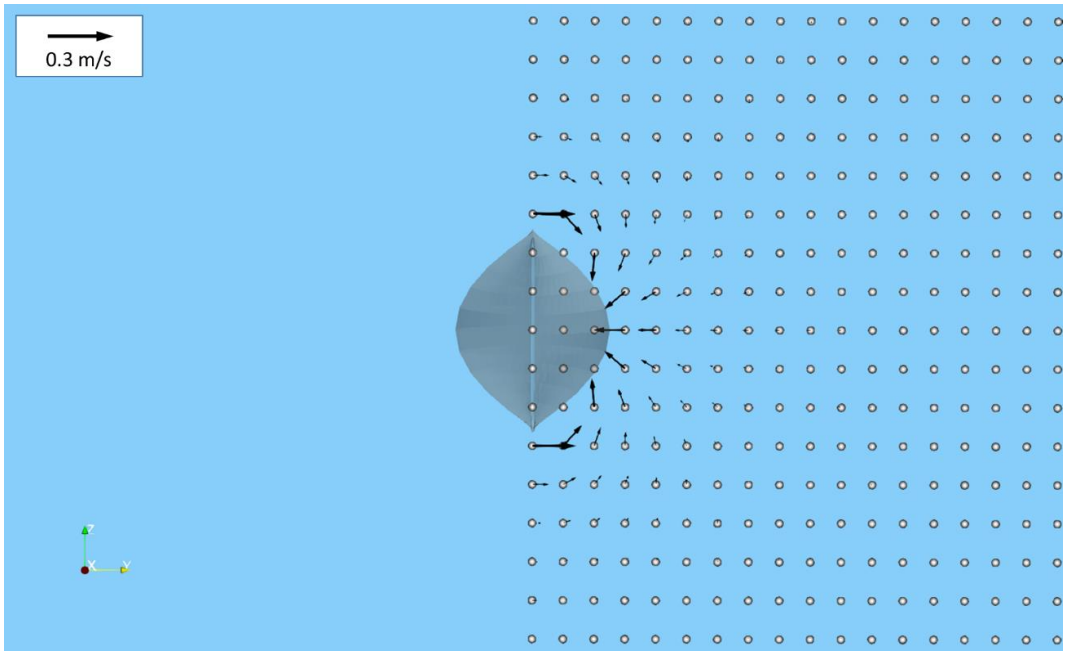

(a) $n = 1$

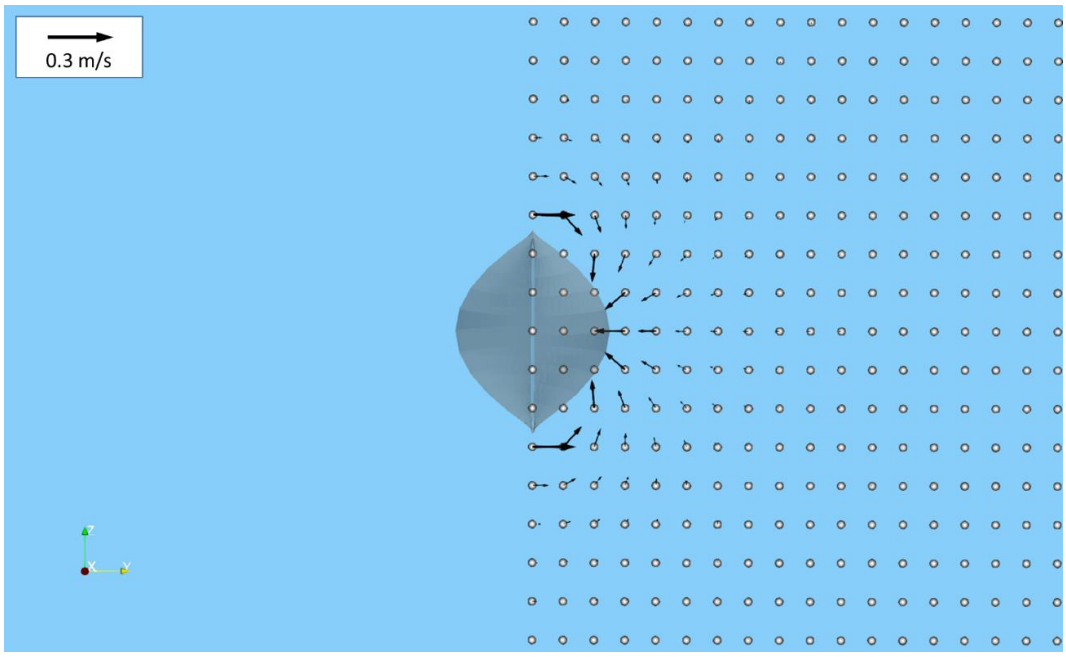

(b) $n = 100$

Figure 5.8 Flow velocity around the Wigley hull for model 1 ($\beta = 30^{\circ}$)

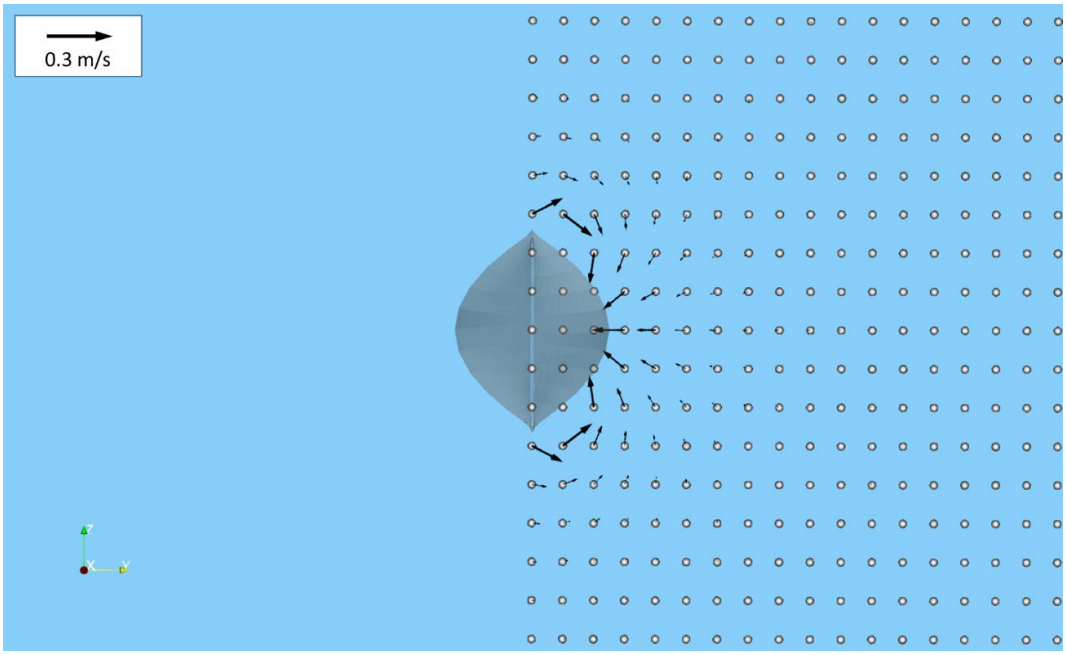

(a) $n = 1$

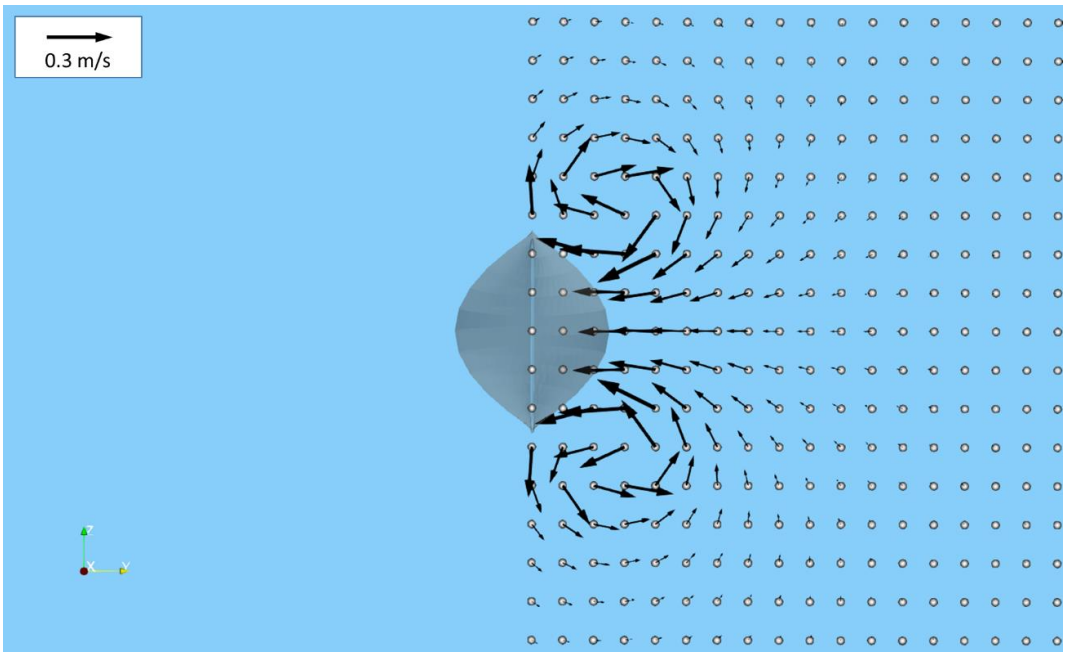

(b) $n = 100$

Figure 5.9 Flow velocity around the Wigley hull for model 2 ($\beta = 30^{\circ}$)

5.3. Application of SQCM to Actual Ship Hull

5.3.1 Hull Shape

Following the Wigley hull form, applicability of the SQCM for actual hull shape is examined. Table 5.3 shows the principal particulars of KCS and KVLCC2 hulls and Fig. 5.10 shows the hull forms of KCS and KVLCC2.

Table 5.3. Principal particular of KCS and KVLCC2.

	KCS		KVLCC2	
	Real	Model	Real	Model
L (m)	230.00	2.500	320.00	2.500
B (m)	32.20	0.350	58.00	0.453
d (m)	10.80	0.117	20.80	0.162
C_b	0.651		0.810	

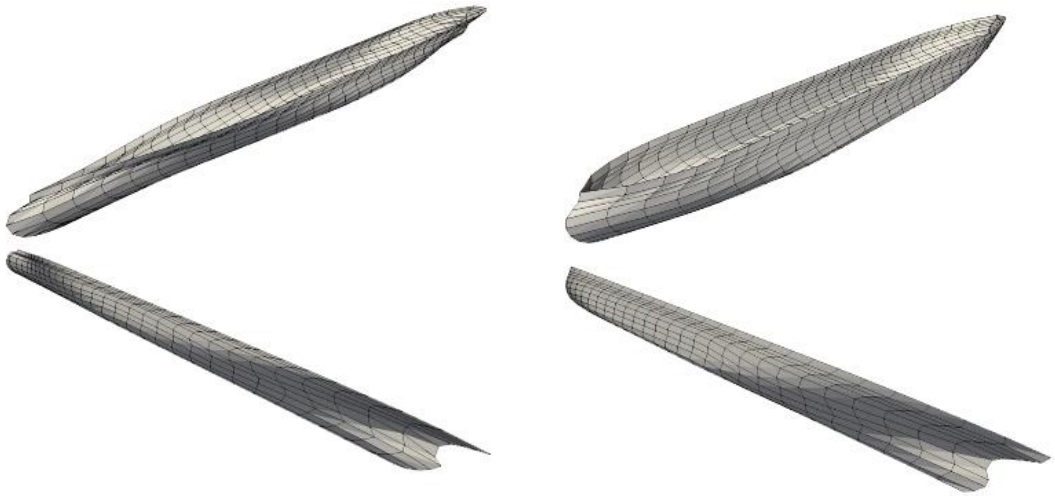

Figure 5.10 KCS model (left) and KVLCC2 model (right)

5.3.2 Calculation Conditions

Convergence test is executed to decide the number of divisions in vertical and longitudinal directions and the number of free vortex elements in the horseshoe vortices, at first. Table 5.4 shows the results of simulation time obtain from the convergence tests for KCS and KVLCC2. The number of divisions in longitudinal direction ν is set from 20 to 50 at an interval of 10 and the number of divisions in vertical direction μ is set as 5 and 8. In here, additional higher number of free vortex elements which is set as 70 is

implemented to investigate the effect of the deformation of free vortex elements to the predicted results of hydrodynamic forces. The value of drift angle β is set as 10° and the vortex model 2 presented in the previous chapter is applied. Ship speed V_0 is set at 0.3 m/s which corresponds to 5.6 kt for KCS and 6.6 kt for KVLCC2 in real ship scale. Initial vortex shedding angle Θ is set same as drift angle β.

Fig. 5.11 shows the comparison of C_y and C_m for each longitudinal division number ν at drift angle $\beta = 10°$ using the vortex model 2 and the number of free vortex elements is set as 50. It is obvious from the figure that the results are almost similar for all longitudinal division numbers. As for the results when the number of vortex elements is equal to 70, significant improvement in the results of C_y and C_m are not observed, but the simulation time is almost twice comparing with that for 50.

Table 5.4 Convergence test results.

Division number		Iteration number	Number of free vortex element	
			50	70
ν	μ		Simulation time (minutes)	
20	5	100	10	26
30			22	44
40			41	75
50			71	130
20	8		24	46
30			58	117
40			101	215
50			160	424

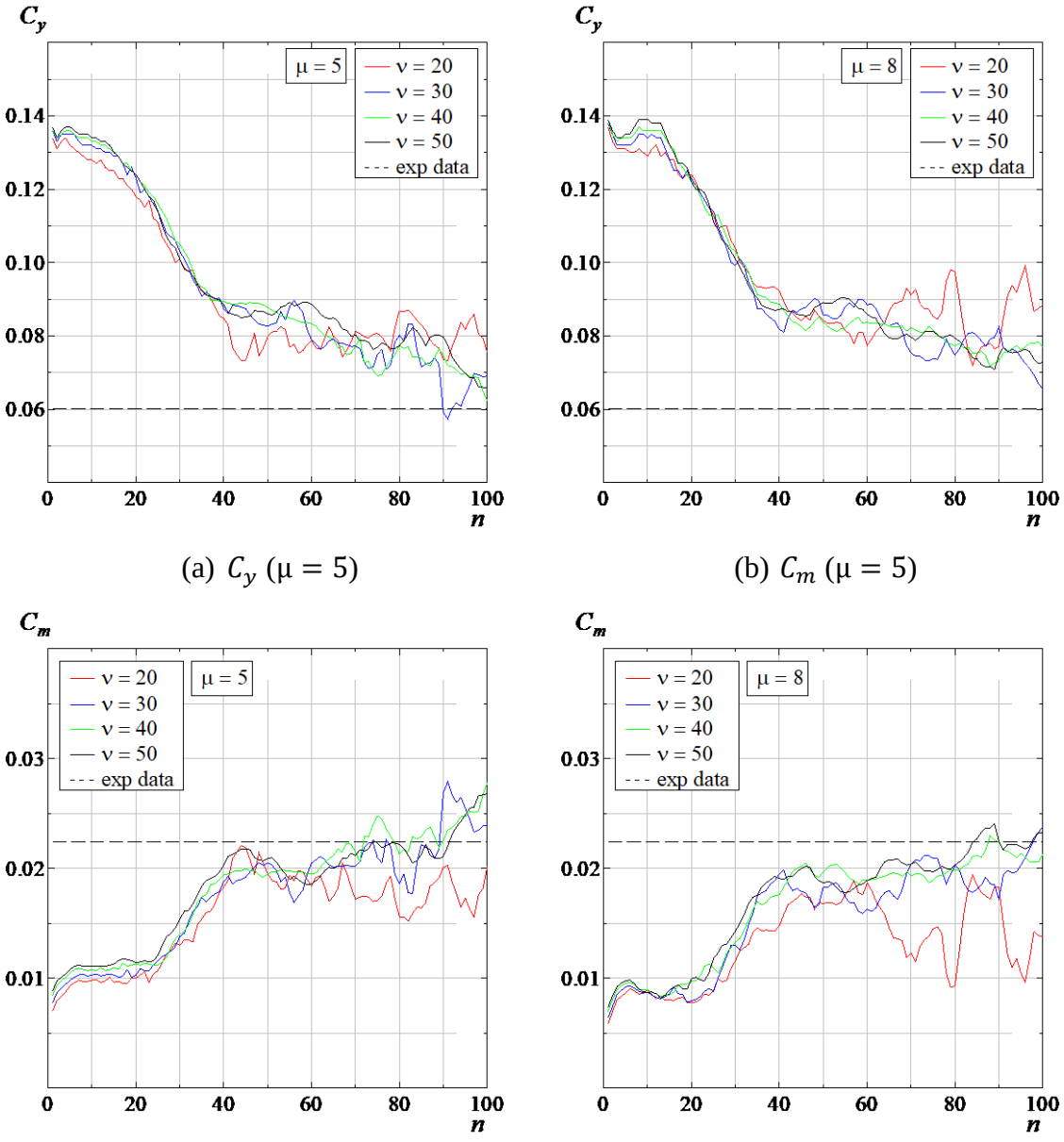

(a) C_y (μ = 5)

(b) C_m (μ = 5)

(c) C_y (μ = 8)

(d) C_m (μ = 8)

Figure 5.11 Comparison of lateral force coefficient C_y and yawing moment coefficient C_m (number of elements n_E = 50)

Higher number of divisions and free vortex elements are also executed in the convergence tests, but the results are not good because the higher number of divisions in vertical direction causes excessive interactions in the calculations of induced velocities by source and vortex. Furthermore, it makes calculation time too long.

The numbers of divisions for the arrangement of vortices are selected as $\nu = 30$ in longitudinal direction and $\mu = 5$ in vertical direction for both KCS and KVLCC2. Accordingly, the number of source panels arranged on the port and starboard sides of the hull becomes 600 ($= 30 \times 5 \times 2 \times 2$) including its mirror image. In addition, the ship breadth at the stern was set to be 1% wider than the exact breadth to avoid the divergence of induced velocity due to the computational singularity at the stern edge. Same with the Wigley hull conditions, all of the free vortices have the same number of elements which is set as 50 and the number of iteration is set as 100 times.

5.3.3 Lateral Force and Yawing Moment

Figs. 5.12 and 5.13 show the calculation results of lateral force coefficient C_y and yawing moment coefficient C_m of KCS and KVLCC2 for the two models as the function of drift angle β, respectively. In the figure, experimental data measured by captive model tests conducted at the Seakeeping and Manoeuvring Basin in Kyushu University are also shown for comparison. Experimental conditions are same as calculating conditions shown in the previous section.

Based on the figure, it is clear that the differences between calculation results of the model 1 and measured results for lateral force coefficient and yawing moment coefficient for both ships are too large comparing with the model 2. This likely happened because of too much simplification of vortex model at the bottom of the hull. On the other hand, calculation results of the model 2 show the same tendency with measured results in the small range of drift angle β for both ships. It means the models 2 can be considered having the same condition with the actual flow.

However, there still remains large difference between the calculated and measured results in the range of large drift angle β. As the value of drift angle becomes larger, interaction among free vortices, hull bottom and side hull becomes bigger. It is considered that the interaction has large influence on calculated hydrodynamic forces. Therefore, further

investigations of the treatment of free vortices existing around hull bottom and side hull are necessary as future works.

To check the applicability of the SQCM for the prediction of hydrodynamic forces acting on a ship hull in manoeuvring motion, the results are compared with the estimated hydrodynamic forces using the following approximate formulae for hydrodynamic derivatives (Kijima et al.1990).

$$\left.\begin{aligned} Y'_{\beta} &= \frac{1}{2}\pi k + 1.4C_b\, B/L\,, \\ Y'_{\beta\beta} &= 2.5d\,(1 - C_b)/B + 0.5, \\ N'_{\beta} &= k, \\ N'_{\beta\beta} &= -0.96d\,(1 - C_b)/B + 0.066, \end{aligned}\right\} \tag{5.2}$$

where,

k : $2d/L$.

As shown in Figs. 5.12 and 5.13, calculated results of the SQCM with the vortex model 2 show better accuracy comparing with the results obtained by using the approximate formulae for the small range of drift angle. However, lateral force coefficient and yawing moment coefficient estimated by using the approximate formulae have better accuracy for both ships in the large range of drift angle. According to these results, the applicability of the SQCM is quite good in the small range of drift angle, but it still has a lot of room to improve the accuracy in the prediction of lateral force and yawing moment. It is important to focusing on the free vortex model implemented when calculating the hydrodynamic forces using the SQCM.

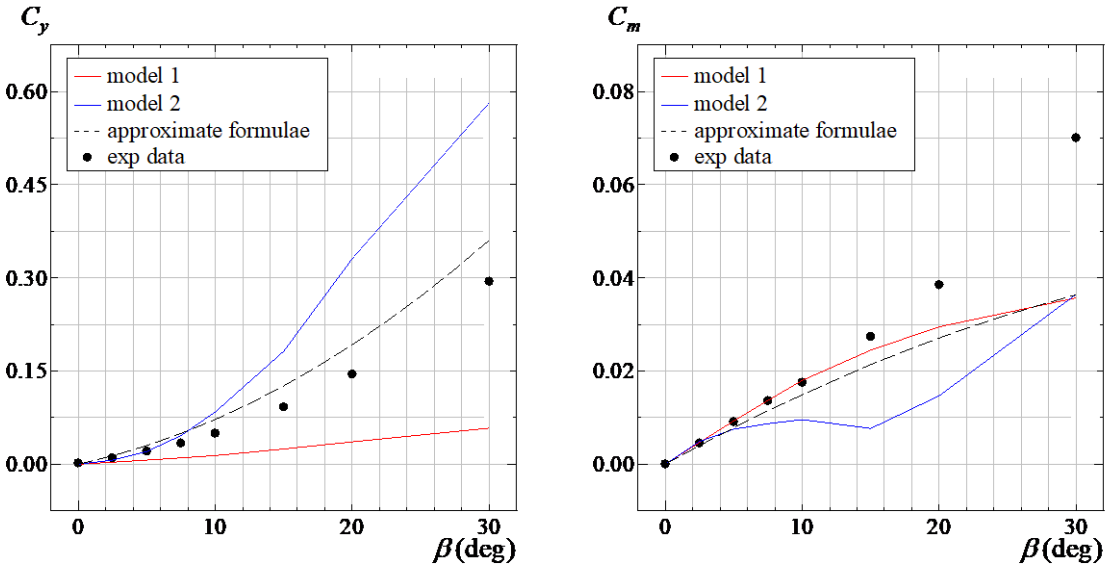

(a) Lateral force coefficient (b) Yawing moment coefficient

Figure 5.12 KCS lateral force coefficient C_y and yawing moment coefficient C_m

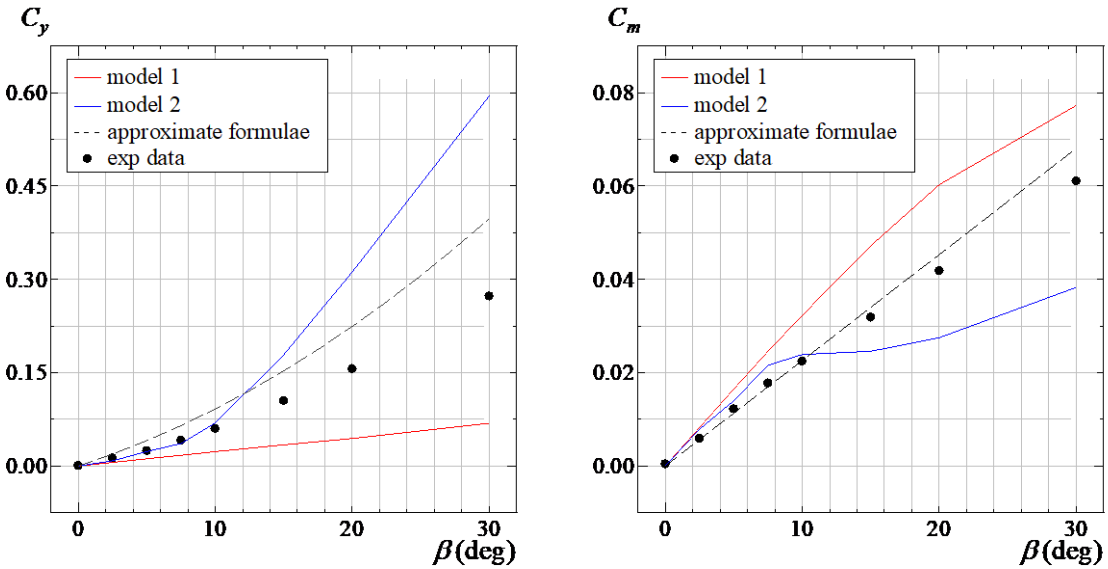

(a) Lateral force coefficient (b) Yawing moment coefficient

Figure 5.13 KVLCC2 lateral force coefficient C_y and yawing moment coefficient C_m

5.3.4 Pressure Distribution

Pressure distributions around the ship hull at drift angle $\beta = 20°$ are presented in Figs. 5.14 to 5.17 for both KCS and KVLCC2. Figs. 5.14 and 5.15 and Figs. 5.16 and 5.17 show pressure coefficients on the portside and starboard sides of KCS and KVLCC2 for all vortex models, respectively. There is no significant differences observed on the port side in any of the models except for the pressure distribution at the bottom of the hull and around the stern. Same tendency occurs with the results of the Wigley hull where the model 1 tends to have lower pressure distribution than that of the model 2. These phenomena can be observed for both ships. Large difference can be observed between the

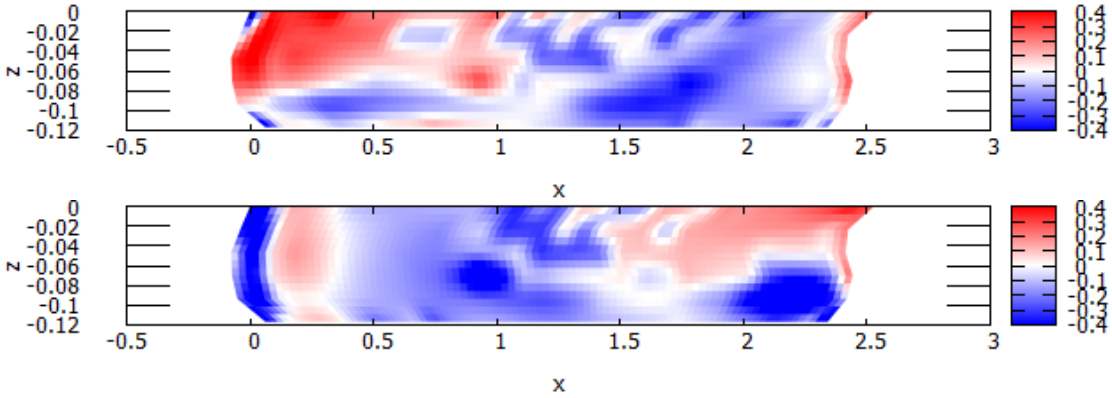

Figure 5.14 KCS pressure distribution on port side (up) and starboard side (down) for model 1 ($\beta = 20°$)

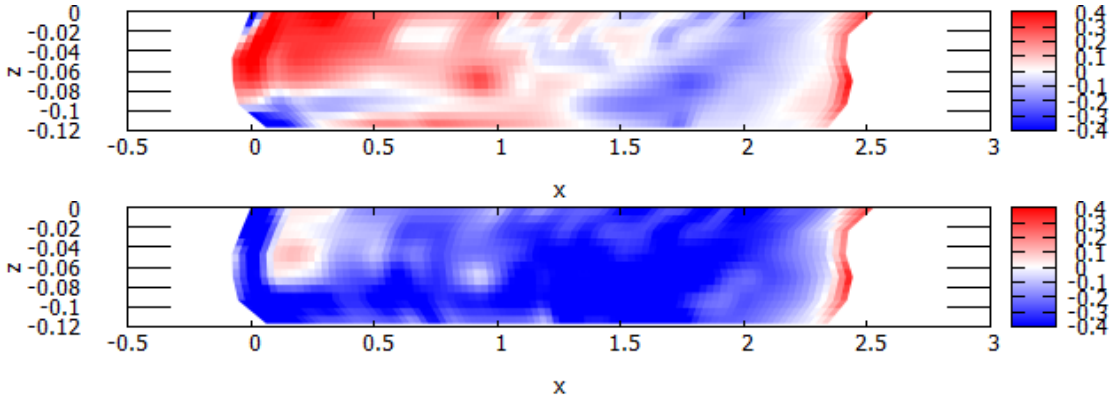

Figure 5.15 KCS pressure distribution on port side (up) and starboard side (down) for model 2 ($\beta = 20°$)

pressure coefficients on the starboard side for the vortex models 1 and 2. Similar results between pressure distribution on the starboard side and portside for the model 1 are recognized.

In contrast, the model 2 shows difference in pressure distributions between the port side and the starboard side clearly. The differences between the model 1 and the model 2 in starboard side are likely due to the existence of vortex strength around the hull. Therefore, in order to improve the prediction accuracy of hydrodynamic forces acting on the hull, it is necessary to investigate vortex model including the influence of shedding angle based on the model 2.

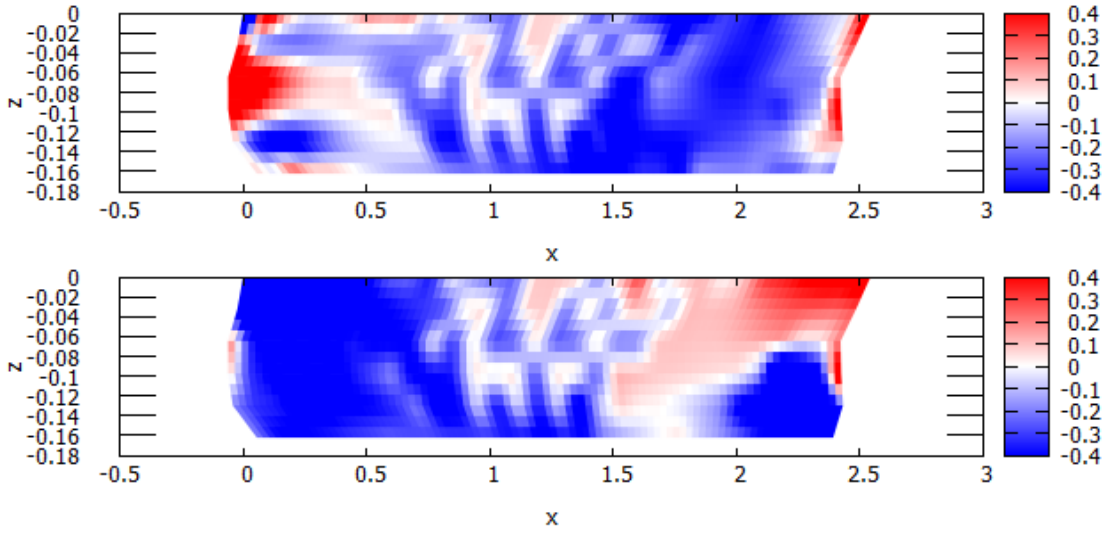

Figure 5.16 KVLCC2 pressure distribution on port side (up) and starboard side (down) for model 1 ($\beta = 20°$)

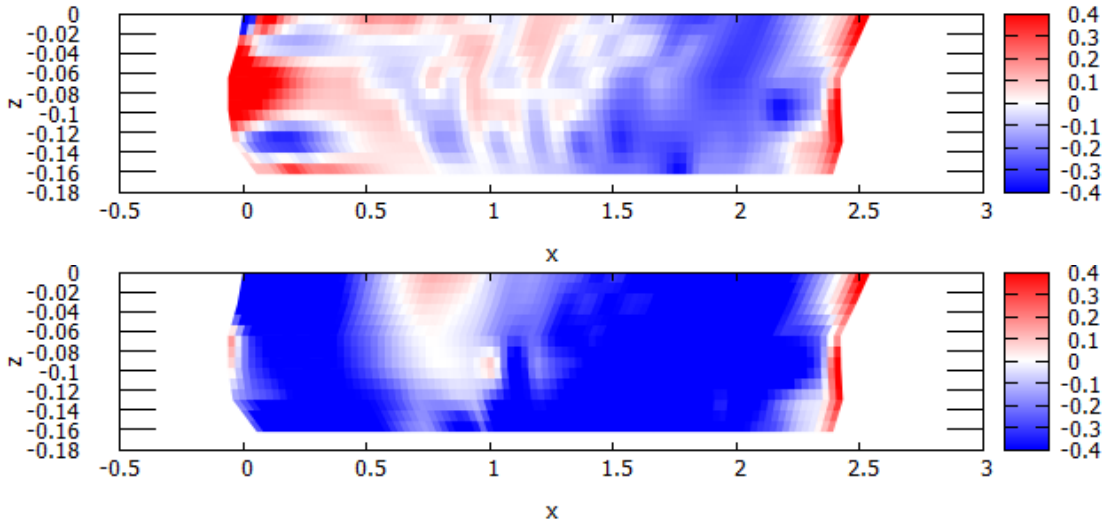

Figure 5.17 KVLCC2 pressure distribution on port side (up) and starboard side (down) for model 2 ($\beta = 20°$)

5.3.5 Velocity Field

Figs. 5.18 to 5.21 show velocity fields around KCS and KVLCC2 for the model 1 and the model 2, respectively. The velocity field conditions are same with the Wigley hull.

Figs. 5.18 and 5.20 show the results for the model 1 for KCS and KVLCC2, respectively. Same tendency with the Wigley hull is observed where there is no differences between flow fields at iteration number $n = 1$ and $n = 100$ due to vortex shed only from the stern. Small circulation can be observed due to the influence of induced velocity around the stern.

Velocity field for the model 2 for KCS and KVLCC2 are shown in Figs. 5.19 and 5.21, respectively. It is obvious that the differences between flow fields at iteration number $n = 1$ and $n = 100$ exist due to the vortex shed from hull bottom. Large magnitude of velocity vectors is observed on the bottom of the hull. This mainly caused by the fact that the flow from lateral direction become stronger as the drift angle becomes larger, affecting the yz plane component of the velocity in the basic coordinate system. Based on that, the flow field around the hull is not well reproduced in the large range of drift angle, and will affect to the calculation of hydrodynamic forces due to some errors.

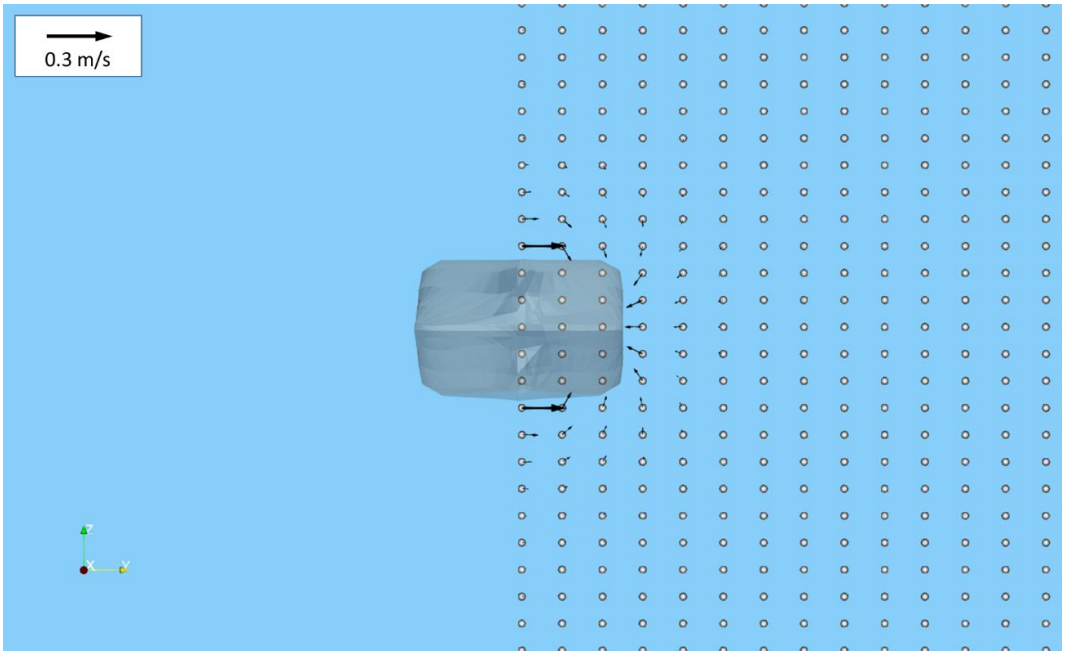

(a) $n = 1$

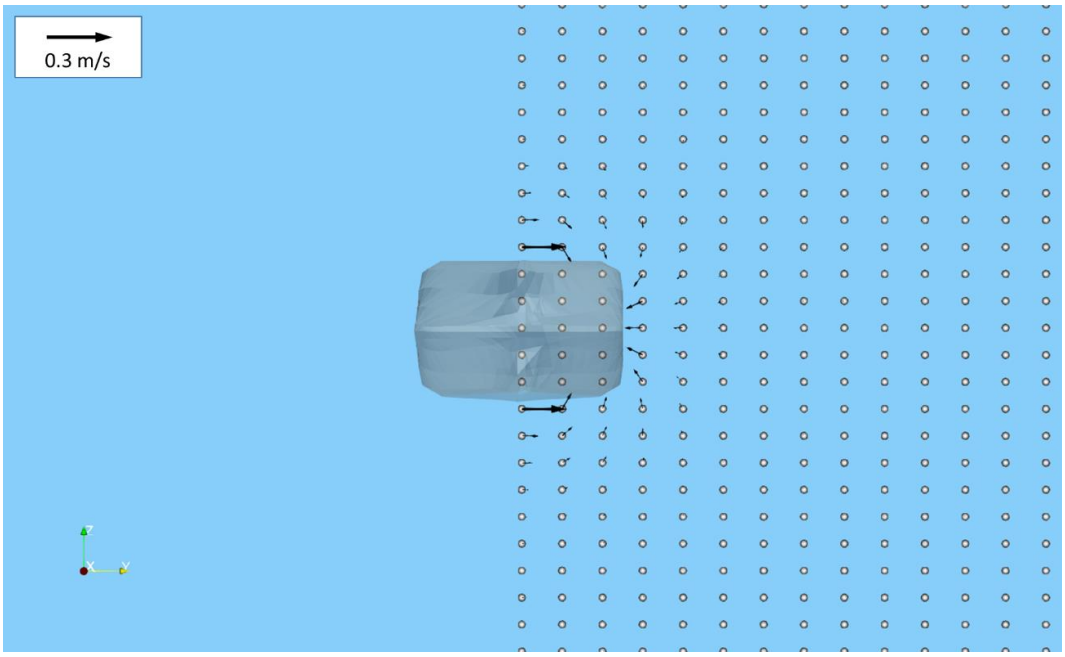

(b) $n = 100$

Figure 5.18 Flow velocity around the KCS hull for model 1 ($\beta = 30^{\circ}$)

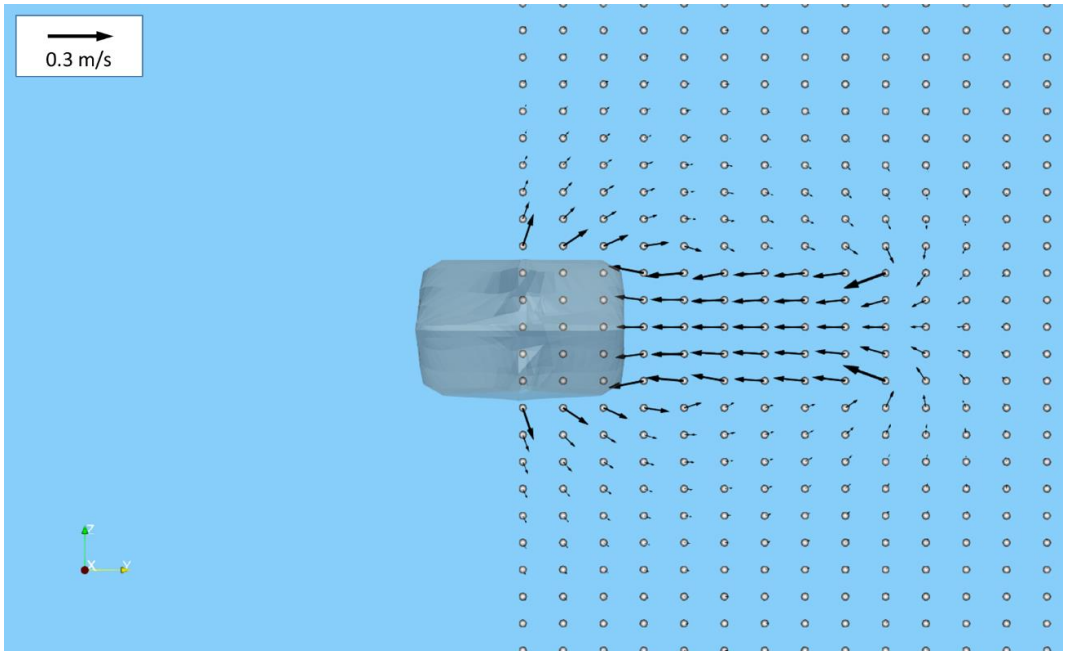

(a) $n = 1$

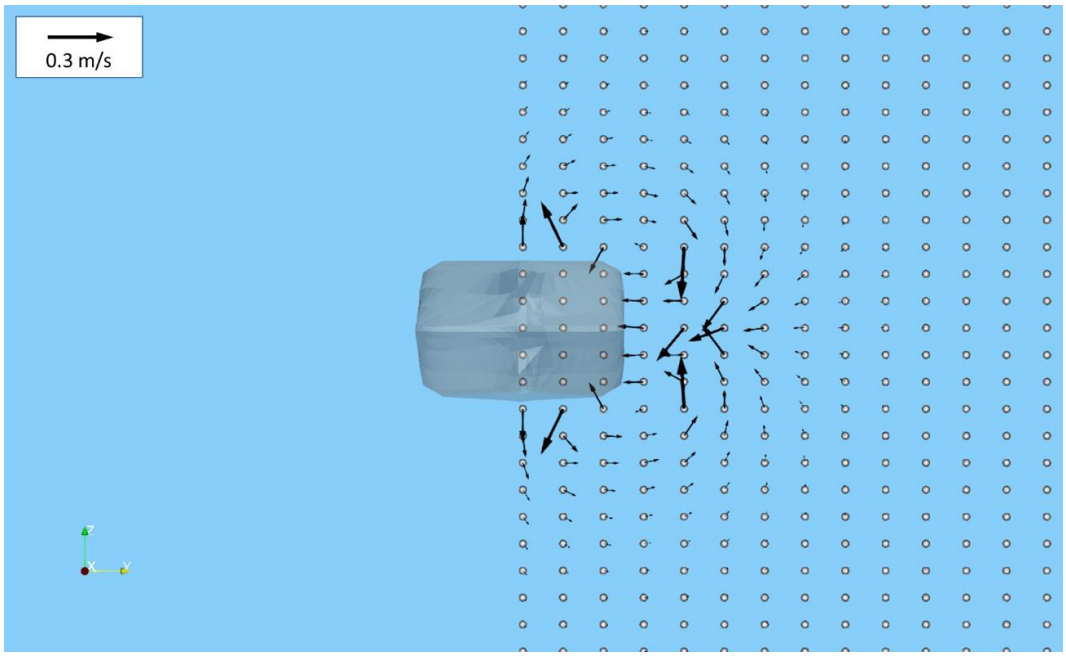

(b) $n = 100$

Figure 5.19 Flow velocity around the KCS hull for model 2 ($\beta = 30^{\circ}$)

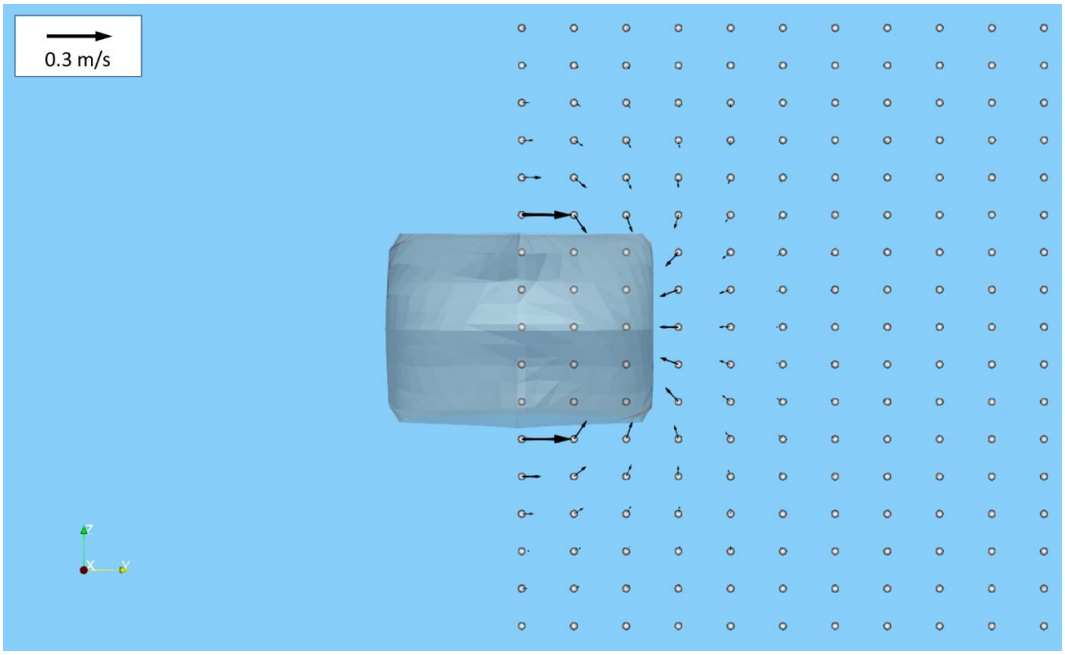

(a) $n = 1$

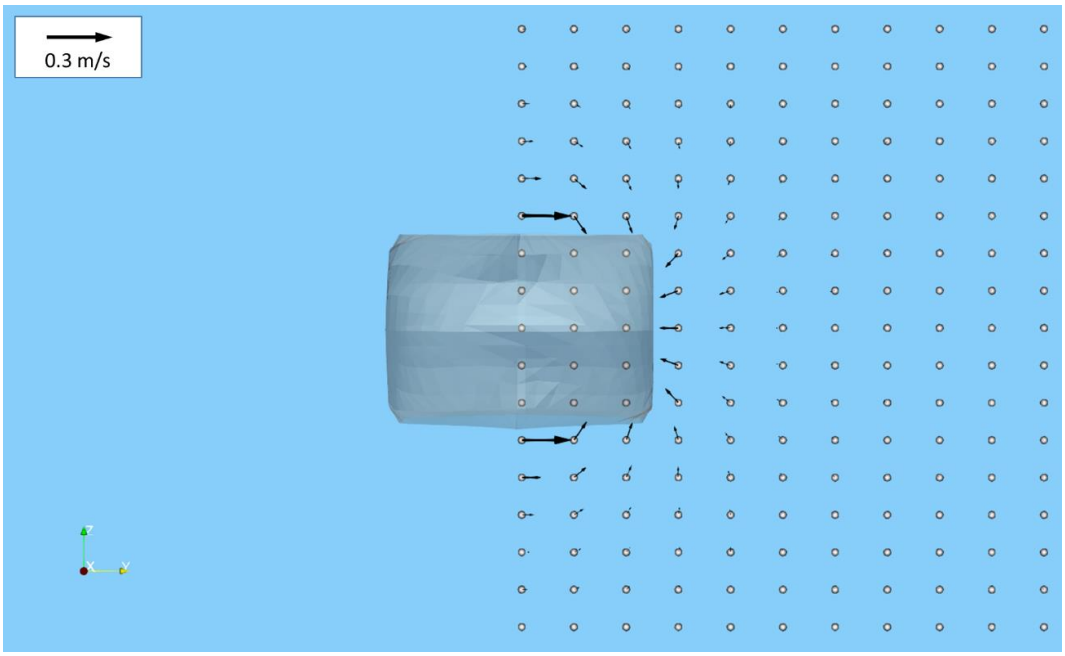

(b) $n = 100$

Figure 5.20 Flow velocity around the KVLCC2 hull for model 1 ($\beta = 30^{\circ}$)

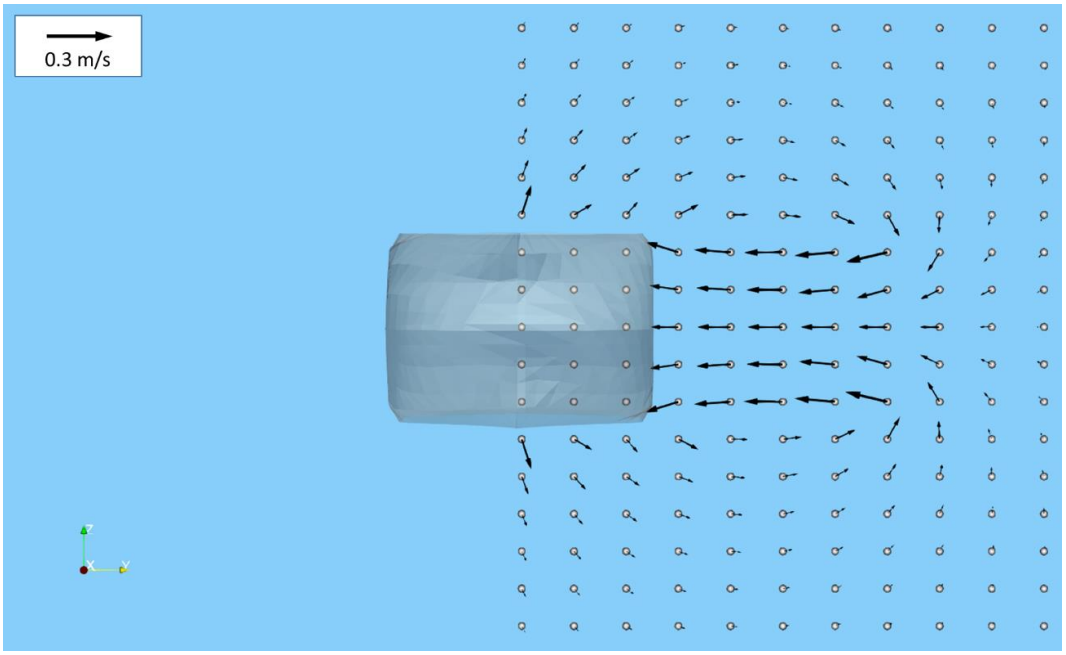

(a) $n = 1$

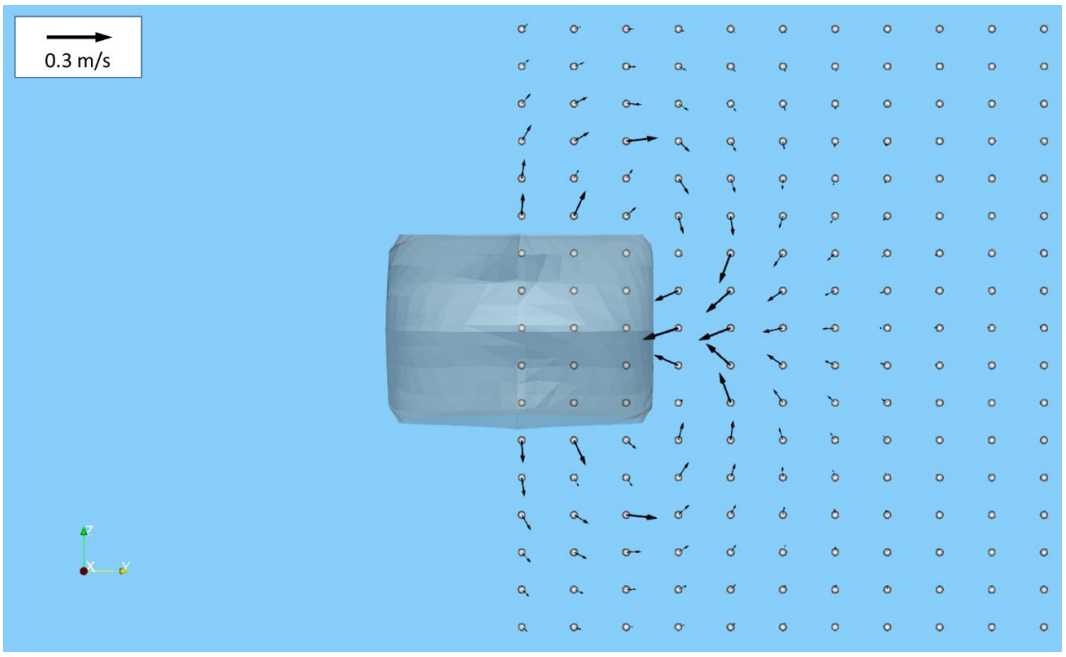

(b) $n = 100$

Figure 5.21 Flow velocity around the KVLCC2 hull for model 2 ($\beta = 30^{\circ}$)

5.4. Conclusion

Prediction of hydrodynamic forces acting on three different hulls in oblique motion using the SQCM has been investigated. Two kinds of vortex models considering the deformation of the shape of free vortices were applied and the calculated results were compared with measured data.

It was confirmed on lateral force coefficient C_y and yawing moment coefficient C_m that the free vortices shed from the bottom of the hull give improvement in results of prediction accuracy in the small range of drift angle β, but there still be significant difference in the large range of drift angle β. The difference in the large range of drift angle β generally generated by the flow from lateral direction.

Chapter 6 Conclusions

In this research, the difference between the characteristics of the cubic and the quadratic models for hydrodynamic forces acting on a ship hull is investigated by comparing course stability indices which are calculated by using linear hydrodynamic derivatives of both models. Then, to clarify the advantages and disadvantages of both models, sensitivity of simulated ship manoeuvring motion to hydrodynamic derivatives derived from measured lateral force and yawing moment including measurement error is investigated. Furthermore, applicability of the SQCM for the prediction of hull forces is investigated introducing two kinds of vortex models with the consideration of the deformation of free vortices.

Chapter 1 introduced a general overview of this study, such as ship manoeuvring standards, prediction methods for manoeuvring performance, mathematical models of hydrodynamic forces and so on. A summarized literature review was presented associated with the review of mathematical models of hydrodynamic forces, sensitivity analysis, and introduction to the SQCM. The objectives and expected outcome of this research as well as a brief layout of this thesis were also presented.

Two kinds of mathematical models for lateral force and yawing moment based on the cubic model and the quadratic model were presented in Chapter 2. Course stability index was investigated to see the differences between the cubic and the quadratic models. It was confirmed the different sign between the cubic model and the quadratic model caused by the difference on linear hydrodynamic derivatives. Existence of measured hydrodynamic forces in the large range of drift angle tends to give different result between the cubic and the quadratic models.

In Chapter 3, sensitivity of simulated manoeuvring motion to hydrodynamic derivatives derived from measured lateral force and yawing moment including measurement error was investigated. Pseudo measurement data were created to evaluate the influence of measurement error on the hydrodynamic derivatives. The cubic model was confirmed to less susceptible to measurement error comparing with the quadratic model. On the other hand, manoeuvring indices predicted by using hydrodynamic derivatives based on the quadratic model tends to have larger standard deviation comparing with the cubic model.

Measurement error included in measured hydrodynamic forces have much influence on transient motion of a ship such as 10°/10° zigzag manoeuvre.

A method to predict lateral force and yawing moment on a ship hull representing the shape of the hull accurately has been proposed in Chapter 4. In this method, ship is treated as thick wing. Hydrodynamic forces acting on a ship hull can be obtained by calculating induced velocities by sources and horseshoe vortices. To represent the flow field around the hull appropriately, two kinds of vortex models considering the deformation of free vortices are introduced. Free vortices of the horseshoe vortices were divided into vortex elements and the motion of each vortex element were calculated based on induced velocities by source panels and other vortices.

The results of predicted lateral force and yawing moment acting on a ship hull by the SQCM were presented in Chapter 5. Two kinds of vortex models with considering the deformation of the shape of free vortices were applied and the calculated results were compared with the measured data. It was confirmed on lateral force coefficient C_y and yawing moment coefficient C_m that the free vortices shed from the bottom of the hull give improvement in results of prediction accuracy in the small range of drift angle β, but there still be significant difference in the large range of drift angle β. The difference in the large range of drift angle β generally generated by the flow from lateral direction.

From the above results, it can be said that the cubic model has a better approximation accuracy when the hydrodynamic forces are measured in the large range of drift angle. It was shown that the quadratic model may give better approximation results when the measurement range is small. The first and second terms of course stability index also investigated. Almost all the absolute values of the first and second terms of course stability index for the quadratic model is smaller than those of the cubic model. Though influence of hydrodynamic derivatives for lateral force and yawing moment on simulated manoeuvring motion was only investigated in this research, there are many parameters which have significant impact on ship manoeuvrability. They should be further investigated considering realistic measurement error. As for SQCM, this method give a capable result of prediction accuracy in the small range of drift angle β. However, in

order to improve the prediction accuracy of hydrodynamic forces acting on a ship hull, it is necessary to investigate new model and the outflow shedding angle of free vortex.

Acknowledgment

First of all, I am very grateful to my supervisor, Professor Yoshitaka Furukawa, for his invaluable guidance, supports, and advice during my studies at Kyushu University. Not only supervised my study, but also provided great supports and guidance for my daily life in Japan, especially in this pandemic time. Without his help, pretty sure I will not be able to complete my research and study.

I am grateful to Professor Jun Ando from Department of Marine Systems Engineering, Faculty of Engineering, Kyushu University, and Professor Changhong Hu from Division of Renewable Energy Dynamics, Research Institute for Applied Mechanics (RIAM), Kyushu University for their valuable advices and suggestions to my thesis. Also I am greatly indebted to Mr. Hiroshi Ibaragi for helping me a lot in my first year of my study, helpful advice and constructive comments related to my research.

I would like to express my gratitude to the former members of Marine Dynamics and Control Laboratory especially Dr. Yuda Apri Hermawan, Dr. Bora Choe, Mr. Kenshi Yamashita, Mr. Kento Yamauchi, Mr. Ryuto Miyajima, Ms. Chinami Morikawa, and Ms. Yukari Hosoi for their advices and help not only for my research but also for my daily life.

Many thanks to all members of Marine Dynamics and Control Laboratory during my study, Doctoral student, (Hee Jin Lee), Master students 2nd year, (Atsushi Koda, Yasutaka Gosho, Yukio Shimada), Master students 1st year, (Katsunao Takahashi, Kentaro Koroki, Ryo Katahira, Takuro Arai, Takuya Mizuno) and Undergraduate students, (Hechun Xu, Takuki Hayashi, Yuya Matsunaga) for their supports during my study.

Special thanks to my best friend Mr. Yoshi Takeda who always helping me whenever I had a hard time during living in Japan and for my Indonesian friends that I can't mention one by one, thank you very much for your support.

Finally, I would like to express my sincere gratitude for my parents, my sister and brother, for their support and encouragement. This thesis is dedicated to my family.

References

Abkowitz, M.A., 1964, “Lectures on Ship Hydrodynamics – Steering and Manoeuvrability”, Hydro-og Aerodynamisk Laboratorium, Lyngby, Denmark, Report No. Hy-5.

Ando, J., Nakatake, K. and Maita, S., 1995, “A Simple Surface Panel Method to Predict Steady Marine Propeller Performance”, Journal of the Society of Naval Architects of Japan, 178, 61-69.

Ando, J., Yamamoto, T., Maita, S. and Nakatake, K., 1997, “An Estimation of Hydrodynamic Forces Acting on a Ship in Oblique Towing by a Simple Surface Panel Method (SQCM)”, Transactions of The West-Japan Society of Naval Architects, 94, 13-20.

Ayub, F.A., Furukawa, Y. and Ibaragi, H., 2019, “Sensitivity Study of Manoeuvring Motion of Ships using Whole Ship Model,” Proceeding of Maritime Safety International Conference (MASTIC 2018), Bali, 118-126.

Ayub, F.A. and Furukawa, Y., 2020, “Prediction of Hydrodynamic Forces Acting on Wigley Hull based on SQCM,” 2nd Maritime Safety International Conference (MASTIC), Surabaya, IOP, 557, 012015.

Ayub, F.A., Furukawa, Y. and Ibaragi, H., 2021, “Sensitivity Analysis of Hydrodynamic Derivatives for Lateral Force and Yawing Moment”, 31st International Ocean and Polar Engineering Conference (ISOPE), Rhodes, Greece.

Ayub, F.A., Furukawa, Y. and Ibaragi, H., 2021, “Prediction of Hydrodynamic Forces Acting on Ship Hull based on SQCM”, 31st International Ocean and Polar Engineering Conference (ISOPE), Rhodes, Greece.

Cebeci T., Platzer M., Chen H., Chang K.C. and Shao J.P., 2005, “Panel Methods”, Analysis of Low-Speed Unsteady Airfoil Flows. Springer, Berlin, Heidelberg.

Chudley, J., Dove, M.J. and Tapp, N.J., 1991, “A Review of Mathematical Models Used in Ship Maneouvres”, Proceedings of CADMO ‘91, Florida, USA.

Clarke, D., 1972, “A Two-Dimensional Strip Method for Surface Ship Hull Derivatives: Comparison of Theory with Experiments On a Segmented Tanker Model”, J.Mech.Eng Sci. (14) No. 7, Supplementary Issue

Crane, C.L., 1979, “Manoeuvring Trials of 278000 DWT Tanker in Shallow and Deep Water”, Transactions SNAME, New York, 87.

Cura Hochbaum, A., Vogt, M. and Gatchell, S., 2008, “Manoeuvring Predictions for Two Tankers based on RANS Simulations”, Proceedings of SIMMAN 2008, Copenhagen 14-16.

Davidson, K.S.M. and Schiff, L.I., 1946, “Turning and Course Keeping Qualities”, The Society of Naval Architects and Marine Engineers, N. Y., 54, pp. 152-200.

Dash, A.K., Nagarajan, V. and Sha, O.P., 2015, “Uncertainty Assessment for Ship Maneuvering Mathematical Model”, International Ship Building Progress, Vol. 61, pp. 129-161.

Dand, I.W., 1987, “On Modular Manoeuvring Models”, Proc. RINA International Conference on Ship Manoeuvrability – Prediction Achievement, RINA, London, U.K., Paper No. 8.

Dand, I.W., 1992, “Measurement Errors and Manoeuvring Prediction”, Workshop on Prediction of Ship Manoeuvrability, Fukuoka, The West-Japan Society of Naval Architects.

Fedyaevsky, K.K. and Sobolev, G.V., 1963, “The Handling Qualities of Ships”, Sudpromgiz, Leningrad.

Fedyaevsky, K.K. and Sobolev, G.V., 1963, “Control and Stability in Ship Design”. State Union Ship Building Publishing House, Leningrad.

Gavrilin, S. and Steen, S., 2015, “Uncertainty of Sea Trials Results Used for Validation of Ship Manoeuvring Simulation Models”, OMAE 2015, St. John’s, Newfoundland, Canada, 7 pp.

Gavrilin, S. and Steen, S., 2016, “An Alternative Approach to Validation of Ship Manoevring Models”, OMAE 2016, Busan, Korea, 8 pp.

Hess, J.L. and Smith, A.M.O., 1964, “Calculation of Nonlifting Potential about Arbitrary Three Dimensional Bodies,” Journal of Ship Research, 8(2), 22-44.

Helton, J., Johnson, J., Salaberry, C. and Storlie, C., 2006, “Survey of Sampling-Based Methods for Uncertainty and Sensitivity Analysis”, Reliab. Eng. Syst. Saf. 91, 1175–1209.

Inoue, S., 1978, “The Hydrodynamic Derivatives on Ship Manoeuvrability in Even Keel Conditions”. Proceeding of 15th International Towing Tank Conference (ITTC),

International Maritime Organization, 1993, “Interim Standards for Ship Manoeuvrability”, Resolution A.751(18) (adopted on 4 November 1993).

International Maritime Organization, 2002. “Standards for Ship Manoeuvrability”, Annex 6 Resolution MSC.137(76) (adopted on 4 December 2002).

Iooss B. and Saltelli A., 2017, “Introduction to Sensitivity Analysis”. Ghanem R., Higdon D., Owhadi H. (eds) Handbook of Uncertainty Quantification. Springer, Cham.

ITTC Manoeuvring Committee, 1999, “Report of the Manoeuvring Committee,” Proceeding of 22nd International Towing Tank Conference (ITTC), Seoul-Shanghai.

ITTC Manoeuvring Committee, 2008, “Report of the Manoeuvring Committee,” Proceeding of 25th International Towing Tank Conference (ITTC), Fukuoka, I, 143-208.

ITTC Manoeuvring Committee, 2017, “Report of the Manoeuvring Committee,” Proceeding of 28th International Towing Tank Conference (ITTC), Wuxi, I, 131-213.

ITTC Manoeuvring Committee, 2017, “Recommended Procedure and Guidelines: Uncertainty Analysis for Manoeuvring Predictions based on Captive Manoeuvring Tests”, 7.5-02-06-04, p.33, Effective date 2017, Rev. 2.

Kanemaru, T. and Ando, J., 2013, “Numerical Analysis of Cavitating Propeller and Pressure Fluctuation On Ship Stern Using a Simple Surface Panel Method “SQCM””, Journal of Marine Science and Technology, 18, 294-309.

Kijima, K., Katsuno, T., Nakiri, Y. and Furukawa, Y., 1990, “On the Manoeuvring Performance of a Ship with the Parameter of Loading Condition”, Journal of The Society of Naval Architects of Japan, 168, 141-148.

Kleijnen, J., 1997, “Sensitivity Analysis and Related Analyses: A Review of Some Statistical Techniques”, J. Stat. Comput. Simul. 57, 111–142.

Kose, K. and Saeki, T., 1979, “On a New Mathematical Model of Manoeuvring Motion of a Ship”, Journal of Society of Naval Architects of Japan, Vol. 146. (written in Japanese).

Lan, C.E., 1974, “A Quasi-Vortex-Lattice Method in Thin Wing Theory,” Journal of Aircraft, 11(9), 518-527.

Maita, S., Ando, J. and Nakatake, K., 1997, “A Method to Solve Unsteady Two-dimensional Wing Problems by a Simple Surface Panel Method (SQCM)”, Transactions of The West-Japan Society of Naval Architects, 93, 15-24.

Maita, S., Ando, J. and Nakatake, K., 1997, “A Method to Solve Unsteady Three-dimensional Wing Problems by a Simple Surface Panel Method (SQCM)”, Transactions of The West-Japan Society of Naval Architects, 94, 1-11.

Maita, S., Ando, J. and Nakatake, K., 1997, “A Simple Surface Panel Method to Predict Unsteady Marine Propeller Performance”, Journal of the Society of Naval Architects of Japan, 182, 71-80.

McCallum, I.R., 1992, “Assessment and Improvement of Ship Handling Characteristics”, Proceedings of 5th International Symposium on Practice Design of Ships and Mobile Units, PRADS ’92, Newcastle upon Tyne, U. K., pp. 1. 284- 1. 297.

Nakatake, K., Ando, J., Kataoka, K. and Yoshitake, A., 1994, “A Simple Calculation Method for Thick Wing,” Transaction of the West-Japan Society of Naval Architects, 88, 13-21. (Written in Japanese).

Nomoto, K., Taguchi, T., Honda, K. and Hirano, S., 1957, “On the Steering Qualities of Ships”, International Ship Building Progress, 4-35, 354-370.

Norrbin, N.H., 1971, “Theory and Observations on the Use of a Mathematical Model for Ship Maneuvering in Deep and Confined Waters”, Proc. 8th ONR Symposium on Naval Hydrodynamics, Pasadena, USA, pp. 807-904.

Ogawa, A., Hasegawa, K. and Yoshimura, Y., 1980, “MMG Report V”, Bulletin, Soc. N.A. Japan, No.616.

Ogawa, A., Kasai, H., 1978, “On the Mathematical Model of Manoeuvring Motion of Ships”, International Shipbuilding Progress, Volume 25, No. 292, p. 306-319.

Saltelli, A., Tarantola, S. and Campolongo, F., 2000, “Sensitivity Analysis as an Ingredient of Modelling”, Stat. Sci. 15, 377–395.

Saltelli, A., 2002, “Making Best Use of Model Evaluations to Compute Sensitivity Indices”, Computer and Physics Community. 145, 280–297.

Shenoi, R., Krishnankutty, P. and Selvam, P., 2015, “Sensitivity Study of Hydrodynamic Derivative Variations on the Maneuverability Prediction of a Container Ship”, OMAE 2015, St. John’s, Newfoundland, Canada, 9 pp.

Shin, S.S., Ahn, K.S., Sung, Y.J. and Oh, S.H., 2012, “A Study on Effect of the Self-Propulsion Points in PMM Tests for KVLCC’s Manoeuvrability,” Proceeding of International Conference Ship Manoeuvrability and Maritime Simulation (MARSIM 2012), Singapore, 449-457.

Son, K. and Nomoto, K., 1981, “On the Coupled Motion of Steering and Rolling of a High Speed Container Ship,” Japan Society of Naval Architects, Japan, 150, 232-244.

Sung, Y.J., Park, S.H., Ahn, K.S., Chung, S.H., Shin, S.S. and Jun, J.H., 2014, “Evaluation on Deep Water Manoeuvring Performances of KVLCC2 based on PMM Test and RANS Simulation,” Proceeding Workshop on Verification and Validation of Ship Manoeuvring Simulation Methods (SIMMAN 2014), Copenhagen, Denmark, C105-C110.

Toxopeus, S.L. and Lee, S.W., 2008, “Comparison of Manoeuvring Simulation Programs for SIMMAN Test Cases”, SIMMAN 2008, Copenhagen

Turanyi, T., 1990, “Sensitivity Analysis for Complex Kinetic System, Tools and Applications”, J. Math. Chem. 5, 203–248.

Wang, X.G., Zou, Z.J., Xu, F. and Ren, R.Y., 2014, "Sensitivity Analysis and Parametric Identification for Ship Manoeuvring in 4 Degrees of Freedom", Journal of Marine Science and Technology, Vol. 19, pp. 394–405.

Woodward, M., 2013, “Propagation of Experimental Uncertainty from Force Measurements into Manoeuvring Derivatives”, AMT ’13: 3rd International Conference on Advanced Model Measurement Technology, Gdansk, Poland

Woodward, M. D., 2014, “Evaluation of Inter-Facility Uncertainty for Ship Manoeuvring Performance Prediction”, Ocean Engineering, Vol. 88, pp. 598-606.

Yasukawa, H. and Yoshimura, Y., 2015, “Introduction of MMG Standard Method for Ship Maneuvering Predictions,” Japan Marine Science and Technology, 20, 37-52.

Zhou X. and Lin H., 2008, “Local Sensitivity Analysis”, Shekhar S., Xiong H. (eds) Encyclopedia of GIS. Springer, Boston, MA.s